Title
Energetics of Domain Engineered Rhombohedral Ferroelectric Single Crystals

Author
Lv, Peng

Publication Date
2018

Peer reviewed|Thesis/dissertation

UNIVERSITY OF CALIFORNIA

Los Angeles

Energetics of Domain Engineered Rhombohedral Ferroelectric Single Crystals

A dissertation submitted in partial satisfaction of the

requirements for the degree Doctor of Philosophy

in Mechanical Engineering

by

Peng Lv

2018

ABSTRACT OF THE DISSERTATION

Energetics of Domain Engineered Rhombohedral

Ferroelectric Single Crystals

by

Peng Lv

Doctor of Philosophy in Mechanical Engineering

University of California, Los Angeles, 2018

Professor Christopher S. Lynch, Chair

Domain engineered ferroelectric relaxor-PT crystals have attracted extensive attentions due to their ultrahigh piezoelectric coefficients and electromechanical coupling factors. To gain insight into the microstructure and its effects on the material behavior, a modeling approach was developed from an energetic perspective. A Landau-Devonshire energy function, in the form of a 10^{th} order polynomial, was proposed to describe the dielectric, piezoelectric and ferroelectric properties of rhombohedral phase PIN-PMN-PT crystals with a MPB composition. The coefficients of this energy function were determined through extensive fitting to the experimental data. The resulting energy function reproduced the temperature induced phase transformations as well as the polarization and strain hysteresis loops of domain engineered 4R and 2R crystals. This energy function was then implemented in a phase-field model to investigate the evolution of

domain structures under the electric field. A new way to apply periodic boundary conditions was implemented to accommodate nonzero strain during domain formation and evolution. The domain formation process was simulated first and 71 and 109 domain walls were found to populate the crystals. Then these two types of domain walls were individually studied under the electric field applied along the [110] direction. They showed different behavior in response to the electric field. A domain wall broadening effect was observed on 71 domain walls when below the coercive field. When the field exceeded the coercive field, homogeneous polarization switching occurred with no motion of 71 domain walls. While the sweeping of 109 domain walls facilitated heterogeneous polarization switching and reduced the energy required relative to homogeneous polarization switching. The two mechanisms of domain evolution are consistent with the minimal domain wall motion in the engineered domain structures under the electric field. With this work, the application of the phase-field method was expanded to the new rhombohedral phase relaxor-PT crystals beyond ferroelectric materials with tetragonal symmetry. This work also deepened the understanding of domain structures of ferroelectric single crystals that is important in many applications.

The dissertation of Peng Lv is approved.

Gregory P. Carman

Vijay Gupta

Ertugrul Taciroglu

Christopher S. Lynch, Committee Chair

University of California, Los Angeles

2018

For my parents,

Hongjun Lv and Lijuan Tang,

and my wife,

Xiaoli Kong

TABLE OF CONTENTS

1 Introduction 1

1.1 Motivation 1

1.2 Background 7

1.2.1 Piezoelectricity 7

1.2.2 Ferroelectricity 13

2 Thermodynamics of ferroelectric materials 21

2.1 External work, heat addition and internal energy 21

2.2 Energy function formulation based on series expansion 26

2.3 Evolution law for polarization 33

2.4 Finite element implementation 35

3 Energy function development for ferroelectric single crystals 38

3.1 Introduction 38

3.2 Landau-Devonshire energy function 42

3.2.1 Energy function formulation 42

3.2.2 Material properties 44

3.2.3 Coefficient determination 46

3.3 Simulated thermal properties 49

3.4 Electric field driven homogeneous polarization switching 54

3.5 Combined effect of temperature and electric field 61

3.6 Conclusion 63

Appendix A Coefficient determination 64

4 Phase-field simulation of domain walls in ferroelectric single crystals 68

4.1 Introduction 68

4.2 Phase-field method 70

4.3 Domain wall formation 77

4.4 Electric field driven domain wall evolution 81

4.4.1 71 domain wall 81

4.4.2 109 domain wall 83

4.5 Conclusion 87

5 Summary and conclusions 88

References 90

LIST OF FIGURES

Figure 1.1. Piezoelectric coefficient d_{33} and electromechanical coupling factor k_{33} of relaxor-PT single crystals and piezoelectric ceramics as a function of the Curie temperature [1]. 1

Figure 1.2. Domain engineered rhombohedral crystals. (a) Eight variants of rhombohedral crystals before poling. (b) 4R crystals obtained by poling along the [001] direction. (c) 2R crystals obtained by poling along the [011] direction. 2

Figure 1.3. (a) Phase diagram of PMN-PT in terms of temperature and composition [7]. The MPB is in the range of 31%-37% PT. (b) Phase diagram of PIN-PMN-PT in terms of composition [8]. The MPB is in the range of 24%-33% PIN and 30%-33% PT. 4

Figure 1.4. A conceptual schematic showing the perovskite structure of lead titanate in the high temperature cubic phase (left) and the low temperature tetragonal phase with spontaneous polarization *P*s (right). 9

Figure 1.5. Energy landscape of a tetragonal structure plotted as a function of two polarization components P_1 and P_2. (a) Energy landscape with four energy wells representing four spontaneous states of a tetragonal structure in 2 dimensional space. (b) Energy landscape under an electric field applied along the P_2 axis. (c) Energy landscape under mechanical compression applied along the P_2 axis. 15

Figure 1.6. The schematics of ferroelectric crystalline materials before and after poling. (a) Single crystals with multiple domains. Dashed lines represent domain walls. (b) A single domain is formed under electric field *E*. (c) Polycrystalline ceramics with multiple grains. Solid lines represent grain boundaries. (d) Domains are reoriented under electric field *E*. Not all domains align with the electric field due to the constraints imposed by neighboring domains and grains. 17

Figure 1.7. The electric displacement and strain hysteresis loops of 8/65/35 PLZT [34]. (a) The hysteresis loop of electric displacement vs electric field. The slope at zero electric field is the linear dielectric permittivity. (b) The hysteresis loop of longitudinal strain vs electric field. The slope at zero electric field is the linear piezoelectric coefficient. 19

Figure 2.1. The superposition of a quadratic polynomial and a quartic polynomial to generate local minima..... 30

Figure 3.1. A schematic of the composition-temperature phase diagram of PIN-PMN-PT. C, T, O and R denote cubic, tetragonal, orthorhombic and rhombohedral phase, respectively. Vertical red dashed line represents the MPB composition for which the energy function is developed. The horizontal orange dashed line represents the compositions that have been experimentally characterized. A typical MPB composition contains 32%-33% of PT. 46

Figure 3.2. A schematic of a pseudo-cubic unit cell (a) and its energy density plotted as a function of P_{12} and P_3 above the Curie temperature (b) and at room temperature (c). 50

Figure 3.3. Energy density of three ferroelectric phases plotted as a function of temperature. The phase transition temperatures are obtained at the intersections of the curves. 51

Figure 3.4. (a) Spontaneous polarization P_S plotted as a function of temperature. (b) Dielectric constants e_{ii} (i = 1, 2, 3) plotted as a function of temperature. Superscript T, O and R represent tetragonal, orthorhombic and rhombohedral phase, respectively. The subscript of the dielectric constants follows the definitions in Table 3.1. 53

Figure 3.5. The simulated volume average polarization-electric field (*PE*) hysteresis loops for 4R (a) and 2R (b). The energy landscape labeled as A, B, C and D are corresponding to the points in the *PE* hysteresis loops. 57

Figure 3.6. The simulated volume average strain-electric field (*SE*) hysteresis loops for 4R (a) and 2R (b). 58

Figure 3.7. The hysteresis loops at 25°C, 50°C and 75°C. (a) The *PE* loops of 4R. (b) The *PE* loops of 2R. (c) The *SE* loops of 4R. (d) The *SE* loops of 2R. 62

Figure 4.1. (a) The "cubic" coordinate system used in reference [10]. The three axes are in the directions [100]-[010]-[001]. (b) The 2D "rhombohedral" coordinate system used in this work. The three axes are in the directions [-110]-[001]-[110]. The *y*-*z* plane is the diagonal plane (-110) in (a). It contains four rhombohedral variants, R1, R2, R3 and R4. 71

Figure 4.2. A schematic of a representative volume element with boundaries (Top, Bot, Left and Right) and vertex points (LT, RT, LB and RB). *u* and *v* are horizontal and vertical displacement components, respectively. 78

Figure 4.3. Domain formation process in a representative volume element of the rhombohedral ferroelectric single crystals. The colors represent the magnitude of polarization with unit C/m^2. The white arrows represent the directions of polarization. The deformation is magnified by 10 times. 80

Figure 4.4. The broadening of the 71 domain walls when the electric field is below the coercive field. T is the period of the electric field. The domain wall is zoomed in to show the variation of the domain wall thickness. 82

Figure 4.5. The homogeneous polarization switching with no motion of the 71 domain walls when the electric field exceeds the coercive field. The domains before and after the switching are shown on the right. 83

Figure 4.6. The sweeping of the 109 domain walls and heterogeneous polarization switching under the constant electric field 0.1MV/m. A single domain is formed after the two domain walls merge and disappear. 84

LIST OF TABLES

Table 1.1. Symbols in piezoelectric constitutive equations. 11

Table 2.1. Thermodynamic potentials with different independent variables. 25

Table 3.1. Nomenclature used to describe ferroelectric relaxor single crystals. 1T, 1O and 1R represent tetragonal, orthorhombic and rhombohedral crystals in the single domain state. 2R and 4R are domain engineered rhombohedral crystals with two and four variants..... 41

Table 3.2. Data used to determine the coefficients of the energy function for a MPB composition of PIN-PMN-PT. Superscript T, O and R represent tetragonal, orthorhombic and rhombohedral phase, respectively. P_S and e_{ii} (i = 1, 2, 3) denote spontaneous polarization and dielectric constants measured at fixed stress in the single domain state. The subscript of the dielectric constants follows the definitions in Table 3.1. 45

Table 3.3. Coefficients of the energy function in Eq. (3.1). *T* is temperature in °C. 48

Table 3.4. Dielectric constant, coercive field, remanent polarization and piezoelectric coefficient of 4R and 2R at room temperature. Dielectric constant and piezoelectric coefficient were calculated based on the slope of the *PE* and *SE* curves between 0 and 0.1MV/m, respectively.. 60

VITA

EDUCATION

2015 **M.S., Aerospace Engineering**

University of California, Los Angeles

2012 **B.S., Aircraft Design and Engineering**

Xi'an Jiaotong University, China

EMPLOYMENT HISTORY

2013-2018 **Graduate Student Researcher**

University of California, Los Angeles

2017-2018 **Panel Process and Optics Engineering Intern**

Apple Inc.

PUBLICATIONS

Peng Lv, Christopher S. Lynch. "Phase-field simulation of domain walls in rhombohedral ferroelectric single crystals." Acta Materialia 155: 245-252. (2018)

Peng Lv, Linghang Wang, Christopher S. Lynch. "A phenomenological thermodynamic energy function for PIN-PMN-PT relaxor ferroelectric single crystals." Acta Materialia 137: 93-102. (2017)

Peng Lv, Christopher S. Lynch. "Energetics of domain engineered rhombohedral ferroelectric single crystals." Behavior and Mechanics of Multifunctional Materials and Composites 2017, Proceedings Volume 10165: 101650B. (2017)

Peng Lv, Christopher C. Roberts, Christopher S. Lynch. "Loading rate controlled stress-driven depolarization of PZT 52/48 and 95/5." Proceedings of 20th International Conference on Composite Materials (ICCM-20): 5211-2. (2015)

Aditya Chauhan, Satyanarayan Patel, Shuai Wang, Nikola Novak, Bai-Xiang Xu, **Peng Lv**, Rahul Vaish, Christopher S. Lynch. "Enhanced performance of ferroelectric materials under hydrostatic pressure." Journal of Applied Physics 122: 224105. (2017)

Christopher C. Roberts, **Peng Lv**, Dipankar Ghosh, Thibaud Talon, Christopher S. Lynch. "Intermediate strain rate energy harvesting from the impact of PZT 52/48 and 95/5." Journal of Composite Materials 49: 1863-1871. (2014)

PRESENTATIONS

Peng Lv, Christopher S. Lynch. "Energetics of domain engineered rhombohedral ferroelectric single crystals." SPIE's 24th Annual International Symposium on Smart Structures and Materials + Nondestructive Evaluation and Health Monitoring, Portland, OR, USA. March 25-29, 2017.

Peng Lv, Christopher S. Lynch. "Energetics of domains and phase transformations in ferroelectric single crystals." 13th International Symposium on Ferroic Domains & Micro- to Nano-scopic Structures (ISFD-13), Vancouver, BC, Canada. October 2-6, 2016.

1 Introduction

1.1 Motivation

The past two decades have seen the rapid development of ferroelectric relaxor-$PbTiO_3$ (PT) crystals. They have attracted extensive attentions due to their ultrahigh piezoelectric coefficients (d_{33}>2000pC/N) and electromechanical coupling factors (k_{33}>0.9). As shown in Figure 1.1, the relaxor-PT crystals far outperform state-of-the-art polycrystalline piezoelectric ceramics, exhibiting great potential for replacing polycrystalline ceramics in piezo-based applications such as sensors and actuators.

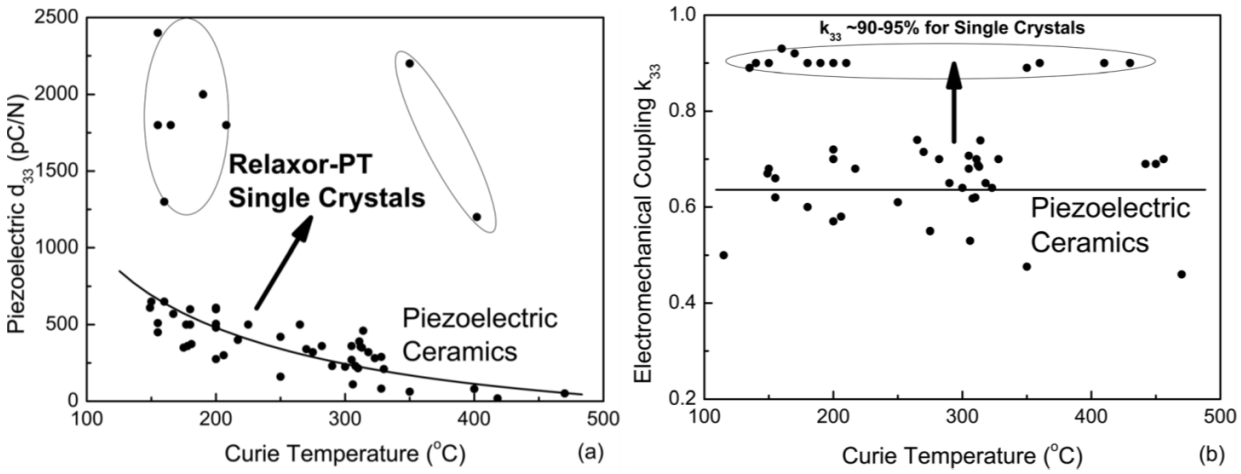

Figure 1.1. Piezoelectric coefficient d_{33} and electromechanical coupling factor k_{33} of relaxor-PT single crystals and piezoelectric ceramics as a function of the Curie temperature [1].

Two typical relaxor-PT crystals are (1-x)$Pb(Mg_{1/3}Nb_{2/3})O_3$-$x$$PbTiO_3$ (PMN-PT) and (1-x)$Pb(Zn_{1/3}Nb_{2/3})O_3$-$x$$PbTiO_3$ (PZN-PT). They were first reported to have ultrahigh piezoelectric coefficients (d_{33}>2500pC/N) and strain levels up to 1.7% through domain engineering by Park and Shrout [2]. Domain engineering is a technique to obtain enhanced

piezoelectric properties, including cutting and poling the crystals along certain directions. These crystals with rhombohedral symmetry have eight spontaneous polarization directions, the <111> directions. Each of them is called a rhombohedral variant. Usually the crystals are poled along specific nonpolar directions, resulting in a set of equivalent domains such that there is no driving force for domain wall motion under subsequent electric field [3]. Figure 1.2 shows examples of domain engineered rhombohedral crystals poled along the [001] and [011] directions. By poling along the [001] direction, only the top four variants are populated in the crystal. This is called a four-rhombohedral-variant (4R) crystal. It exhibits a giant longitudinal piezoelectric coefficient d_{33} and a high electromechanical coupling factor k_{33}. A two-rhombohedral-variant (2R) crystal is obtained by poling along the [011] direction. Large transverse and shear piezoelectric coefficients and electromechanical coupling factors, i.e. d_{32}, k_{32}, d_{15} and k_{15}, are observed in 2R crystals [4].

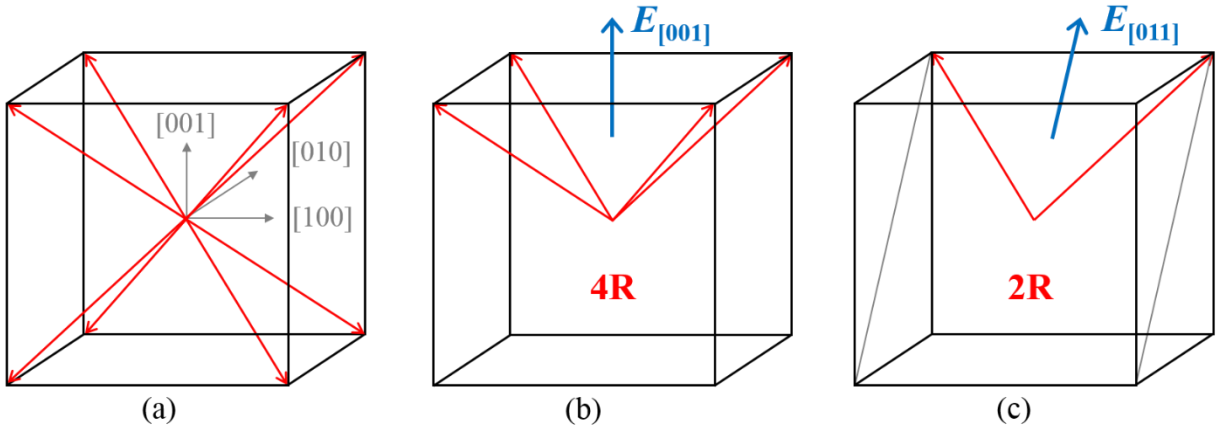

Figure 1.2. Domain engineered rhombohedral crystals. (a) Eight variants of rhombohedral crystals before poling. (b) 4R crystals obtained by poling along the [001] direction. (c) 2R crystals obtained by poling along the [011] direction.

Domain engineered PMN-PT crystals exhibit exceptional piezoelectric properties. However, their relatively low Curie temperature (T_C) and ferroelectric phase transition temperature (T_{RT}) limit their applications. In addition, their low coercive field E_c results in depolarization issues. In some applications a DC bias may be required to maintain the polarization. This results in reduction of sensitivity. Applying a DC bias also adds complexity and cost to the device. Furthermore, their low mechanical quality factors (Q_m~100) restrict their use in resonance based applications [1]. Single crystals with better thermal stability, higher coercive field and lower loss were desired. This led to extensive efforts to develop new crystals. The ternary compositions of xPb($In_{1/2}Nb_{1/2}$)O_3-(1-x-y)Pb($Mg_{1/3}Nb_{2/3}$)O_3-$y$$PbTiO_3$ (PIN-PMN-PT) were found to have higher T_C/T_{RT} and E_c, while maintain similar piezoelectric properties compared to the binary compositions of PMN-PT [5]. With a broader temperature usage range and improved electrical stability, PIN-PMN-PT crystals provide more room for the design of piezo-based devices. The properties of crystals can be further tailored by adding dopants. For example, enhanced mechanical quality factors (Q_m~1000) are observed in Mn doped PIN-PMN-PT crystals, making them potential candidate for high power transducer applications [6].

Both binary compound PMN-PT and ternary compound PIN-PMN-PT may possess different symmetries depending on the composition and external conditions. The highest piezoelectric coefficients are found in compositional ranges close to a morphotropic phase boundary (MPB) for both. The MPB is a compositional boundary separating two ferroelectric phases with different crystallographic symmetries. As shown in Figure 1.3, the MPB of PMN-PT is in the range of 31%-37% PT, separating the rhombohedral phase from the tetragonal phase and coexisting with a monoclinic phase [7], while the MPB of PIN-PMN-PT is in the range of 24%-33% PIN and 30%-33% PT between the rhombohedral phase and the tetragonal phase [8].

Within the compositional ranges close to the MPB, the structure is less stable, making it easier for polarization to rotate. This results in large material response under external excitations and enhanced dielectric and piezoelectric properties.

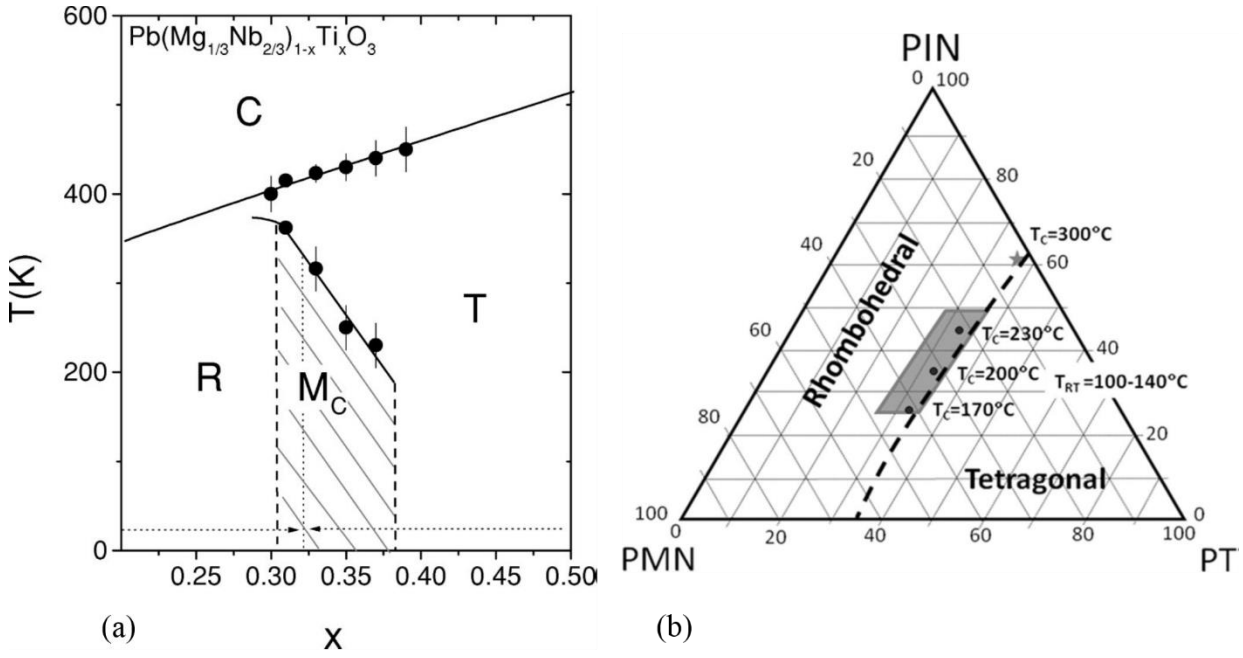

Figure 1.3. (a) Phase diagram of PMN-PT in terms of temperature and composition [7]. The MPB is in the range of 31%-37% PT. (b) Phase diagram of PIN-PMN-PT in terms of composition [8]. The MPB is in the range of 24%-33% PIN and 30%-33% PT.

Research of ferroelectric relaxor-PT crystals is ongoing and focused on improving or tailoring the material properties for piezo-based applications. Material modeling is used to obtain insight into the microstructure and its effects on the material behavior. The phase-field method has proved to be a powerful approach to modeling and predicting mesoscale microstructural evolution [9]. It uses order parameters to describe the domain structure, including domains and domain walls in ferroelectric single crystals. When the material is not in the equilibrium state, there is a driving force for the evolution of the order parameters that minimizes the energy of the system. This is governed by a kinetic relation, the time dependent Ginzburg Landau (TDGL)

equation. The phase-field method has been used to investigate many ferroelectric single crystals. However, most of the previous work was focused on conventional materials with tetragonal symmetry such as $BaTiO_3$, $PbTiO_3$ and certain compositions of lead zirconate titanate (PZT) with high PT content. This is because the phase-field method requires input of a Landau-Devonshire energy function that describes the dielectric, piezoelectric and ferroelectric properties of a single crystal in the single domain state, but this type of energy function was not available for ferroelectric relaxor-PT crystals with rhombohedral symmetry.

This dissertation describes the development of such an energy function for ferroelectric relaxor-PT crystals [10]. A MPB composition of PIN-PMN-PT with rhombohedral symmetry at room temperature was of most interest because the crystals grown in this compositional range exhibit the highest piezoelectric coefficients. In addition, these crystals undergo a series of phase transformations on cooling, including both paraelectric to ferroelectric and ferroelectric to ferroelectric phase transformations. Therefore, the formulation of their energy functions is the most complicated. The method of constructing the energy functions can be extended to compositions away from the MPB because they only undergo paraelectric to ferroelectric phase transformation and the associated energy functions are simplified versions of the one for the MPB compositions. This method also applies to PMN-PT and other relaxor-PT crystals. Then the energy function developed for rhombohedral PIN-PMN-PT crystals was implemented in a phase-field model to study the domain formation and evolution and their contributions to the material properties [11]. Special attention was given to the two types of domain walls that were populated in the rhombohedral crystals, the 71 and 109 domain walls. They showed different responses to external electric field. The minimal domain wall motion in the engineered domain structures was discussed in the context of these results.

The dissertation is constructed as follows. Chapter 1 provides the motivation for this work and a review of background material on piezoelectricity and ferroelectricity. It is followed by an introduction to the thermodynamics of coupled electromechanical systems in Chapter 2. This provides the theoretical basis of the phase-field method. Chapter 3 presents the energy function construction for a MPB composition of PIN-PMN-PT crystals with rhombohedral variants. Based on this energy function, the development of a phase-field model is presented in Chapter 4. Chapter 5 provides the summary and conclusions of the dissertation.

1.2 Background

1.2.1 Piezoelectricity

The term “piezoelectricity” describes the coupling between the mechanical and electrical response of a material. When a piezoelectric material is squeezed, electric charges accumulate on the surface. This is the direct piezoelectric effect, discovered in 1880 by French physicists Jacques and Pierre Curie. Conversely, when an electric field is applied, a piezoelectric material mechanically deforms. This is the converse piezoelectric effect. It was first deduced from thermodynamics by Gabriel Lippmann in 1881, and then experimentally confirmed by the Curie brothers.

Many crystalline materials exhibit piezoelectric behavior, including naturally occurring crystals, synthetic crystals and ceramics. Examples of naturally occurring crystals are Quartz and Rochelle salt [12]. Synthetic materials exhibit much better piezoelectric properties than natural materials. The most common piezoelectric material today, lead zirconate titanate, also known as PZT, is a type of lead-based ceramics. It is produced in the form of both bulk ceramics [13–15] and thin films [16–18]. Concern regarding the toxicity of lead and its compounds is growing. Developing lead-free piezoelectric materials has been a focused research topic and attracted attention from both academia and industries [19,20]. Examples of lead-free materials are sodium potassium niobate ($(K,Na)NbO_3$, or KNN) and sodium bismuth titanate ($(Na_{0.5}Bi_{0.5})TiO_3$, or NBT) [21–24]. Certain polymers represent another important piezoelectric material category. A typical piezoelectric polymer is polyvinylidene fluoride (PVDF) [25,26].

The continued development of piezoelectric materials has led to a huge market of piezo-based products ranging from those for everyday use to more specialized devices. Piezoelectric materials were initially developed for military and marine applications. The first application was an ultrasonic submarine detector during World War I. The discovery of synthetic piezoelectric materials, which exhibited piezoelectric properties much higher than natural piezoelectric materials, led to rapid development of piezoelectric materials and their applications since World War II. The emergence of microelectromechanical systems (MEMS) in the 1980s further catalyzed the development of piezoelectric MEMS devices. Now piezo-based applications such as sensors, actuators, high voltage and power generators, and energy harvesters are widely used in the automotive industry, manufacturing, consumer electronics, medical devices and defense industry. Examples include cigarette lighters, ignition systems, air bag sensors, microphones, speakers, inkjet printers, auto-focus motors of camera, ultrasonic transducers for medical imaging, nondestructive testing, vibration reduction system, etc. The global demand for piezoelectric devices was valued at approximately US $21.60 billion in 2015 [27].

The piezoelectric effect originates from the occurrence of electric dipole moments in the materials. The corresponding crystal classes do not possess a center symmetry. Of the 32 crystal classes, 21 are non-centrosymmetric. All of them are piezoelectric with one exception, the cubic class 432. The piezoelectric crystal classes include triclinic class (1), monoclinic class (2, m), orthorhombic class (222, mm2), tetragonal class (4, $\bar{4}$, 422, 4mm, $\bar{4}$2m), trigonal class (3, 32, 3m), hexagonal class (6, $\bar{6}$, 622, 6mm, $\bar{6}$2m) and cubic class (23, $\bar{4}$3m). The unit cell of lead titanate ($PbTiO_3$) is illustrated as an example in Figure 1.4.

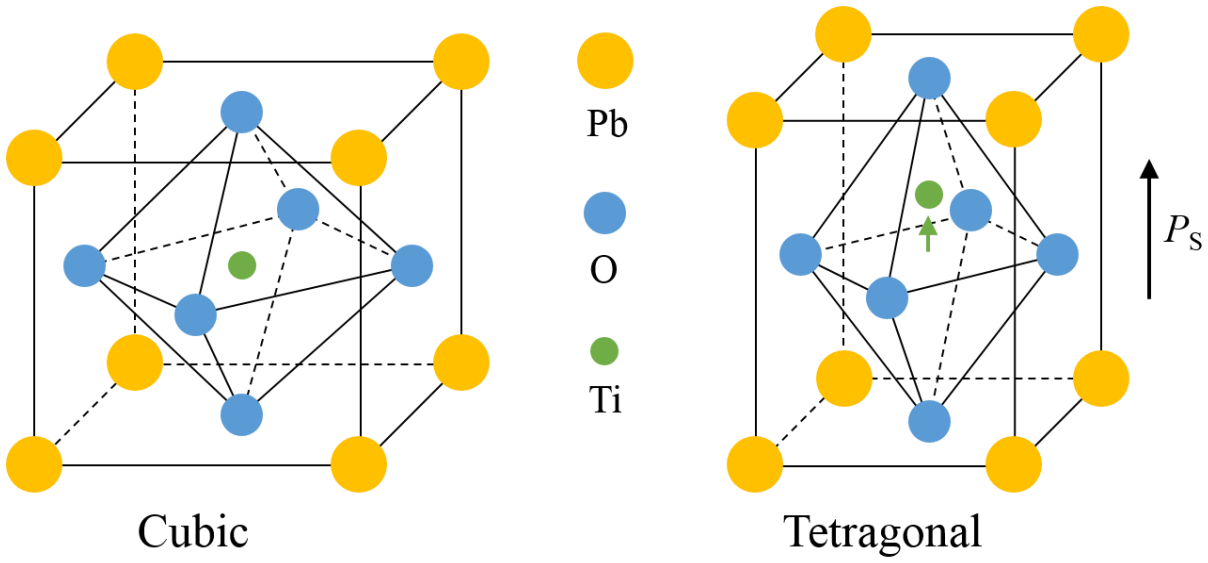

Figure 1.4. A conceptual schematic showing the perovskite structure of lead titanate in the high temperature cubic phase (left) and the low temperature tetragonal phase with spontaneous polarization *P*s (right).

Lead titanate is an ABO_3 perovskite type oxide. The perovskite has an A^{+2} ion at each corner of the unit cell, a B^{+4} ion at the center of the unit cell and an O^{-2} at the center of each face. At high temperature, lead titanate is cubic. When cooled below the Curie temperature, it becomes tetragonal due to the displacement of the central Ti^{+4} ion relative to the surrounding O^{-2} ions. The separation of positive and negative ions gives rise to electric dipole moments. The polarization is defined as the dipole moments per unit volume. The external load, in the way of either mechanical stress or electric field, can change the polarization by inducing a relative displacement of the positive and negative ions. The load also deforms the crystal structure and induces strain. This is the coupling effect of polarization and strain. When the external load is small, the change is reversible and linear. Lines and Glass [28] derived linear constitutive laws for piezoelectric effect from energy considerations. Not only the coupling between strain and polarization is included, but also the elastic and dielectric effects. Depending on the independent

variables used, the piezoelectric constitutive equations have following forms for an isothermal process.

a. Strain-Charge Form

$$\begin{aligned} \varepsilon_m &= s_{mn}^E \sigma_n + d_{im}^\sigma E_i \\ D_i &= d_{im}^E \sigma_m + \kappa_{ij}^\sigma E_j \end{aligned} \tag{1.1}$$

b. Stress-Charge Form

$$\begin{aligned} \sigma_m &= c_{mn}^E \varepsilon_n - e_{im}^\varepsilon E_i \\ D_i &= e_{im}^E \varepsilon_m + \kappa_{ij}^\varepsilon E_j \end{aligned} \tag{1.2}$$

c. Strain-Voltage Form

$$\begin{aligned} \varepsilon_m &= s_{mn}^D \sigma_n + g_{im}^\sigma D_i \\ E_i &= -g_{im}^D \sigma_m + \beta_{ij}^\sigma D_j \end{aligned} \tag{1.3}$$

d. Stress-Voltage Form

$$\begin{aligned} \sigma_m &= c_{mn}^D \varepsilon_n - h_{im}^\varepsilon D_i \\ E_i &= -h_{im}^D \varepsilon_m + \beta_{ij}^\varepsilon D_j \end{aligned} \tag{1.4}$$

Repeated subscripts (i, j = 1, 2, 3; m, n = 1, 2, 3, 4, 5, 6) imply summation (Einstein summation convention). To simplify notation, the tensors are written in the matrix form, following the Voigt convention. The superscripts indicate the variables that are kept constant. All the symbols in Eq. (1.1) – (1.4) are listed in Table 1.1.

Table 1.1. Symbols in piezoelectric constitutive equations.

Symbol	Type	Matrix Size	Unit	Meaning
σ	Rank-2 tensor	6×1	N/m^2	Stress
ε	Rank-2 tensor	6×1	-	Strain
c	Rank-4 tensor	6×6	N/m^2	Elastic stiffness
s	Rank-4 tensor	6×6	m^2/N	Elastic compliance
E	Vector	3×1	V/m	Electric field
D	Vector	3×1	C/m^2	Electric displacement
κ	Rank-2 tensor	3×3	F/m	Dielectric permittivity
β	Rank-2 tensor	3×3	m/F	Inverse dielectric permittivity
d	Rank-3 tensor	3×6	m/V	Piezoelectric coefficient
e	Rank-3 tensor	3×6	C/m^2	Piezoelectric coefficient
g	Rank-3 tensor	3×6	m^2/C	Piezoelectric coefficient
h	Rank-3 tensor	3×6	V/m	Piezoelectric coefficient

Note the piezoelectric coefficients of the same type are thermodynamically equivalent, thus the superscripts can be omitted. This is shown in Eq. (1.5) in the tensor form.

$$\begin{aligned} \mathbf{d}^{\boldsymbol{\sigma}} &= \mathbf{d}^{\mathbf{E}} \\ \mathbf{e}^{\boldsymbol{\varepsilon}} &= \mathbf{e}^{\mathbf{E}} \\ \mathbf{g}^{\mathbf{D}} &= \mathbf{g}^{\boldsymbol{\sigma}} \\ \mathbf{h}^{\mathbf{D}} &= \mathbf{h}^{\boldsymbol{\varepsilon}} \end{aligned} \tag{1.5}$$

The coefficients in different forms of piezoelectric constitutive equations are mutually related. That means given the coefficients of one form, those of the other forms can be theoretically derived. An example of strain-charge form converting to the other three forms is shown in Eq.

(1.6)-(1.8). The superscript *t* and -1 denote the transpose and inverse of the corresponding matrix, respectively.

a. Strain-Charge Form to Stress-Charge Form

$$\begin{aligned} \mathbf{c}^{\mathbf{E}} &= (\mathbf{s}^{\mathbf{E}})^{-1} \\ \mathbf{e} &= \mathbf{d} \cdot (\mathbf{s}^{\mathbf{E}})^{-1} \\ \boldsymbol{\kappa}^{\varepsilon} &= \boldsymbol{\kappa}^{\sigma} - \mathbf{d} \cdot (\mathbf{s}^{\mathbf{E}})^{-1} \cdot \mathbf{d}^{t} \end{aligned} \tag{1.6}$$

b. Strain-Charge Form to Strain-Voltage Form

$$\begin{aligned} \mathbf{s}^{\mathbf{D}} &= \mathbf{s}^{\mathbf{E}} - \mathbf{d}^{t} \cdot (\boldsymbol{\kappa}^{\sigma})^{-1} \cdot \mathbf{d} \\ \mathbf{g} &= (\boldsymbol{\kappa}^{\sigma})^{-1} \cdot \mathbf{d} \\ \boldsymbol{\beta}^{\sigma} &= (\boldsymbol{\kappa}^{\sigma})^{-1} \end{aligned} \tag{1.7}$$

c. Strain-Charge Form to Stress-Voltage Form

$$\begin{aligned} \mathbf{c}^{\mathbf{D}} &= (\mathbf{s}^{\mathbf{D}})^{-1} = (\mathbf{s}^{\mathbf{E}} - \mathbf{d}^{t} \cdot (\boldsymbol{\kappa}^{\sigma})^{-1} \cdot \mathbf{d})^{-1} \\ \mathbf{h} &= \boldsymbol{\beta}^{\varepsilon} \cdot \mathbf{e} = (\boldsymbol{\kappa}^{\sigma} - \mathbf{d} \cdot (\mathbf{s}^{\mathbf{E}})^{-1} \cdot \mathbf{d}^{t})^{-1} \cdot \mathbf{d} \cdot (\mathbf{s}^{\mathbf{E}})^{-1} \\ \boldsymbol{\beta}^{\varepsilon} &= (\boldsymbol{\kappa}^{\varepsilon})^{-1} = (\boldsymbol{\kappa}^{\sigma} - \mathbf{d} \cdot (\mathbf{s}^{\mathbf{E}})^{-1} \cdot \mathbf{d}^{t})^{-1} \end{aligned} \tag{1.8}$$

From Eq. (1.6) and (1.7), it is clear that the dielectric permittivity and elastic compliance measured under different conditions will have different values. The free dielectric permittivity (zero stress) and clamped dielectric permittivity (zero strain) can vary by as much as 50-80% [29]. This variance also applies to the elastic compliance measured under open circuit (zero electric displacement) and short circuit conditions (zero electric field). Therefore, it is important to have a good control of the boundary conditions in the measurements of piezoelectric material properties.

1.2.2 Ferroelectricity

The term “ferroelectricity” describes the characteristics of a material that possesses at least two equilibrium orientations of spontaneous polarization in the absence of external electric field, and in which the spontaneous polarization can be switched between those orientations by an electric field [29]. This term is used in analogy to ferromagnetism despite the fact that most ferroelectric materials do not contain iron, which is the meaning of prefix “ferro”.

Ferroelectric materials are all piezoelectric. However, not all piezoelectric materials are ferroelectric. This is because the dipoles present in some piezoelectric materials (e.g. polymers) are carried by molecular chains or are only present when induced by mechanical stress such as in quartz. These materials do not have spontaneous polarization that can be reversed even though they lack a center of symmetry in their unit cell and can still exhibit piezoelectric effect. As discussed in Section 1.2.1, 20 out of 32 crystal classes exhibit piezoelectricity. Among the 20 piezoelectric classes, 10 of them have a spontaneous polarization that varies with the temperature. This is the pyroelectric effect. Among the 10 pyroelectric classes, if the spontaneous polarization of a material can be reversed by an electric field, then it is called a ferroelectric material.

Many ferroelectric materials have perovskite structure and undergo a phase transformation from a high temperature paraelectric phase to a low temperature ferroelectric phase. The spontaneous polarization is developed with the separation of positive and negative electrical charges upon the paraelectric to ferroelectric phase transformation. This also comes with the spontaneous strain which is related to the spontaneous polarization through the electrostrictive effect [30–32]. The spontaneous polarization of a tetragonal structure can lie along one of six

<001> orientations with equal probability because all six orientations are energetically equivalent. This is corresponding to a potential energy that has an energy well along each of the six orientations. An illustration of the energy landscape of a tetragonal structure is shown in Figure 1.5. The potential energy is plotted as a function of two polarization components P_1 and P_2. Therefore, four energy wells are observed in Figure 1.5(a). Positive work must be done to get the polarization out of one energy well and negative work is done as it slides into another. If the system is conservative, the total work of polarization switching from one energy well to another is zero due to the equivalent depth of the energy wells. Otherwise, heat is generated for a dissipative process. If an electric field is applied along one of the orientations with energy minima (P_2 axis in Figure 1.5(b)), the energy landscape is tilted such that the energy well along the electric field goes deeper while the others elevate. At certain electric field, other energy states become unstable and the associated polarizations switch to the one favored by the electric field. This is called ferroelectric polarization switching. The polarization can be rotated by either 180º or 90º for a tetragonal structure. A similar term is ferroelastic polarization switching. It describes the polarization switching driven by a mechanical load. This is illustrated in Figure 1.5(c) where the mechanical compression applied along one axis (P_2 axis) leads to shallower energy wells in that direction but deeper wells in the perpendicular direction. Thus only 90º polarization switching can be induced via a ferroelastic effect in a tetragonal structure.

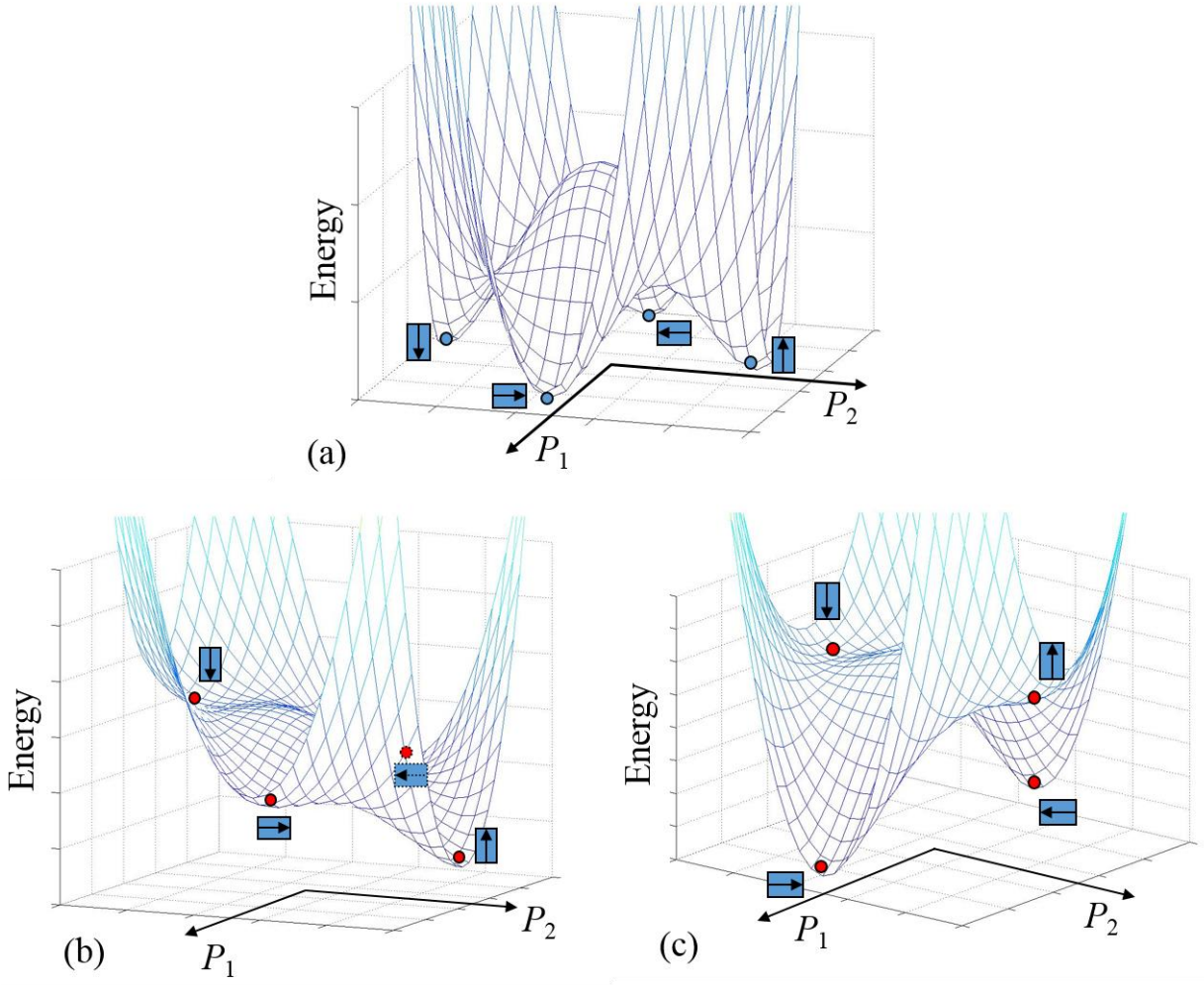

Figure 1.5. Energy landscape of a tetragonal structure plotted as a function of two polarization components P_1 and P_2. (a) Energy landscape with four energy wells representing four spontaneous states of a tetragonal structure in 2 dimensional space. (b) Energy landscape under an electric field applied along the P_2 axis. (c) Energy landscape under mechanical compression applied along the P_2 axis.

Figure 1.5 represents the behavior of polarization in a unit cell. If all the unit cells in a region of a crystal have the same spontaneous polarization, then this region is called a domain. The region between two domains is called a domain wall. The type of domain walls depends on the angle between two polarization directions and the symmetry of crystal structure. Two types of domain walls, i.e. 180º and 90º domain walls, are populated in a tetragonal structure like lead

titanate. A crystal structure with rhombohedral symmetry has eight possible spontaneous polarizations along the <111> directions. This results in three types of domain walls: 71º, 109º and 180º domain walls. Typically, single crystals are composed of many domains separated by domain walls. Bulk ceramics and polycrystalline films are split into many grains and each grain has multiple domains. In the as-grown state, the domains are randomly distributed such that the net polarization is zero. The material is not piezoelectric under this condition. An electric field is required to bring the material into a polar state and exhibit the piezoelectric effect. The process of reorienting the polarizations and aligning the domains with the direction of electric field is called poling. This is usually done with a high electric field (1-10MV/m) at elevated temperatures. For single crystals, a single domain can be obtained if they are poled along one of the polar directions. However, this complete poling is not likely to occur in ceramics because some domains within the grain cannot be reoriented due to the internal stresses and physical constraints imposed by neighboring grains. The schematics of single crystals and ceramics before and after poling are shown in Figure 1.6.

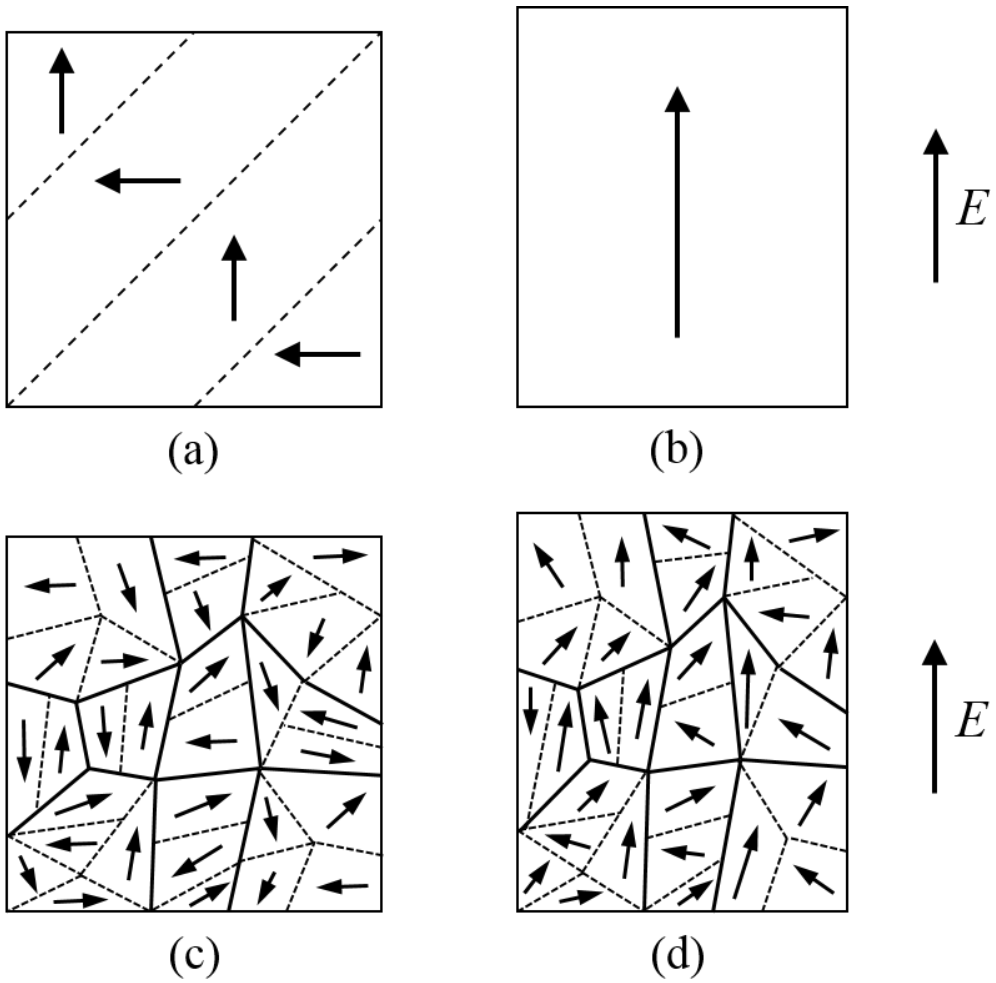

Figure 1.6. The schematics of ferroelectric crystalline materials before and after poling. (a) Single crystals with multiple domains. Dashed lines represent domain walls. (b) A single domain is formed under electric field *E*. (c) Polycrystalline ceramics with multiple grains. Solid lines represent grain boundaries. (d) Domains are reoriented under electric field *E*. Not all domains align with the electric field due to the constraints imposed by neighboring domains and grains.

The most important characteristic of ferroelectric materials is the hysteresis loop of electric displacement or polarization vs electric field. In most ferroelectric materials, the electric displacement D is nearly equal to polarization P. This is because D is related to P and electric field E by the equation $D = P + \kappa_0 E$ where κ_0 is the permittivity of free space. The term $\kappa_0 E$ is negligible compared to P. The polarization hysteresis loop can be obtained from experiments

using a Sawyer-Tower circuit [33]. Figure 1.7(a) are the electric displacement data of lead lanthanum zirconate titanate (8/65/35 PLZT) recorded under a 0.02 Hz cyclic electric field at zero stress [34]. The measurement started from the as-grown state, in which the electric displacement was zero. The loops occurring prior to the fully developed one are not shown in Figure 1.7(a). The hysteresis loop shown here represents the response of poled piezoelectric ceramics. At point A, the material has nonzero polarization at zero electric field. This polarization is called remanent polarization. A negative electric field (opposite to the direction of polarization) is applied. At point B, the polarization begins to switch to the negative direction and the intersection at the electric field axis is called coercive field. At point C the polarization is fully reversed and saturated in the negative direction. Then the electric field is reduced to zero at point D and the material attains the negative remanent polarization. As the electric field turns positive and reaches point E, the negative polarization decreases and begins to reverse. At point F, the polarization is saturated and aligned with the positive electric field. Then the field is reduced to zero and the material returns to point A. The slope at zero field is the linear dielectric permittivity.

In addition to the hysteresis loop of electric displacement vs electric field, polarization switching in ferroelectric materials also results in a hysteretic response of strain under the electric field. The strain hysteresis loop resembles the shape of a butterfly. Thus it is also called a butterfly loop. Figure 1.7(b) are the longitudinal strain data of PLZT recorded simultaneously with the electric displacement in the same experiment [34]. The strain was set to zero in the as-grown state as a reference. Again, the loops occurring prior to the fully developed one are omitted. The lettered points in Figure 1.7(b) correspond to the same letters in Figure 1.7(a). At point A, the material has nonzero strain at zero electric field. This strain is called remanent

strain, corresponding to the remanent polarization. As a negative electric field is applied, the elongation is reduced with ions in the crystal structure experiencing a force pushing them towards the cubic state. When the coercive field is reached at point B, the polarization turns negative. The negative electric field stretches negative polarization and the crystal structure, giving rise to a positive strain at point C. Then the electric field is reduced to zero and the material attains remanent strain at point D. Note point D is corresponding to the negative remanent polarization despite its coincidence with point A, which corresponds to the positive remanent polarization. A positive electric field is applied to the negatively polarized material. The elongation is reduced. When the coercive field is reached at point E, the polarization switches back to being positive. This comes with a positive strain of the crystal structure. The maximum elongation is attained at point F. Then the electric field is reduced to zero and the material returns to point A with positive remanent polarization and strain. The slope at zero electric field is the linear piezoelectric coefficient.

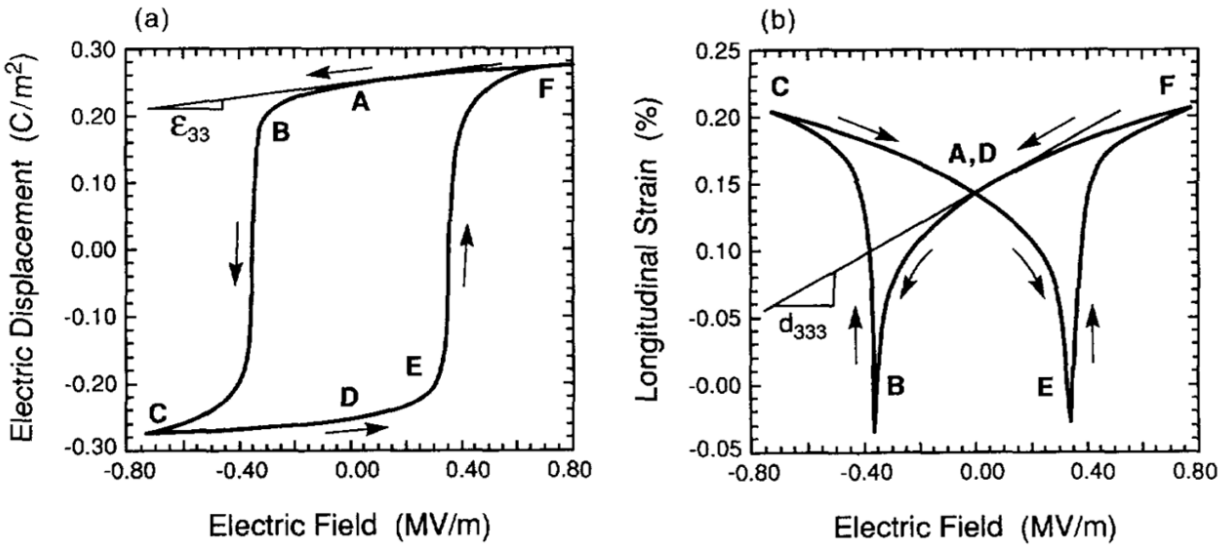

Figure 1.7. The electric displacement and strain hysteresis loops of 8/65/35 PLZT [34]. (a) The hysteresis loop of electric displacement vs electric field. The slope at zero electric field is the linear dielectric permittivity. (b) The

hysteresis loop of longitudinal strain vs electric field. The slope at zero electric field is the linear piezoelectric coefficient.

2 Thermodynamics of ferroelectric materials

The approach to describing ferroelectric material behavior involves the first law and second law of thermodynamics. The first law states the conservation of energy. In order words, the change in the total energy of a closed system is equal to the heat added to the system, plus the work that is done on the system. The second law states that the total entropy of an isolated system can never decrease over time. The discussion of thermodynamics of ferroelectric materials here is based on the work presented by Carka and Lynch [35] and Su and Landis [36].

2.1 External work, heat addition and internal energy

The description of the material within a thermodynamic framework begins with the first law of thermodynamics. The external work includes mechanical work, electrical work and thermal energy added to the system. To calculate the mechanical work done on a material, the distributed surface tractions, distributed body forces and the associated displacements are used. The relations are formulated in a rate form. The rate of mechanical work ($\dot{W}^M$) is the sum of the integral of the traction vector (t_i) and displacement rate ($\dot{u}_i$) over the surface (S) and the integral of the body force (b_i) and displacement rate ($\dot{u}_i$) over the volume (V), Eq. (2.1).

$$\dot{W}^M = \int_S t_i \dot{u}_i dS + \int_V b_i \dot{u}_i dV \tag{2.1}$$

The dot on top of a variable indicates the time derivative. Electrical work is done by moving a charge to a location with different electric potential. The rate of electrical work ($\dot{W}^E$) is found using the rate of surface charge densities ($\dot{\omega}_S$), the rate of volume charge densities ($\dot{\rho}_V$) and the associated electric potentials (ϕ), Eq. (2.2).

$$\dot{W}^E = \int_S \phi \dot{\omega}_S dS + \int_V \phi \dot{\rho}_V dV \tag{2.2}$$

Note that the volume charge density (ρ_V) is zero for ferroelectric materials by treating them as insulators. The thermal energy added to the system can be evaluated as the sum of the heat generated within the volume from an external source and the heat transferred across the surface of the system by heat flux. The rate of heat addition $\dot{\Theta}$ is given by Eq. (2.3).

$$\dot{\Theta} = \int_V \dot{r} dV - \int_S \dot{q}_i n_i dS \tag{2.3}$$

Here $\dot{r}$ is the rate at which heat is generated within the volume from an external source. This does not account for the heat generated by an internal dissipative process. The vector $\dot{q}_i$ is the rate of outward heat flux, representing the heat leaving the system per unit area per unit time. The vector n_i is the unit normal vector of the surface *S*. According to the first law of thermodynamics, the expression for energy balance is

$$\dot{W}^M + \dot{W}^E + \dot{\Theta} = \dot{K} + \dot{U} \tag{2.4}$$

where the left-hand side (LHS) is the sum of all the energy transferred to the system and the right-hand side (RHS) represents where the energy is going. The first term and second term on the RHS represent the rate of kinetic energy ($\dot{K}$) and internal energy ($\dot{U}$) of the system, respectively. Substituting Eq. (2.1), (2.2) and (2.3) into (2.4) yields

$$\begin{aligned} &\int_S t_i \dot{u}_i dS + \int_V b_i \dot{u}_i dV + \int_S \phi \dot{\omega}_S dS + \int_V \phi \dot{\rho}_V dV + \int_V \dot{r} dV - \int_S \dot{q}_i n_i dS \\ &= \frac{d}{dt} \int_V \frac{1}{2} \rho \dot{u}_i \dot{u}_i dV + \int_V \rho \dot{e} dV \end{aligned} \tag{2.5}$$

where $\dot{e}$ is the rate of internal energy density, ρ is the mass density. Using the expressions of surface tractions and surface charge densities, Eq. (2.5) becomes Eq. (2.6).

$$\begin{aligned}&\int_S \sigma_{ij} n_j \dot{u}_i dS + \int_V b_i \dot{u}_i dV - \int_S \phi \dot{D}_i n_i dS + \int_V \phi \dot{\rho}_V dV + \int_V \dot{r} dV - \int_S \dot{q}_i n_i dS \\ &= \frac{d}{dt} \int_V \frac{1}{2} \rho \dot{u}_i \dot{u}_i dV + \int_V \rho \dot{e} dV\end{aligned} \tag{2.6}$$

Using the divergence theorem, the surface integrals can be written as volume integrals, Eq. (2.7).

$$\begin{aligned}&\int_V \left(\sigma_{ij} \dot{u}_i\right)_{,j} dV + \int_V b_i \dot{u}_i dV - \int_V \left(\phi \dot{D}_i\right)_{,i} dV + \int_V \phi \dot{\rho}_V dV + \int_V \dot{r} dV - \int_V \dot{q}_{i,i} dV \\ &= \frac{d}{dt} \int_V \frac{1}{2} \rho \dot{u}_i \dot{u}_i dV + \int_V \rho \dot{e} dV\end{aligned} \tag{2.7}$$

Expanding the partial derivatives, Eq. (2.7) becomes Eq. (2.8).

$$\begin{aligned}&\int_V \left(\sigma_{ij,j} \dot{u}_i + \sigma_{ij} \dot{\varepsilon}_{ij}\right) dV + \int_V b_i \dot{u}_i dV - \int_V \left(\phi_{,i} \dot{D}_i + \phi \dot{D}_{i,i}\right) dV + \int_V \phi \dot{\rho}_V dV + \int_V \dot{r} dV - \int_V \dot{q}_{i,i} dV \\ &= \frac{d}{dt} \int_V \frac{1}{2} \rho \dot{u}_i \dot{u}_i dV + \int_V \rho \dot{e} dV\end{aligned} \tag{2.8}$$

Note the stress does no work on the rigid body rotations. This is shown in Eq. (2.9) and has been applied to Eq. (2.8).

$$\sigma_{ij} \dot{u}_{i,j} = \sigma_{ij} \frac{1}{2}\left(\dot{u}_{i,j} + \dot{u}_{j,i}\right) + \sigma_{ij} \frac{1}{2}\left(\dot{u}_{i,j} - \dot{u}_{j,i}\right) = \sigma_{ij} \dot{\varepsilon}_{ij} \tag{2.9}$$

The equations for mechanical equilibrium, Gauss law and the relation between electric field and electric potential are in Eq. (2.10).

$$\begin{aligned}\sigma_{ij,j} + b_i &= \rho \ddot{u}_i \\ D_{i,i} - \rho_V &= 0 \\ E_i &= -\phi_{,i}\end{aligned} \tag{2.10}$$

Using Eq. (2.10), Eq. (2.8) is simplified to Eq. (2.11).

$$\int_V \sigma_{ij}\dot{\varepsilon}_{ij}dV + \int_V E_i\dot{D}_i dV + \int_V \dot{r}dV - \int_V \dot{q}_{i,i}dV = \int_V \rho\dot{e}dV \tag{2.11}$$

This is the desired expression for the rate of change of the internal energy. The second law of thermodynamics states that the heat added to the system will never be greater than the increase of thermally stored energy. This can be expressed by

$$\int_V \dot{r}dV - \int_V \dot{q}_{i,i}dV \le \int_V T\dot{S}dV \tag{2.12}$$

where the equals sign is adopted for a reversible process. Now we will only consider reversible processes. By shrinking the volume to a point, the integral form of Eq. (2.11) can be expressed in a differential form,

$$\dot{U} = \rho\dot{e} = \sigma_{ij}\dot{\varepsilon}_{ij} + E_i\dot{D}_i + T\dot{S} \tag{2.13}$$

which can also be written as

$$dU = \sigma_{ij}d\varepsilon_{ij} + E_i dD_i + TdS \tag{2.14}$$

Here it is assumed ε_{ij}, D_i and S are independent variables of the internal energy. A difficulty with the expression in Eq. (2.14) is the entropy S cannot be easily controlled while the temperature T is usually controlled. This motivates interchanging the roles of T and S in Eq. (2.14). This can be accomplished using a Legendre transformation to define a new thermodynamic potential, the Helmholtz free energy.

$$\psi = U - TS \quad \rightarrow \quad d\psi = dU - SdT - TdS \tag{2.15}$$

Substituting Eq. (2.14) into Eq. (2.15) yields Eq. (2.16).

$$d\psi = \sigma_{ij} d\varepsilon_{ij} + E_i dD_i - SdT \tag{2.16}$$

Now the independent variables become ε_{ij}, D_i and T. The stress σ_{ij}, electric field E_i and entropy S can be expressed by the following relations, Eq. (2.17).

$$\sigma_{ij} = \frac{\partial \psi}{\partial \varepsilon_{ij}} \qquad E_i = \frac{\partial \psi}{\partial D_i} \qquad S = -\frac{\partial \psi}{\partial T} \tag{2.17}$$

Actually, the three independent variables can be chosen in eight different ways from the conjugate pairs (σ_{ij}, ε_{ij}), (E_i, D_i) and (T, S). This leads to eight thermodynamic potentials listed in Table 2.1 [28].

Table 2.1. Thermodynamic potentials with different independent variables.

Thermodynamic potentials	Differential forms	Independent variables
Internal energy	$dU = \sigma d\varepsilon + EdD + TdS$	ε, D, S
Helmholtz energy	$d\Psi = \sigma d\varepsilon + EdD - SdT$	ε, D, T
Enthalpy	$dH = -\varepsilon d\sigma - DdE + TdS$	σ, E, S
Elastic enthalpy	$dH_1 = -\varepsilon d\sigma + EdD + TdS$	σ, D, S
Electric enthalpy	$dH_2 = \sigma d\varepsilon - DdE + TdS$	ε, E, S
Gibbs energy	$dG = -\varepsilon d\sigma - DdE - SdT$	σ, E, T
Elastic Gibbs energy	$dG_1 = -\varepsilon d\sigma + EdD - SdT$	σ, D, T
Electric Gibbs energy	$dG_2 = \sigma d\varepsilon - DdE - SdT$	ε, E, T

2.2 Energy function formulation based on series expansion

The free energy is a function of each of the independent variables. Though the energy function is still unknown, a well behaved function can be approximated using a Taylor's series expansion. Note that internal energy is also stored in polarization gradients [35]. Therefore, the polarization gradients $P_{i,j}$ should be included as independent variables and there should be some work conjugate variables associated with the gradients [35]. Then the Helmholtz free energy can be expressed as Eq. (2.18).

$$\psi = \psi\left(\varepsilon_{ij}, D_m, P_{i,j}, T\right) = \psi\left(\varepsilon_{ij}, P_m^{\mathrm{FS}}, P_m, P_{i,j}, T\right) \tag{2.18}$$

Here the electric displacement D_m is decomposed into P_m and P_m^{FS} by the relation $D_m = P_m + \kappa_0 E_m$. The variable $P_m^{\mathrm{FS}} = \kappa_0 E_m$ represents the polarization in the free space occupied by the material. κ_0 is the permittivity of free space, E_m is the electric field. The variable P_m represents the polarization in the ferroelectric material. Therefore, the free energy includes both the energy stored in the material and the energy stored in the free space occupied by the material.

The series expansion describes the energy relative to a reference state. Here ferroelectric materials with a perovskite structure are considered. These materials have cubic symmetry in the parent phase above the Curie temperature. When cooled below the Curie temperature, they possess spontaneous polarizations. The reference energy state is taken as the cubic state at a given temperature. This will be a metastable state when below the Curie temperature, but maintains all of the cubic symmetry. If the temperature is held constant, the Helmholtz free energy density can be expanded with respect to the cubic state, Eq. (2.19).

$$\Delta\psi\left(\varepsilon_{ij},P_k,P_k^{\mathrm{FS}},P_{i,j}\right)=\left.\frac{\partial\psi}{\partial\varepsilon_{ij}}\right|_{P,T}\Delta\varepsilon_{ij}+\left.\frac{\partial\psi}{\partial P_k}\right|_{\varepsilon,T}\Delta P_k+\left.\frac{\partial\psi}{\partial P_k^{\mathrm{FS}}}\right|_{\varepsilon,T}\Delta P_k^{\mathrm{FS}}+\left.\frac{\partial\psi}{\partial P_{i,j}}\right|_{\varepsilon,T}\Delta P_{i,j}+$$
$$\frac{1}{2!}\left(\frac{\partial^2\psi}{\partial\varepsilon_{ij}\partial\varepsilon_{kl}}\Delta\varepsilon_{ij}\Delta\varepsilon_{kl}+2\frac{\partial^2\psi}{\partial\varepsilon_{ij}\partial P_k}\Delta\varepsilon_{ij}\Delta P_k+\frac{\partial^2\psi}{\partial P_k\partial P_l}\Delta P_k\Delta P_l+\ldots\right)+ \qquad (2.19)$$
$$\frac{1}{3!}\left(\begin{array}{l}\dfrac{\partial^3\psi}{\partial\varepsilon_{ij}\partial\varepsilon_{kl}\partial\varepsilon_{mn}}\Delta\varepsilon_{ij}\Delta\varepsilon_{kl}\Delta\varepsilon_{mn}+3\dfrac{\partial^3\psi}{\partial\varepsilon_{ij}\partial\varepsilon_{mn}\partial P_k}\Delta\varepsilon_{ij}\Delta\varepsilon_{mn}\Delta P_k+\\ 3\dfrac{\partial^3\psi}{\partial\varepsilon_{ij}\partial P_k\partial P_l}\Delta\varepsilon_{ij}\Delta P_k\Delta P_l+\dfrac{\partial^3\psi}{\partial P_k\partial P_l\partial P_s}\Delta P_k\Delta P_l\Delta P_s+\ldots\end{array}\right)+\ldots$$

Note that all partial derivatives are taken with all other independent variables fixed. This is explicitly denoted in the linear terms in Eq. (2.19), but from here forward will not be indicated. A number of terms in Eq. (2.19) can be eliminated under the following conditions.

a. No odd order terms of polarization are allowed. This is because the system is in a cubic state with symmetry in all directions about this state. A positive polarization change should have the same effect on the energy as a negative polarization change.
b. The strain is a quadratic term. This is corresponding to the linear relation of stress and strain. The coupling of strain and polarization is described by the product of strain term and even order terms of polarization.
c. The free space polarization is a quadratic term that gives rise to the linear contribution of electric field to electric displacement. This term is not coupled to other terms.
d. The polarization gradient term is associated with dipole-dipole interactions. It is taken as a quadratic term only even though the gradient term could be coupled with other terms, which requires higher order contributions.

e. Constant temperature is assumed. In general, temperature dependence needs to be included. The temperature coupling terms are related to the Curie-Weiss behavior above the Curie temperature.

f. It is assumed the energy is relative to the cubic state with zero energy where the strain and polarization are both zero. This enables dropping all of the deltas in Eq. (2.19).

With the restrictions above, the Helmholtz free energy is simplified as Eq. (2.20).

$$\psi\left(\varepsilon_{ij}, P_k, P_k^{\mathrm{FS}}, P_{i,j}\right) = \frac{1}{2!}\left(\begin{array}{l} \dfrac{\partial^2\psi}{\partial\varepsilon_{ij}\partial\varepsilon_{kl}}\varepsilon_{ij}\varepsilon_{kl} + \dfrac{\partial^2\psi}{\partial P_k\partial P_l}P_kP_l + \\ \dfrac{\partial^2\psi}{\partial P_k^{\mathrm{FS}}\partial P_l^{\mathrm{FS}}}P_k^{\mathrm{FS}}P_l^{\mathrm{FS}} + \dfrac{\partial^2\psi}{\partial P_{k,r}\partial P_{l,s}}P_{k,r}P_{l,s} \end{array}\right) + \frac{1}{3!}\left(3\frac{\partial^3\psi}{\partial\varepsilon_{ij}\partial P_k\partial P_l}\varepsilon_{ij}P_kP_l\right) + \ldots \tag{2.20}$$

The variables σ_{ij}, E_k^{eff}, E_k and ξ_{kr} are obtained by taking the partial derivatives of the energy function in Eq. (2.20).

$$\begin{aligned} \sigma_{ij} &= \frac{\partial\psi}{\partial\varepsilon_{ij}} = \frac{1}{2!}\left(2\frac{\partial^2\psi}{\partial\varepsilon_{ij}\partial\varepsilon_{kl}}\varepsilon_{kl}\right) + \frac{1}{3!}\left(3\frac{\partial^3\psi}{\partial\varepsilon_{ij}\partial P_k\partial P_l}P_kP_l\right) + \ldots \\ E_k^{\mathrm{eff}} &= \frac{\partial\psi}{\partial P_k} = \frac{1}{2!}\left(2\frac{\partial^2\psi}{\partial P_k\partial P_l}P_l\right) + \frac{1}{3!}\left(6\frac{\partial^3\psi}{\partial\varepsilon_{ij}\partial P_k\partial P_l}\varepsilon_{ij}P_l\right) + \ldots \\ E_k &= \frac{\partial\psi}{\partial P_k^{\mathrm{FS}}} = \frac{1}{2!}\left(2\frac{\partial^2\psi}{\partial P_k^{\mathrm{FS}}\partial P_l^{\mathrm{FS}}}P_l^{\mathrm{FS}}\right) \\ \xi_{kr} &= \frac{\partial\psi}{\partial P_{k,r}} = \frac{1}{2!}\left(2\frac{\partial^2\psi}{\partial P_{k,r}\partial P_{l,s}}P_{l,s}\right) \end{aligned} \tag{2.21}$$

The first equation in Eq. (2.21) is the stress σ_{ij}. With the polarization fixed, a tensile strain is associated with a tensile stress and a compressive strain with a compressive stress. This is

described by the first term in the stress equation, the linear elastic stiffness. If the strain is held fixed and the polarization varies, the coupling between the polarization and strain should give rise to stress. This is described by the second term, the quadratic term of polarization. The second equation in Eq. (2.21) is the effective electric field E_k^{eff} in the material. It is related to the polarization and also dependent on the strain through the coupling effect. The third equation in Eq. (2.21) is the electric field E_k, which is related to the polarization in the free space through the inverse permittivity of free space. The fourth equation in Eq. (2.21) is the work conjugate variable ξ_{kr} associated with the polarization gradient. Eq. (2.21) can be rewritten as

$$\begin{aligned}
\sigma_{ij} &= C_{ijkl}\varepsilon_{kl} + \frac{1}{2}Q_{ijkl}P_kP_l \\
E_k^{\text{eff}} &= \alpha_{kl}P_l + Q_{ijkl}\varepsilon_{ij}P_l \\
E_k &= \frac{1}{\kappa_0}P_k^{\text{FS}} \\
\xi_{kr} &= G_{krls}P_{l,s}
\end{aligned} \tag{2.22}$$

with C_{ijkl} representing the elastic stiffness coefficients, Q_{ijkl} representing the electrostriction coefficients, α_{kl} representing the dielectric stiffness coefficients and G_{krls} representing the gradient coefficients. These coefficients are related to the partial derivatives in Eq. (2.21).

$$\begin{aligned}
C_{ijkl} &= \frac{\partial^2\psi}{\partial\varepsilon_{ij}\partial\varepsilon_{kl}} \\
Q_{ijkl} &= \frac{\partial^3\psi}{\partial\varepsilon_{ij}\partial P_k\partial P_l} \\
\alpha_{kl} &= \frac{\partial^2\psi}{\partial P_k\partial P_l} \\
\frac{1}{\kappa_0} &= \frac{\partial^2\psi}{\partial P_k^{\text{FS}}\partial P_k^{\text{FS}}} \\
G_{krls} &= \frac{\partial^2\psi}{\partial P_{k,r}\partial P_{l,s}}
\end{aligned} \tag{2.23}$$

With these coefficients, the Helmholtz free energy in Eq. (2.20) can be rewritten as Eq. (2.24).

$$\psi\left(\varepsilon_{ij}, P_k, P_k^{FS}, P_{i,j}\right) = \frac{1}{2}C_{ijkl}\varepsilon_{ij}\varepsilon_{kl} + \frac{1}{2}\alpha_{kl}P_kP_l + \frac{1}{2\kappa_0}P_k^{FS}P_k^{FS} + \frac{1}{2}G_{krls}P_{k,r}P_{l,s} + \frac{1}{2}Q_{ijkl}\varepsilon_{ij}P_kP_l + \ldots \tag{2.24}$$

To generate a multi-well energy landscape to represent multiple spontaneous polarizations, higher even order terms of polarization are needed. The easy way to visualize this is to consider a quadratic polynomial with a negative coefficient and a quartic polynomial with a positive coefficient (Figure 2.1). Add the two together and the resulting function will initially be negative and then go positive as the independent variable increases from zero. There are some locations where the slope is zero. These local minima are the energy wells that can be used to represent the spontaneous polarizations.

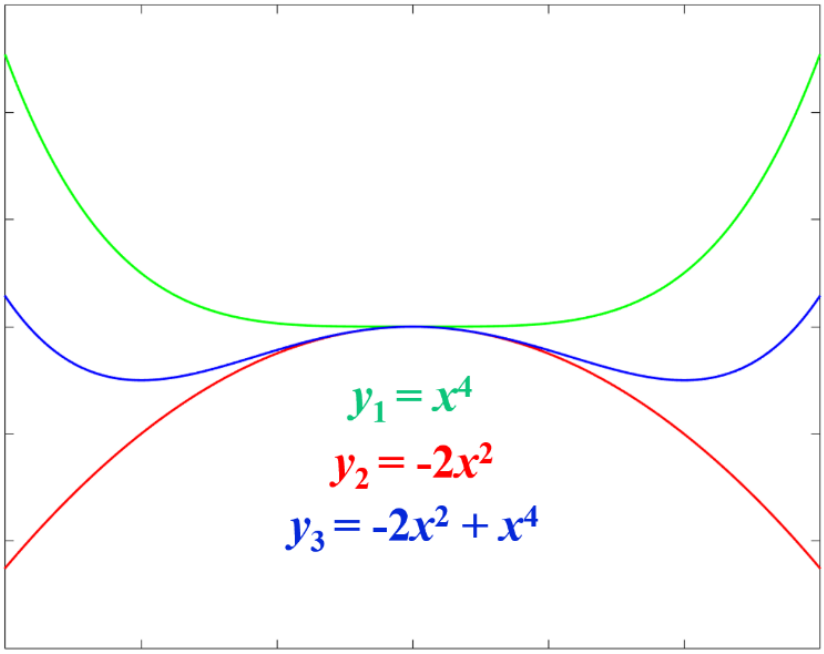

Figure 2.1. The superposition of a quadratic polynomial and a quartic polynomial to generate local minima.

Eq. (2.25) is the updated Helmholtz free energy to which the higher order terms of polarization are added.

$$\psi\left(\varepsilon_{ij}, P_k, P_k^{\mathrm{FS}}, P_{i,j}\right) = \frac{1}{2}C_{ijkl}\varepsilon_{ij}\varepsilon_{kl} + \frac{1}{2}\alpha_{kl}P_kP_l + \frac{1}{2\kappa_0}P_k^{\mathrm{FS}}P_k^{\mathrm{FS}} + \frac{1}{2}G_{krls}P_{k,r}P_{l,s} + \frac{1}{2}Q_{ijkl}\varepsilon_{ij}P_kP_l + \frac{1}{4!}\alpha_{klmn}P_kP_lP_mP_n + \frac{1}{6!}\alpha_{klmnrs}P_kP_lP_mP_nP_rP_s + \ldots \tag{2.25}$$

The energy function can be further modified with additional terms to better represent the ferroelectric materials. For example, the fourth order elasticity tensor must have cubic symmetry with this energy function regardless of the polarization, but a real material exhibits a lower symmetry of elasticity when the spontaneous polarizations are developed below the Curie temperature. This may result in tetragonal, orthorhombic or rhombohedral symmetry. In this case a higher order term in the Helmholtz free energy should be kept that represents the dependence of stiffness on polarization, i.e.

$$\frac{\partial^4\psi}{\partial\varepsilon_{ij}\partial\varepsilon_{kl}\partial P_m\partial P_n}\varepsilon_{ij}\varepsilon_{kl}P_mP_n \tag{2.26}$$

which leads to an stiffness tensor that is a function of polarization in Eq. (2.27).

$$C_{ijkl} + \frac{\partial^2 C_{ijkl}}{\partial P_m\partial P_n}P_mP_n \tag{2.27}$$

Similarly, higher order terms can be added to modify the electrostriction tensor that has cubic symmetry in this formulation. The higher order dependence on polarization enables matching a lower symmetry induced by the spontaneous polarization. Examples of using higher order

coupling terms to describe tetragonal symmetry can be found in the work of Su and Landis [36] and Völker et al. [37].

2.3 Evolution law for polarization

The coefficients of the energy function are all constants. These constants are determined by fitting to the piezoelectric, elastic and dielectric properties of the ferroelectric materials. The coefficient determination process is not trivial. Detailed discussion about the energy function formulation and the coefficient determination for a composition of PIN-PMN-PT crystals is presented in Chapter 3. Once these constants are obtained, the equilibrium state under a set of external loads can be determined. A kinetic relation is required to govern the process of the material approaching the equilibrium state. This is known as the time dependent Ginzburg-Landau (TDGL) equation. A generalized form of it is shown in Eq. (2.28).

$$\left(\frac{\partial \psi}{\partial P_{i,j}}\right)_{,j} - \frac{\partial \psi}{\partial P_i} + \gamma_i = \beta_{ij}\dot{P}_j \tag{2.28}$$

This is derived by Su and Landis [36] who proposed a set of micro-forces and the associated governing balance laws following the work of Fried and Gurtin [38–40]. The inverse mobility tensor β_{ij} is positive definite. Most of the time it is assumed $\beta_{ij} = \beta\delta_{ij}$ ($\beta \geq 0$) for materials with cubic symmetry above the Curie temperature. An external micro-force vector γ_i is introduced to describe the power density expended on the material by external sources. An internal micro-force vector π_i is also introduced to describe the power density expended by material internally, Eq. (2.29).

$$\pi_i = -\frac{\partial \psi}{\partial P_i} - \beta_{ij}\dot{P}_j \tag{2.29}$$

The term on the RHS of Eq. (2.28) represents the viscous response of the polarization. It governs the rate at which the polarization responds to the driving force at a point in the material. Note

that the viscous parameter β should be zero for equilibrium state. However, in practice we usually need to allow the material to evolve along non-equilibrium paths. Therefore β is used as a free numerical parameter to drive the solution and is gradually reduced to zero at equilibrium.

2.4 Finite element implementation

The evolution of polarization field is described by the TDGL equation. In addition, the ferroelectric material behavior also obeys the mechanical equilibrium and Gauss law. The governing equations and boundary conditions of mechanical fields are

$$\begin{cases} \sigma_{ij,j} = 0 & \text{in } V \\ \sigma_{ij} = C_{ijkl}\varepsilon_{kl} & \text{in } V \\ \varepsilon_{kl} = \dfrac{1}{2}\left(u_{k,l} + u_{l,k}\right) & \text{in } V \\ \sigma_{ij} n_j = t_i^0 & \text{on } S \\ u_i = u_i^0 & \text{on } S \end{cases} \tag{2.30}$$

The governing equations and boundary conditions of electric fields are

$$\begin{cases} D_{i,i} = 0 & \text{in } V \\ D_i = \kappa_0 E_i + P_i & \text{in } V \\ E_i = -\phi_{,i} & \text{in } V \\ D_i n_i = -\omega_s^0 & \text{on } S \\ \phi_i = \phi_i^0 & \text{on } S \end{cases} \tag{2.31}$$

The superscript 0 in Eq. (2.30) and (2.31) represents the quantities that are prescribed. Here it is assumed the system reaches mechanical equilibrium instantaneously for a given polarization field but varies slowly with respect to the speed of light (quasi-static electromagnetic approximation). The inertial terms and body forces are neglected. There is no volume charge density within the material.

The three groups of governing equations (TDGL, mechanical equilibrium and Gauss law) need to be solved simultaneously for a fully coupled model. This can be done by using a semi-implicit Fourier-spectral method [41], a finite difference method [42] or a finite element method

[36,43]. The finite element method is adopted here because it allows for analysis of arbitrary geometries with non-periodic or periodic boundary conditions. It also makes it possible to use commercial FEA software packages that allow you to program your own weak forms. The mechanical displacement, polarization and electric potential are used as nodal degrees of freedom. The field quantities are interpolated from the nodal quantities **d** with the shape functions **N** such that

$$\begin{Bmatrix} u_i \\ \phi \\ P_i \end{Bmatrix} = \mathbf{Nd} \tag{2.32}$$

The shape function matrix **N** must meet the requirements for C_0 continuous elements [44]. In order to model the polarization evolution, a time-dependent analysis is required. At a given time step, the polarization rate is

$$\dot{P}_i = \frac{P_i^{t+\Delta t} - P_i^t}{\Delta t} \tag{2.33}$$

The field quantities are

$$\begin{aligned} u_i &= \alpha u_i^{t+\Delta t} + (1-\alpha) u_i^t \\ \phi &= \alpha \phi^{t+\Delta t} + (1-\alpha) \phi^t \\ P_i &= \alpha P_i^{t+\Delta t} + (1-\alpha) P_i^t \end{aligned} \tag{2.34}$$

The superscript denotes the time step at which the field is solved. The parameter α between 0 and 1 describes how the solution fields are interpolated in time. When $\alpha = 0$ the first-order accurate forward Euler integration scheme is recovered; $\alpha = 1$ represents the first-order accurate backward

Euler scheme that allows for enhanced numerical stability with larger time increments; $\alpha = 0.5$ is the second-order accurate Crank-Nicholson method.

Given a known set of nodal values at time t, a set of non-linear equations (Eq. (2.35)) in terms of nodal degrees of freedom at time $t + \Delta t$ are obtained by substituting the finite element interpolations (Eq. (2.32)) and the time integration approximations (Eq. (2.33) and (2.34)) into the governing equations.

$$\mathbf{B}\left(\mathbf{d}^{t+\Delta t}\right) = \mathbf{F} \tag{2.35}$$

These nonlinear equations can be solved with Newton-Raphson method,

$$\begin{aligned} &\left.\frac{\partial \mathbf{B}}{\partial \mathbf{d}}\right|_{\mathbf{d}_i^{t+\Delta t}} \Delta \mathbf{d}_i = \mathbf{F} - \mathbf{B}\left(\mathbf{d}_i^{t+\Delta t}\right) \\ &\mathbf{d}_{i+1}^{t+\Delta t} = \mathbf{d}_i^{t+\Delta t} + \Delta \mathbf{d}_i \end{aligned} \tag{2.36}$$

where subscript i is the step counter in the Newton-Raphson iteration. The iteration is carried out until the solution fields are converged at time $t + \Delta t$. Then the procedure continues to run through time and the evolution history in terms of the solution fields can be obtained.

3 Energy function development for ferroelectric single crystals

3.1 Introduction

In this work Landau-Devonshire energy functions were developed for ferroelectric single crystals. The coefficients of the energy functions were determined through extensive fitting to the experimental data. The energy functions were validated by comparison of simulated temperature induced phase transformations, coercive fields, remanent polarizations, dielectric constants and piezoelectric coefficients with measured values.

Landau-Devonshire energy functions represent the structural free energy of a unit cell. This thermodynamics based theory was developed by Devonshire [45,46], who applied the Ginzburg-Landau theory of phase transformation to $BaTiO_3$ crystals using a 6^{th} order polynomial of polarization. Bell and Cross [47] used a modified form of Devonshire energy function to model field-driven ferroelectric phase changes in $BaTiO_3$. Amin et al. [48] developed a 6^{th} order energy function with coefficients determined at various compositions across the phase diagram of PZT. Haun et al. introduced a 6^{th} order energy function for $PbTiO_3$ [49] and presented a two-sublattice model for $PbZrO_3$ [50] following Kittel's theory of antiferroelectricity [51]. The discovery of a monoclinic phase in PZT by Noheda et al. [52] challenged the traditional 6^{th} order expansion form of the Landau-Devonshire energy. Vanderbilt and Cohen [53] proposed that energy functions allowing monoclinic and triclinic phases require terms up to the 8^{th} and 12^{th} order, respectively. An 8^{th} order polynomial was constructed by Li et al. [54], which is applicable to $BaTiO_3$ thin films under large strains. Wang et al. [55] used additional temperature dependent coefficients in an 8^{th} order polynomial to achieve a better description of the dielectric properties

of $BaTiO_3$ around and above the Curie temperature. Methods have been developed by Heitmann and Rossetti [56,57] to interpolate between end members to obtain energy functions that reproduce the morphotropic phase boundary (MPB) effects. Völker et al. [37,58] presented an adjustment procedure of the energy function coefficients of $PbTiO_3$ and PZT based on first-principles calculations.

Although ferroelectric relaxor single crystals with rhombohedral symmetry are of considerable technological importance, Landau-Devonshire energy functions that reproduce their behavior have not yet been introduced. These are needed for phase-field models [9] such as those presented by Hu and Chen [59,60], Zhang and Bhattacharya [42,61], Su and Landis [36], and many others that are used to gain deeper understanding of the energy landscapes, of how energy landscapes are affected by composition and external excitations, of domain formation and evolution, and of domain engineered structures.

Ferroelectric relaxor single crystals, such as certain compositions of PMN-PT and PZN-PT, have extraordinarily large piezoelectric coefficients and high electromechanical coupling factors when cut and poled in certain orientations. The ternary compound PIN-PMN-PT was developed to increase the phase transition temperature and coercive field of these crystals without sacrificing their superior piezoelectric properties. Compositions with the highest piezoelectric coefficients are generally found in rhombohedral phase close to a morphotropic phase boundary. These rhombohedral crystals possess spontaneous polarizations along eight <111> pseudo-cubic directions. Each of the eight possible polarization directions is referred to as a crystal variant. A domain is a region in the crystal where neighboring cells in the lattice are all of the same variant. The boundary between two different domains is a domain wall. In general, ferroelectric single crystals have multiple domains and domain walls, giving rise to complex domain structures.

Domain engineering [2,62,63] involves cutting and poling the crystals in orientations that do not produce a driving force for domain wall motion when an electric field is applied within limits governed by polarization reversal, field induced phase transformations and dielectric breakdown.

The work presented herein draws from many experimental results reported in the literature. Ferroelectric relaxor single crystals occur in different phases, and they can be cut and poled in different orientations. Results reported in the literature typically introduce a Cartesian coordinate system with the x_3 direction aligned with the volume average polarization direction. A notation is adopted here that is consistent with most of the reported results. The orientation of the Cartesian coordinate system x_1-x_2-x_3 for each crystal cut is defined in terms of the pseudo-cubic coordinate system and the associated Miller indices. The variant and phase structure, the poling direction, the resulting macroscopic symmetry, the associated Cartesian coordinate system and the variants present in the domain engineered crystals are given in Table 3.1. The variant and phase structure are identified by a number indicating the number of variant types present followed by a letter indicating the phase. Poling along the [001], [110] or [111] direction induces domain structures in the rhombohedral crystals that have certain enhanced volume average properties. The rhombohedral crystals poled along the [001] direction have an enhanced longitudinal piezoelectric coefficient while those poled along the [110] direction have an enhanced transverse piezoelectric coefficient. The [111] poled single domain state exhibits a high shear piezoelectric coefficient.

Table 3.1. Nomenclature used to describe ferroelectric relaxor single crystals. 1T, 1O and 1R represent tetragonal, orthorhombic and rhombohedral crystals in the single domain state. 2R and 4R are domain engineered rhombohedral crystals with two and four variants.

Variant and phase structure	Poling direction	Macroscopic symmetry	Cartesian coordinate system $x_1 - x_2 - x_3$	Variants
1T	[001]	4*mm*	[100] – [010] – [001]	[001]
1O	[110]	*mm*2	[-110] – [001] – [110]	[110]
1R	[111]	3*m*	[1-10] – [11-2] – [111]	[111]
2R	[110]	*mm*2	[-110] – [001] – [110]	[111], [11-1]
4R	[001]	4*mm*	[100] – [010] – [001]	[111], [1-11], [-111], [-1-11]

3.2 Landau-Devonshire energy function

In this section we introduce the 10^{th} order Landau-Devonshire energy function suitable for describing the dielectric, piezoelectric and ferroelectric properties of PIN-PMN-PT observed on cooling through the sequence of cubic (C) → tetragonal (T) → orthorhombic (O) → rhombohedral (R) phase transformations, and the effects of applied electric field and temperature on the polarization switching in domain engineered rhombohedral crystals.

3.2.1 Energy function formulation

In perovskite ferroelectric single crystals, the high temperature cubic paraelectric phase distorts into a ferroelectric phase with lower symmetry as it is cooled. Taking the cubic phase as the reference state with zero energy, the Landau-Devonshire energy function is expressed as a series expansion of polarization up to the 10^{th} order under zero stress conditions. The polynomial only contains even order terms because the energy must remain invariant for any orthogonal transformation of the polarization components in the prototype cubic phase. Material symmetry arguments are used to reduce the number of terms, resulting in Eq. (3.1),

$$
\begin{aligned}
f_{\mathrm{LD}} = {} & \alpha_1\left(P_1^2+P_2^2+P_3^2\right)+\alpha_{11}\left(P_1^4+P_2^4+P_3^4\right)+\alpha_{12}\left(P_1^2P_2^2+P_1^2P_3^2+P_2^2P_3^2\right) \\
& +\alpha_{111}\left(P_1^6+P_2^6+P_3^6\right)+\alpha_{112}\left[P_1^2\left(P_2^4+P_3^4\right)+P_2^2\left(P_1^4+P_3^4\right)+P_3^2\left(P_1^4+P_2^4\right)\right] \\
& +\alpha_{123}P_1^2P_2^2P_3^2+\alpha_{1111}\left(P_1^8+P_2^8+P_3^8\right) \\
& +\alpha_{1112}\left[P_1^6\left(P_2^2+P_3^2\right)+P_2^6\left(P_1^2+P_3^2\right)+P_3^6\left(P_1^2+P_2^2\right)\right] \\
& +\alpha_{1122}\left(P_1^4P_2^4+P_1^4P_3^4+P_2^4P_3^4\right)+\alpha_{1123}\left(P_1^2P_2^2P_3^4+P_1^2P_2^4P_3^2+P_1^4P_2^2P_3^2\right) \\
& +\alpha_{11111}\left(P_1^{10}+P_2^{10}+P_3^{10}\right) \\
& +\alpha_{11112}\left[P_1^8\left(P_2^2+P_3^2\right)+P_2^8\left(P_1^2+P_3^2\right)+P_3^8\left(P_1^2+P_2^2\right)\right] \\
& +\alpha_{11122}\left[P_1^6\left(P_2^4+P_3^4\right)+P_2^6\left(P_1^4+P_3^4\right)+P_3^6\left(P_1^4+P_2^4\right)\right] \\
& +\alpha_{11223}\left(P_1^4P_2^4P_3^2+P_1^4P_2^2P_3^4+P_1^2P_2^4P_3^4\right)+\alpha_{11123}\left(P_1^2P_2^2P_3^6+P_1^2P_2^6P_3^2+P_1^6P_2^2P_3^2\right)
\end{aligned}
\tag{3.1}
$$

where P_i (i = 1, 2, 3) are the orthogonal components of polarization along the axes of the pseudo-cubic unit cell and α's are the coefficients of the energy function.

With mechanical stress applied, the elastic energy needs to be included. The stresses and stiffness coefficients can be obtained by taking the first and second derivatives of the elastic energy with respect to strains, respectively. The elastic stiffness tensor for the high temperature paraelectric phase has cubic symmetry. Thus cubic elastic stiffness tensor is normally used for ferroelectric phases. In order to have a more accurate description of the elastic energy for ferroelectric crystals with lower symmetry, higher order terms can be added to address the coupling with polarization. These additional terms result in modification of stiffness coefficients and matching a lower symmetry of the elastic stiffness tensor. The stiffness coefficients with lower symmetry have been experimentally characterized and these data can be used for a better description of the elastic energy. This work did not address the stiffness coefficients.

3.2.2 Material properties

Finding a consistent set of coefficients for the energy function requires addressing large uncertainties in the data reported in the literature. Single crystals are cut from boules that have a compositional gradient and the composition is often estimated, not directly measured. As a result, the composition has a degree of uncertainty not reported, and the measured properties can lie within a fairly broad range for the same reported composition. Further, the property measurements on a MPB composition at multiple temperatures with different cuts that produce a single domain state in each ferroelectric phase are not available, posing challenges to obtaining a complete set of characterization data. To address this, a qualitatively observed composition-temperature equivalence was used. As temperature increases, the rhombohedral crystal undergoes a phase transformation to the orthorhombic phase and with further temperature increase to the tetragonal phase. As the PT content increases, the material behavior shifts from the rhombohedral phase toward the MPB at a fixed temperature, and with further increase to the tetragonal phase. The trends in material properties changing with the temperature and composition are similar. The approach to using the composition-temperature equivalence is described in Figure 3.1. Most available data were measured at room temperature on different compositions. These are marked by the orange dashed line in Figure 3.1. However, the data for a single composition at multiple temperatures (marked by the red dashed line) are needed to determine the coefficients of the energy function. In this work, data were taken from the literature where possible, and approximations of the properties based on the proximity to the MPB were made when data were not available. Since the high temperature properties of the tetragonal phase (light blue dot) and orthorhombic phase (light green dot) could not be found, we approximated those properties at elevated temperatures by examining the data collected at room

temperature with compositional modification resulting in a stable tetragonal phase (blue dot) or orthorhombic phase (green dot) with higher PT content. The single domain properties for the stable rhombohedral phase (red dot) at room temperature are approximated based on the measurements of a composition away from the MPB (dark red dot). To account for the increase of the dielectric constants with the composition approaching the MPB [64–66], a factor of 1.5 was used to adjust the dielectric constants and found to work well as a fitting parameter. The data that were used to determine the coefficients of the energy function for a composition of PIN-PMN-PT right on the rhombohedral side of the MPB at room temperature are listed in Table 3.2.

Table 3.2. Data used to determine the coefficients of the energy function for a MPB composition of PIN-PMN-PT. Superscript T, O and R represent tetragonal, orthorhombic and rhombohedral phase, respectively. P_S and e_{ii} (i = 1, 2, 3) denote spontaneous polarization and dielectric constants measured at fixed stress in the single domain state. The subscript of the dielectric constants follows the definitions in Table 3.1.

Quantities	Values	Units	Quantities	Values	Units
C	1.48×10^{6} [f]	°C	T_2^*	25[c]	°C
T_0	182[e]	°C	P_S^O (T_2^*)	0.455[g]	C/m^2
T_C	192[a]	°C	e_{33}^O (T_2^*)	1500[c]×1.5	-
T_1^*	25[b]	°C	e_{11}^O(T_2^*)	8070[c]×1.5	-
P_S^T (T_1^*)	0.43[b]	C/m^2	e_{22}^O(T_2^*)	30000[c]×1.5	-
e_{33}^T (T_1^*)	1090[b]×1.5	-	T_3	25[d]	°C
e_{11}^T (T_1^*)	15000[b]×1.5	-	P_S^R (T_3)	0.47[h]	C/m^2
T_{OT}	118[a]	°C	e_{33}^R(T_3)	650[d]×1.5	-
T_{RO}	93[a]	°C	e_{11}^R(T_3)	5800[d]×1.5	-

a: Reference [67]; b: Reference [68]; c: Reference [69]; d: Reference [70];

e: No experimental data available. Estimated based on T_C;

f: No experimental data available. Typical values of C are on the order of $10^5 \sim 10^6$;

g: No experimental data available. Estimated based on the average of P_S^T (T_1^*) and P_S^R (T_3);

h: No experimental data available. Estimated based on $P_S^R \approx \sqrt{3}P_S^{4R} \approx \sqrt{3}P_S^{2R}/\sqrt{2}$.

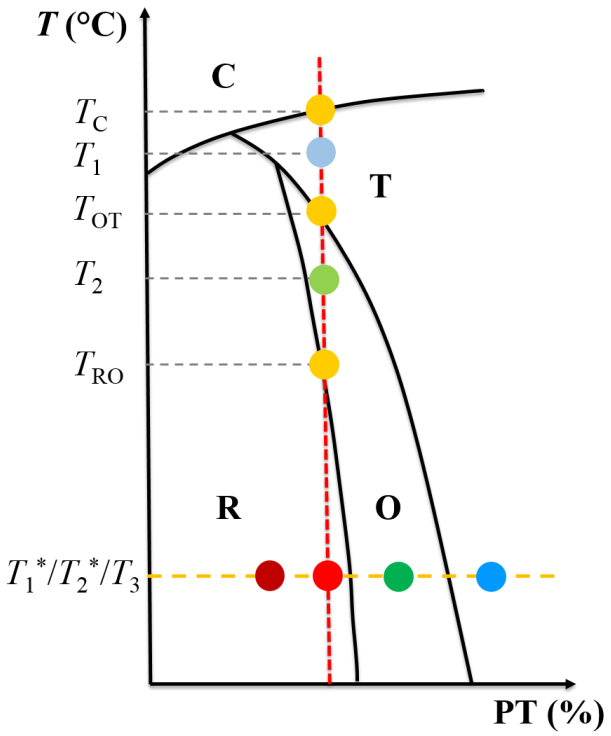

Figure 3.1. A schematic of the composition-temperature phase diagram of PIN-PMN-PT. C, T, O and R denote cubic, tetragonal, orthorhombic and rhombohedral phase, respectively. Vertical red dashed line represents the MPB composition for which the energy function is developed. The horizontal orange dashed line represents the compositions that have been experimentally characterized. A typical MPB composition contains 32%-33% of PT.

3.2.3 Coefficient determination

There are in total 15 coefficients in the proposed energy function. Two coefficients α_{11111} and α_{11122} were found not to have much effect on the material behavior and were thus set to zero. This simplified the coefficient determination process and was found to provide sufficient degrees of freedom to describe the properties involving different symmetries. Only α_1 was taken to be temperature dependent. The remaining 12 coefficients were assumed to be temperature independent. The coefficient α_1 was determined by applying the Curie-Weiss law above the Curie temperature though it is not an exact representation of relaxors,

$$\alpha_1 = \frac{(T - T_0)}{2e_0 C} \tag{3.2}$$

where T, e_0 and C are temperature, permittivity of free space and Curie constant, respectively. T_0 is the Curie-Weiss temperature. It is not equal to the Curie temperature for a first order transition between the paraelectric phase and ferroelectric phase. Typically T_0 is slightly lower than the Curie temperature.

The remaining 12 coefficients were divided into three groups according to the symmetry of ferroelectric phases. First tetragonal symmetry was considered. Taking P_3 as the polar direction of the single domain state and setting P_1 and P_2 to zero, the energy function was reduced to having only three unknown coefficients α_{11}, α_{111} and α_{1111}. They were determined by fitting to the polarization and dielectric constant of the tetragonal phase at T_1 as well as the Curie temperature T_C. Next orthorhombic symmetry was utilized with a tensor transformation of the energy function to a local coordinate system defined as 1O in Table 3.1. Setting the two polarization components along the nonpolar directions to zero, the energy function only contains unknown coefficients α_{12}, α_{112}, α_{1112}, α_{1122} and α_{11112}. They were determined from the polarization and dielectric constants of the orthorhombic phase at T_2 and the phase transition temperature T_{OT} between the tetragonal phase and the orthorhombic phase. Finally by transforming the energy function to another local coordinate system defined as 1R in Table 3.1 and setting the two transverse polarization components to zero, the remaining unknown coefficients α_{123}, α_{1123}, α_{11223} and α_{11123} were determined from the rhombohedral phase properties at T_3 (room temperature). The obtained coefficients are listed in Table 3.3. More details about the coefficient determination process are provided in the appendix.

Table 3.3. Coefficients of the energy function in Eq. (3.1). *T* is temperature in °C.

Coefficients	Values	Units	Coefficients	Values	Units
α_1	3.816×10^4 (*T*-182)	$C^{-2}m^2N$	α_{1122}	-1.993×10^9	$C^{-8}m^{14}N$
α_{11}	-1.212×10^7	$C^{-4}m^6N$	α_{1123}	-3.956×10^{10}	$C^{-8}m^{14}N$
α_{12}	-1.285×10^7	$C^{-4}m^6N$	α_{11112}	-8.865×10^9	$C^{-10}m^{18}N$
α_{111}	9.424×10^7	$C^{-6}m^{10}N$	α_{11223}	1.717×10^{11}	$C^{-10}m^{18}N$
α_{112}	1.550×10^8	$C^{-6}m^{10}N$	α_{11123}	8.946×10^{10}	$C^{-10}m^{18}N$
α_{123}	4.716×10^9	$C^{-6}m^{10}N$	α_{11111}	0	$C^{-10}m^{18}N$
α_{1111}	3.190×10^7	$C^{-8}m^{14}N$	α_{11122}	0	$C^{-10}m^{18}N$
α_{1112}	2.521×10^9	$C^{-8}m^{14}N$			

3.3 Simulated thermal properties

The proposed energy function was used to simulate the temperature induced phase transformations. Figure 3.2(a) is a schematic of a pseudo-cubic unit cell. The three ferroelectric phases T, O and R can be described with the polarization in the diagonal plane (1-10). This enables a 2D representation of the energy function in this plane using the axis $P_{12} = (P_1+P_2)/\sqrt{2}$ and the axis P_3. There can be multiple energy wells at a single temperature. The shallower wells represent the metastable states and the deepest wells represent the stable states. Thermal fluctuations can cause the polarization to move from metastable to stable states, and stress or electric field can tilt the entire energy landscape and change the energy minima. When the minimum energy occurs in the P_3 direction ($P_{12} = 0$), the tetragonal phase is stable. When the minimum energy occurs in the P_{12} direction ($P_3 = 0$), the orthorhombic phase is stable. When the minimum energy corresponds to the polarization in the [111] direction, the rhombohedral phase is stable.

The energy density is plotted as a function of P_{12} and P_3 in Figure 3.2. Only one energy well is present, at zero polarization, when above the Curie temperature (Figure 3.2(b)). This represents the paraelectric phase with zero spontaneous polarization. When cooled below the Curie temperature (Figure 3.2(c)), the crystal possesses a multi-well landscape with energy wells at nonzero polarizations in the directions of all three ferroelectric phases. Following an assumption made by many authors [3,48–50,54,71], the depth of the energy wells was used to indicate the stable phase and the crystal was assumed to transform to the phase with the lowest energy due to the thermal fluctuations taking it out of the metastable state. This approach neglects the hysteresis in the phase transformations associated with increasing vs decreasing temperature. As shown in Figure 3.2(c), the lowest energy at room temperature is associated with

polarization in the <111> directions. This means the crystal is in the rhombohedral phase at this temperature. The shallower wells represent the tetragonal phase and the orthorhombic phase with higher energy levels.

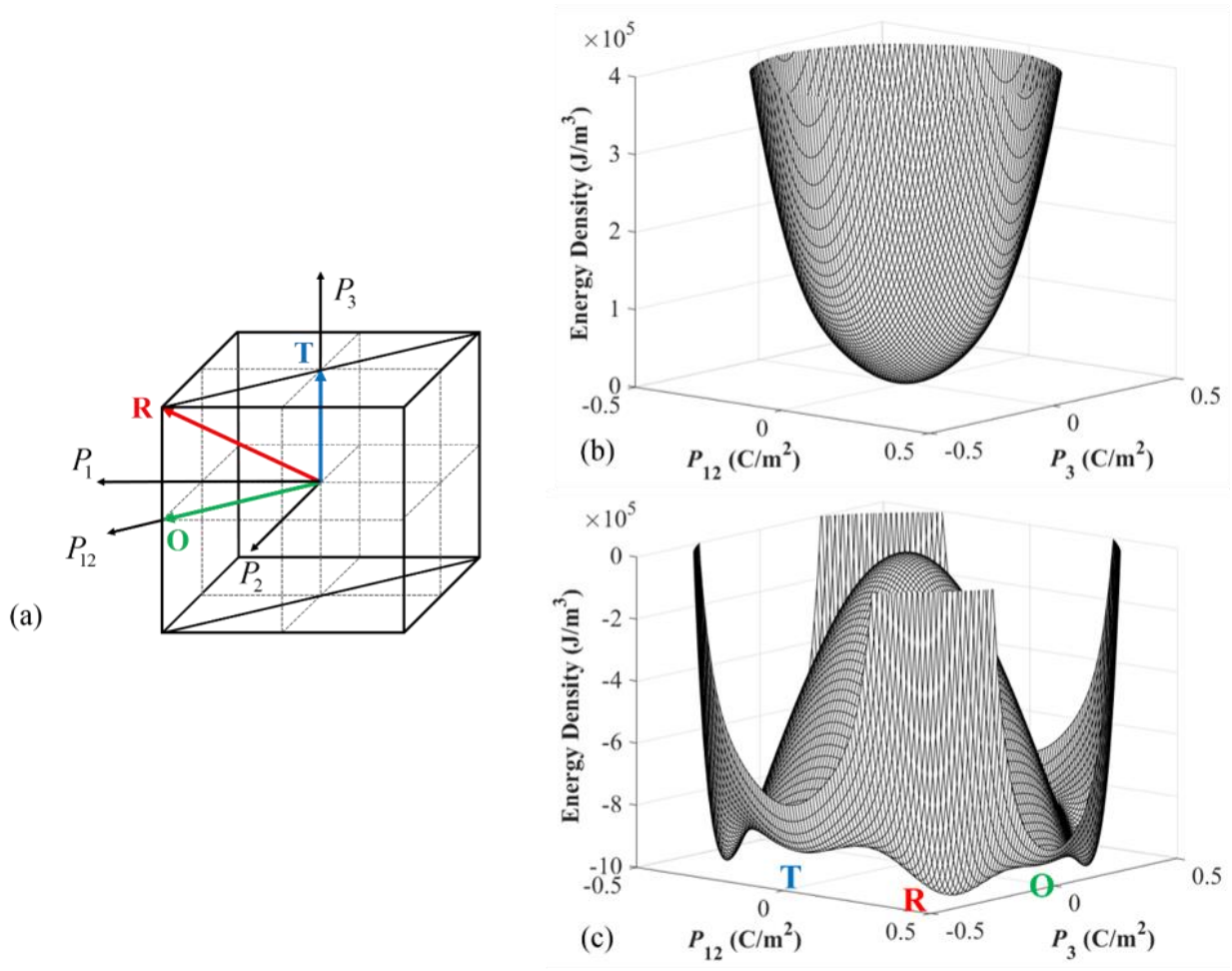

Figure 3.2. A schematic of a pseudo-cubic unit cell (a) and its energy density plotted as a function of P_{12} and P_3 above the Curie temperature (b) and at room temperature (c).

The energy levels of each ferroelectric phase are plotted as a function of temperature in Figure 3.3. The phase transition temperatures were obtained at the intersections of the curves. The paraelectric cubic phase was assumed to possess zero energy. The energy densities of all three ferroelectric phases exceeded zero when the temperature went above 192°C. This was identified

as the Curie temperature. In the inset, the orthorhombic phase and rhombohedral phase were seen to successively possess the lowest energy as the temperature was reduced below 118°C and 93°C. Note the Curie temperature T_C = 192°C and phase transition temperature T_{OT} = 118°C were taken from the measurements on 26PIN-42PMN-32PT [67] and used to determine the coefficients of the energy function. The resulting phase transition temperature T_{RO} = 93°C matched the results of the same experiment on 26PIN-42PMN-32PT [67].

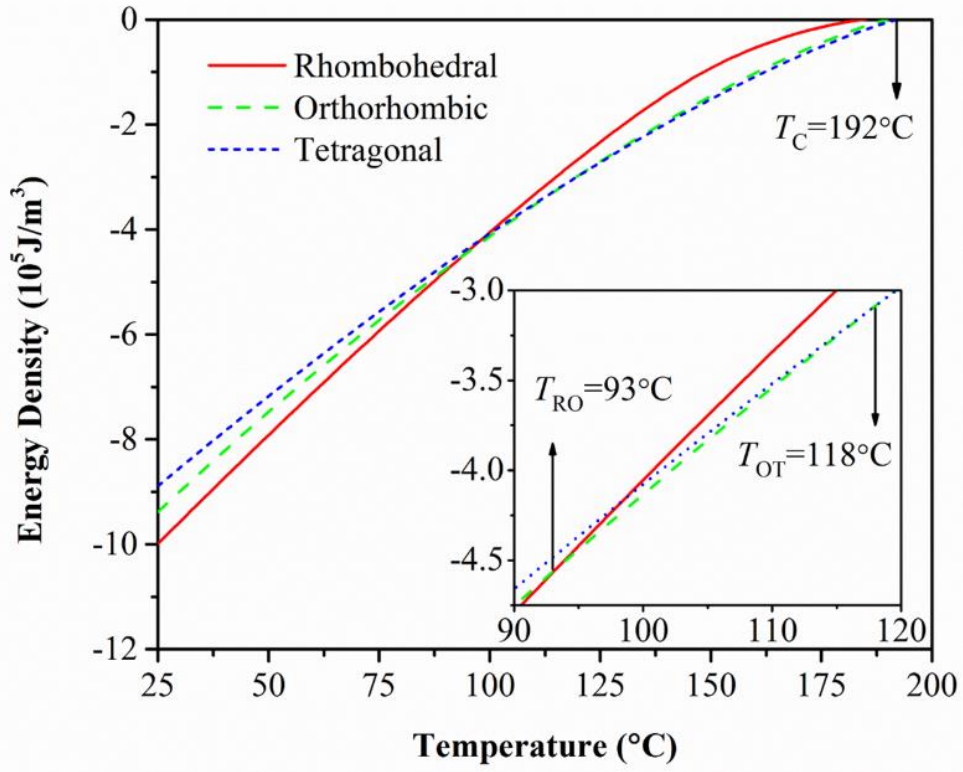

Figure 3.3. Energy density of three ferroelectric phases plotted as a function of temperature. The phase transition temperatures are obtained at the intersections of the curves.

The spontaneous polarization and dielectric constants are plotted as a function of temperature in Figure 3.4. The spontaneous polarization was obtained by minimizing the energy function at a given temperature. As shown in Figure 3.4(a), the magnitude of spontaneous polarization decreased as the temperature increased. Characteristics of first order phase transitions were

observed at the transition with polarization being discontinuous. In addition, the direction of spontaneous polarization changed from <001> to <110> and finally to <111> as the crystal underwent the phase transitions T → O → R. The dielectric constants were obtained by taking the second derivatives of the energy function, Eq. (3.3).

$$\frac{1}{e_{ij}^{\mathrm{A}} e_0} = \frac{\partial f_{\mathrm{LD}}^{\mathrm{A}}}{\partial P_i^{\mathrm{A}} \partial P_j^{\mathrm{A}}} \qquad (i, j = 1,2,3;\ \ \mathrm{A}:\mathrm{T},\ \mathrm{O}\ \mathrm{or}\ \mathrm{R}) \tag{3.3}$$

Since three different ferroelectric phases are involved, superscript A is used to denote the ferroelectric phase and all the quantities are expressed in the associated local coordinate systems. The dielectric constants of all three ferroelectric phases are plotted in Figure 3.4(b). For tetragonal phase and rhombohedral phase, the two transverse components e_{11} and e_{22} are equal. The orthorhombic phase has three independent components of dielectric constants. The sharp increase of the dielectric constants when approaching the Curie temperature is related to the abrupt reduction of the polarization.

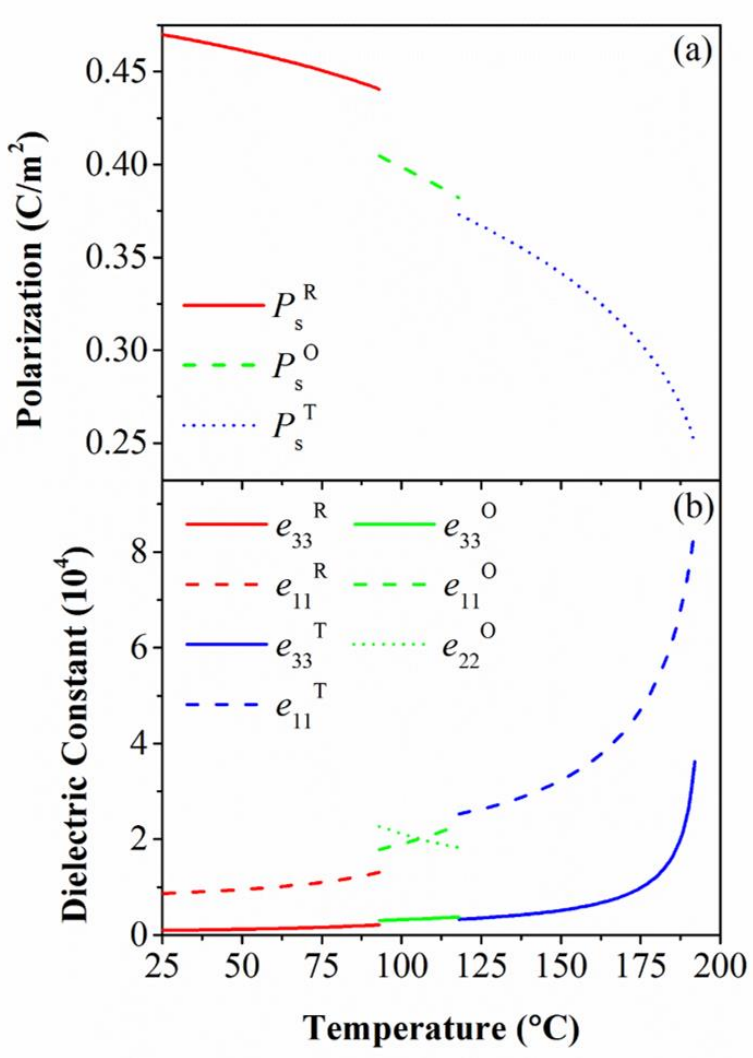

Figure 3.4. (a) Spontaneous polarization P_S plotted as a function of temperature. (b) Dielectric constants e_{ii} (i = 1, 2, 3) plotted as a function of temperature. Superscript T, O and R represent tetragonal, orthorhombic and rhombohedral phase, respectively. The subscript of the dielectric constants follows the definitions in Table 3.1.

3.4 Electric field driven homogeneous polarization switching

When an external electric field (E_1, E_2, E_3) is applied, the potential energy of the polarization in the electric field is added to the Landau-Devonshire energy, Eq. (3.4).

$$f\left(P_1,P_2,P_3\right)=f_{\mathrm{LD}}\left(P_1,P_2,P_3\right)-P_1E_1-P_2E_2-P_3E_3 \tag{3.4}$$

The electrical energy terms tilt the energy landscape, resulting in lower energy in the direction the electric field is applied. Under zero field, the energy landscape of the rhombohedral crystal possesses eight equivalent energy wells along the <111> directions. The barriers between any two energy wells prevent switching of the variants until a critical electric field is reached. Under the external electric field, the energy wells aligned with the field become deeper while those that are not favored by the field elevate. When the field exceeds a critical value, the elevated energy wells become unstable and the associated energy barriers become saddle points. This means the variants that are not favored by the field switch to other field-favored variants. In other words, the variant switching or homogeneous polarization switching takes place when the energy barrier between two variants is overcome under the external electric field. The height of the energy barrier governs the coercive field for homogeneous switching, i.e. switching not facilitated by domain wall motion. However, most of the previous work used the depth of energy wells for different variants or phases as the critical condition to trigger the polarization switching or phase transformation, without considering the energy barriers. As with the thermal case described above, this leads to anhysteretic behavior. Thermal fluctuations are capable of agitating the polarization past small energy barriers (out of shallow metastable wells). Applied field is required to move the polarization out of deeper wells. The effects of thermal fluctuations are not included in this work.

The polarization and strain response to a bipolar external electric field at room temperature were simulated for two domain engineered structures, [001] poled 4R and [110] poled 2R. A crystal variant based model [72,73] was adopted where each variant was tracked individually during the whole process and the overall response was the weighted sum of the contributions from all variants. The behavior of the [001] poled 4R crystals was determined by individually simulating each of the four variants and then taking the average. Similarly, the [110] poled 2R crystals were simulated by taking the average response of the two variants in the crystals. For a single variant, the associated polarization was obtained by finding the local minimum of the energy function, a condition defined by Eq. (3.5).

$$\frac{\partial f\left(P_1,P_2,P_3\right)}{\partial P_1}=0 \quad \frac{\partial f\left(P_1,P_2,P_3\right)}{\partial P_2}=0 \quad \frac{\partial f\left(P_1,P_2,P_3\right)}{\partial P_3}=0 \tag{3.5}$$

Under the stress free boundary condition, the strain response was modeled based on quadratic electrostriction. The spontaneous strain components are given by Eq. (3.6).

$$\begin{aligned} \varepsilon_{11}^0 &= Q_{11}P_1^2+Q_{12}P_2^2+Q_{12}P_3^2 & \varepsilon_{12}^0 &= Q_{44}P_1P_2 \\ \varepsilon_{22}^0 &= Q_{12}P_1^2+Q_{11}P_2^2+Q_{12}P_3^2 & \varepsilon_{13}^0 &= Q_{44}P_1P_3 \\ \varepsilon_{33}^0 &= Q_{12}P_1^2+Q_{12}P_2^2+Q_{11}P_3^2 & \varepsilon_{23}^0 &= Q_{44}P_2P_3 \end{aligned} \tag{3.6}$$

The electrostrictive coefficients Q_{11} = 0.066m^4/C^2, Q_{12} = -0.032m^4/C^2 and Q_{44} = 0.023m^4/C^2 were determined by fitting to the piezoelectric coefficients of domain engineered rhombohedral crystals at room temperature. The normal strain component along any direction with the unit vector [*l*, *m*, *n*] can be calculated by Eq. (3.7) [10].

$$\varepsilon_{[l,m,n]}=l^2\varepsilon_{11}^0+m^2\varepsilon_{22}^0+n^2\varepsilon_{33}^0+2lm\varepsilon_{12}^0+2ln\varepsilon_{13}^0+2mn\varepsilon_{23}^0 \tag{3.7}$$

The simulated polarization-electric field (*PE*) hysteresis loops for 4R and 2R are shown in Figure 3.5. In 4R (Figure 3.5(a)), as the cyclic electric field along the [001] direction exceeds the positive coercive field and overcomes the energy barriers, the four downward oriented variants become unstable and switch to the upward oriented variants. Then they switch back to downward oriented variants when the electric field reaches the negative coercive field and turns the energy barriers into saddle points. As shown in Figure 3.5(b), similar switching behavior between two leftward pointing variants and two rightward pointing variants is observed in 2R under the field along the [110] direction. Specifically for 2R, the polarization component perpendicular to the diagonal plane (1-10) is zero throughout the whole process. This indicates the polarization switching in 2R under the field along the [110] direction is an in-plane process.

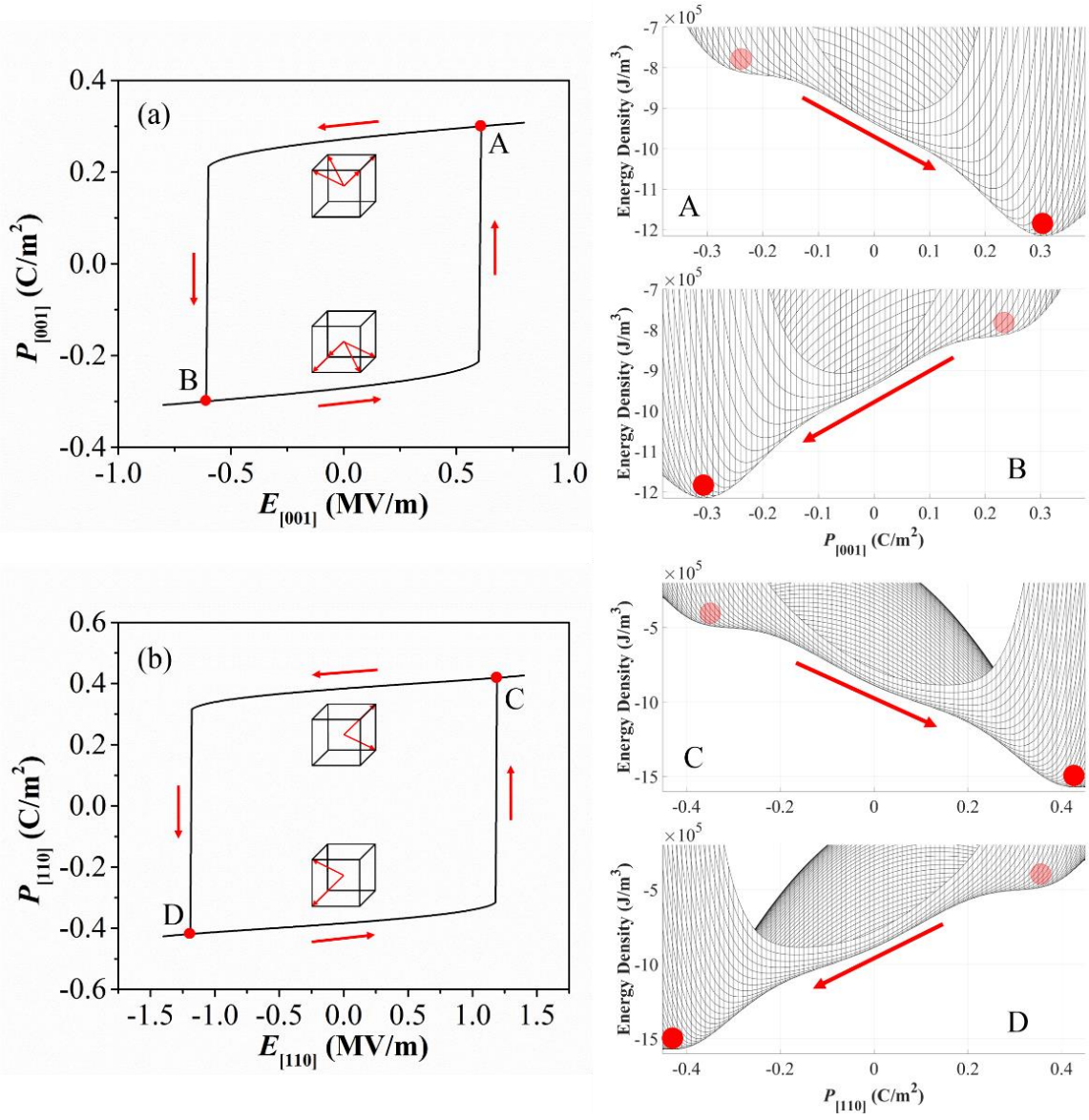

Figure 3.5. The simulated volume average polarization-electric field (*PE*) hysteresis loops for 4R (a) and 2R (b). The energy landscape labeled as A, B, C and D are corresponding to the points in the *PE* hysteresis loops.

The simulated strain-electric field (*SE*) hysteresis loops for 4R and 2R are shown in Figure 3.6. The volume average shear strain components are zero for both 4R and 2R. In 4R (Figure 3.6(a)), the two transverse strain components $\varepsilon_{[100]}$ and $\varepsilon_{[010]}$ are equal and opposite in sign from the longitudinal strain $\varepsilon_{[001]}$. The crystals elongate longitudinally and shrink transversely when the polarization and the electric field are in the same direction. In 2R (Figure 3.6(b)), there are

three independent normal strain components. The transverse strain component $\varepsilon_{[-110]}$ has the same sign as the longitudinal component $\varepsilon_{[110]}$ while the other transverse component $\varepsilon_{[001]}$ has the opposite sign.

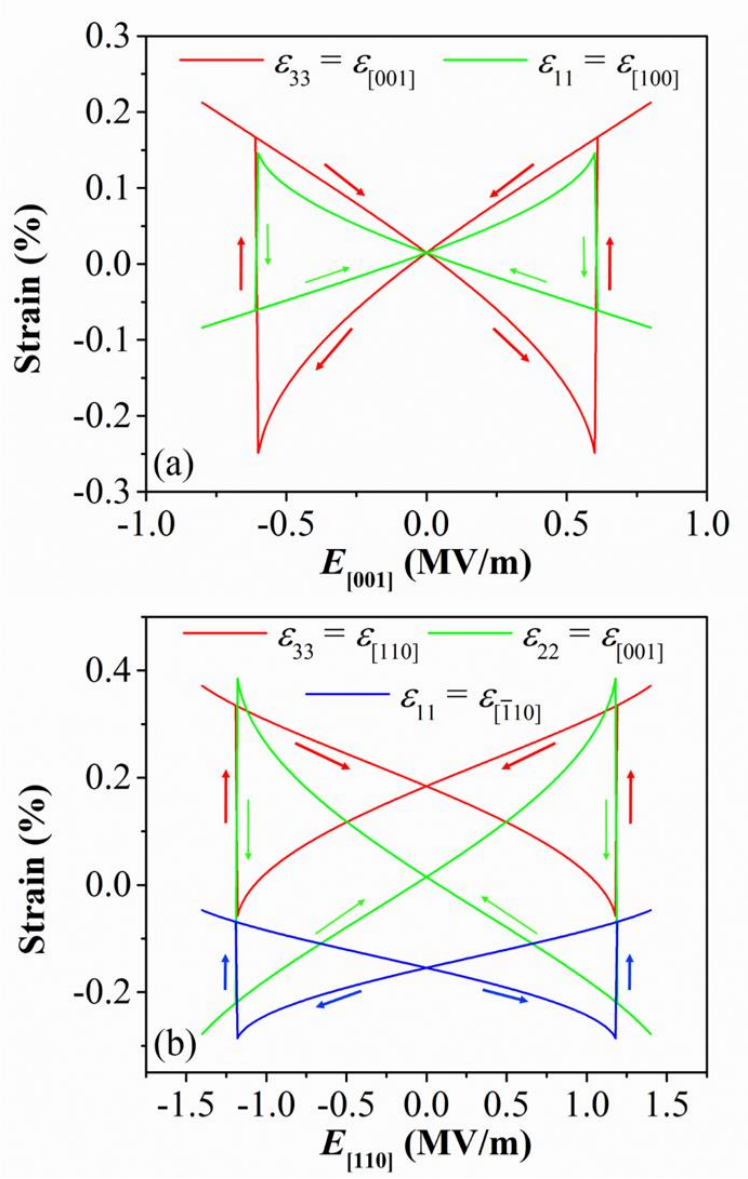

Figure 3.6. The simulated volume average strain-electric field (*SE*) hysteresis loops for 4R (a) and 2R (b).

With the homogeneous switching model (single polarization, no domains present) there is an abrupt jump of polarization and strain at the coercive field. Once the polarization has been

oriented, the dielectric constants and piezoelectric coefficients are apparent as the slope of the polarization and strain curves at zero field. They are defined by Eq. (3.8).

$$
\begin{aligned}
e_{33}^{4R} &= dP_{[001]} / dE_{[001]} & d_{33}^{4R} &= d\varepsilon_{[001]} / dE_{[001]} \\
e_{11}^{4R} &= dP_{[100]} / dE_{[001]} & d_{31}^{4R} &= d\varepsilon_{[100]} / dE_{[001]} \\
e_{33}^{2R} &= dP_{[110]} / dE_{[110]} & d_{33}^{2R} &= d\varepsilon_{[110]} / dE_{[110]} \\
e_{11}^{2R} &= dP_{[\bar{1}10]} / dE_{[110]} & d_{31}^{2R} &= d\varepsilon_{[\bar{1}10]} / dE_{[110]} \\
e_{22}^{2R} &= dP_{[001]} / dE_{[110]} & d_{32}^{2R} &= d\varepsilon_{[001]} / dE_{[110]}
\end{aligned}
\qquad (3.8)
$$

The obtained constants are listed in Table 3.4 along with the experimental data. These data are from compositions in the rhombohedral region of the phase diagram. Some of the compositions are away from the MPB, resulting in lower piezoelectric properties. The data obtained in this work match the experimental measurements well except the coercive field and e_{22} of 2R. The reasons could be the absence of domain wall effects in the homogeneous switching, the absence of thermal fluctuation effects, or the approximations made in the coefficient determination process due to the lack of experimental data.

The piezoelectric coefficients for the single domain orthorhombic phase (at 100°C) and tetragonal phase (at 120°C) were calculated using the electrostrictive coefficients determined for the rhombohedral phase. The tetragonal phase has d_{33} = 1429pm/V and d_{31} = -693pm/V while the orthorhombic phase has d_{33} = 638pm/V, d_{31} = 123pm/V and d_{32} = -716pm/V. No high temperature experimental data of the MPB composition are available for direct comparison. The compositions that are not at the MPB exhibit lower piezoelectricity at room temperature: the single domain tetragonal phase has d_{33} = 530pm/V and d_{31} = -200pm/V [68] while the single domain orthorhombic phase has d_{33} = 350pm/V, d_{31} = 153pm/V and d_{32} = -346pm/V [69]. In

order to have a more accurate description of the piezoelectricity for tetragonal phase and orthorhombic phase, a new set of electrostrictive coefficients may need to be determined.

Table 3.4. Dielectric constant, coercive field, remanent polarization and piezoelectric coefficient of 4R and 2R at room temperature. Dielectric constant and piezoelectric coefficient were calculated based on the slope of the *PE* and *SE* curves between 0 and 0.1MV/m, respectively.

Crystal properties		This work	Experimental data
4R	e_{33} (-)	5919	7244[a], 5900[d], 4753[h],4532[g], 4400[c]
	e_{11} (-)	6147	10081[a], 1728[h], 1666[g]
	E_C (MV/m)	0.60	0.6[g], 0.57[h], 0.56[c], 0.55[a], 0.43[d]
	P_r (C/m^2)	0.271	0.34[a], 0.267[h], 0.26[c], 0.258[g]
	d_{33} (pm/V)	2671	2742[a], >2000[d], 1500[c], 1338[g], 1285[h]
	d_{31} (pm/V)	-1331	-1337[a], -700[c], -651[g], -646[h]
	d_{15} (pm/V)	197	232[a], 147[g], 122[h]
2R	e_{33} (-)	3497	4574[e], 4361[b], 4360[f], 3613[h], 3400[c], 3384[g]
	e_{11} (-)	8729	7459[e], 6814[b], 6810[f], 5028[h], 5000[g]
	e_{22} (-)	6147	1596[e], 1483[b], 1480[f], 1273[h], 1201[g]
	E_C (MV/m)	1.18	0.66[g], 0.61[f], 0.55[b], 0.53[e], 0.53[c]
	P_r (C/m^2)	0.38	0.37[c], 0.37[g]
	d_{33} (pm/V)	1236	1363[b], 1300[f], 1068[e], 972[g], 925[c], 922[h]
	d_{31} (pm/V)	687	744[b], 730[f], 675[e], 590[c], 496[g], 488[h]
	d_{32} (pm/V)	-1911	-1781[b], -1693[e], -1680[f],-1420[c],-1268[g], -1196[h]
	d_{15} (pm/V)	2905	3354[b], 3122[e], 2900[f], 2373[h], 2288[g]
	d_{24} (pm/V)	279	200[f], 162[b], 142[e], 106[h], 94[g]

a: 27PIN-40PMN-33PT (Reference [74]); b: PIN-PMN-32PT (Reference [67]);
c: 28PIN-40PMN-32PT (Reference [75]); d: MPB (Reference [66]);
e: 24PIN-46PMN-30PT (Reference [76]); f: MPB (Reference [77]);
g: 33PIN-38PMN-29PT (Reference [78]); h: 24PIN-47PMN-29PT (Reference [79]).

3.5 Combined effect of temperature and electric field

The previous two sections addressed the thermal properties under zero field and *PE* and *SE* hysteresis loops at room temperature. In this section, simulations of the combined effect of temperature and electric field are presented. The hysteresis loops for 4R and 2R were simulated at 25°C, 50°C and 75°C. The results are shown in Figure 3.7. The trends observed in 4R and 2R are similar. As the temperature increases, the polarizations decrease while the dielectric constants and piezoelectric coefficients at small field increase. In addition, the *PE* hysteresis loops become slimmer with lower coercive field. This indicates the energy barrier becomes smaller and the critical electric field of driving the polarization switching is reduced. Direct quantitative validation of the results is not available due to the lack of experimental data. But the same trend was observed in the measurements on 26PIN-47PMN-27PT [80] and 24PIN-51PMN-25PT [81]. These two compositions are also in rhombohedral phase at room temperature but away from the MPB with lower piezoelectric properties. By comparing to the experimental results, the capability of the proposed energy function in capturing the combined effect of electric field and temperature was partially validated.

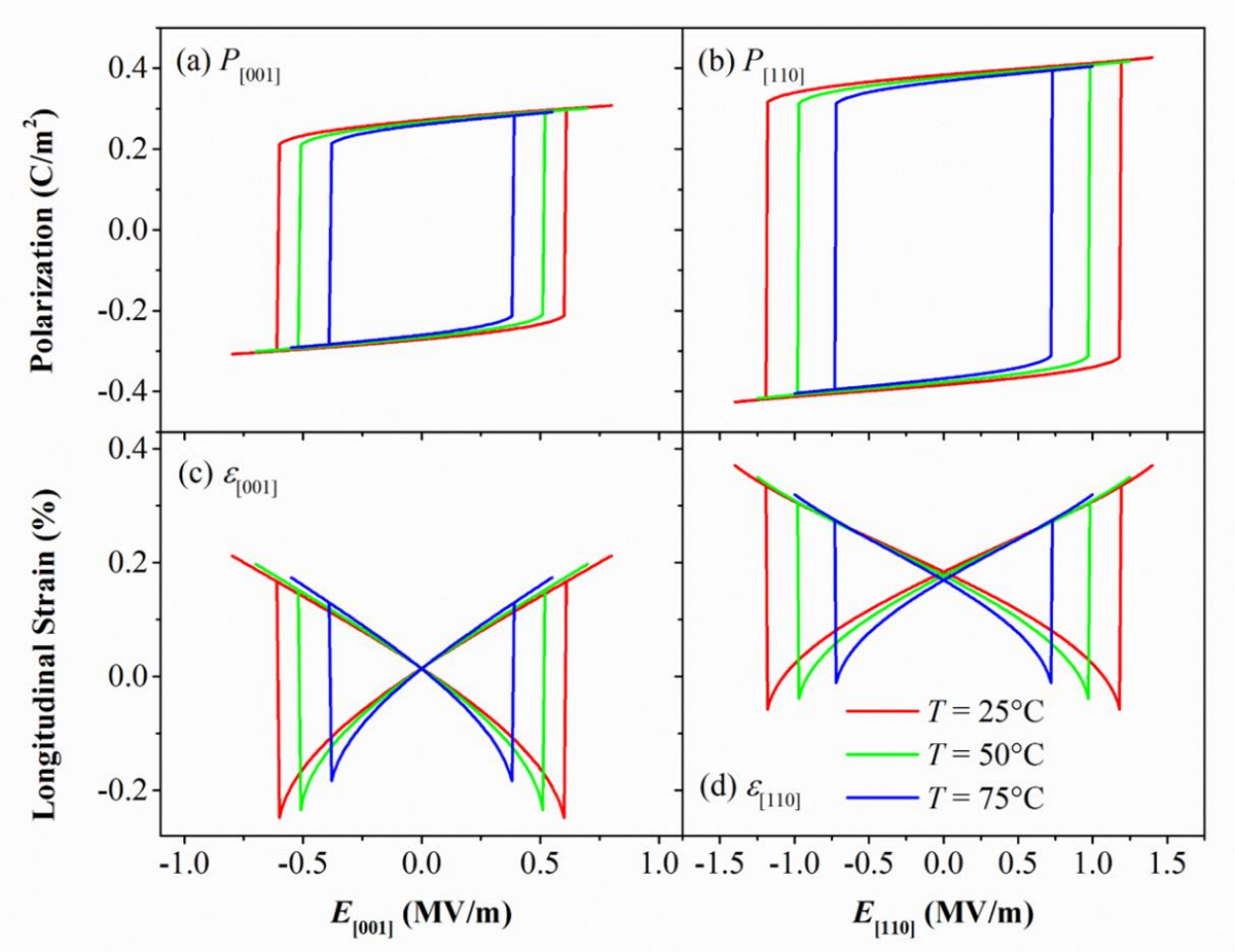

Figure 3.7. The hysteresis loops at 25°C, 50°C and 75°C. (a) The *PE* loops of 4R. (b) The *PE* loops of 2R. (c) The *SE* loops of 4R. (d) The *SE* loops of 2R.

3.6 Conclusion

Domain engineered rhombohedral ferroelectric single crystals of PIN-PMN-PT have stable domain structures that improve piezoelectric properties and reduce dielectric loss. Modeling the evolution of domain structures is challenging as multiple domain switching and phase transformations take place with temperature and applied electric field. A Landau-Devonshire energy function, in the form of a 10^{th} order polynomial, was calibrated through extensive fitting to the experimental data reported in the literature. The resulting energy function reproduced the dielectric, piezoelectric and ferroelectric properties of PIN-PMN-PT with a composition near the MPB. It also captured the effects of temperature and electric field on the homogeneous polarization switching in domain engineered 4R and 2R crystals. The energy barrier between variants was used to govern the coercive field, resulting in hysteresis loops of polarization and strain. The homogeneous polarization switching described by the energy function reproduced the behavior of domain engineered crystals where the domain structures were stable with minimal domain wall motion. To include domain wall effects, the energy function needs to be implemented in a phase-field model where the gradient energy is taken into account. The domain patterns and the effects of boundary conditions, geometry, etc. can also be addressed using the phase-field method. With the energy function proposed in this work, the Landau-Devonshire theory has been extended from the classic $BaTiO_3$ crystals with tetragonal symmetry to PIN-PMN-PT crystals with rhombohedral symmetry. This will enable the use of phase-field models to gain a deeper understanding of domain structures, domain energetics and the associated mechanisms of domain evolution in rhombohedral ferroelectric single crystals.

Appendix A Coefficient determination

The coefficients of the proposed energy function were determined by fitting to the data of polarization and dielectric constants of each ferroelectric phase in the single domain state as well as the temperatures of phase transformations. Since the three ferroelectric phases have different polar directions, local coordinate systems were used to describe the properties of each ferroelectric phase. These local coordinate systems were defined in Table 3.1 with x_3 direction aligned with the polar direction of each ferroelectric phase. For tetragonal phase, the local coordinate system was the same as the global pseudo-cubic coordinate system. However, for orthorhombic phase and rhombohedral phase, the energy function was expressed in the associated local coordinate systems through orthogonal transformations, indicated by Eq. (3.9).

$$\begin{aligned} f_{\mathrm{LD}}(P_1,P_2,P_3) &= f_{\mathrm{LD}}^{\mathrm{T}}(P_1,P_2,P_3) \\ f_{\mathrm{LD}}(P_1,P_2,P_3) &\rightarrow f_{\mathrm{LD}}^{\mathrm{O}}(P_1^{\mathrm{O}},P_2^{\mathrm{O}},P_3^{\mathrm{O}}) \\ f_{\mathrm{LD}}(P_1,P_2,P_3) &\rightarrow f_{\mathrm{LD}}^{\mathrm{R}}(P_1^{\mathrm{R}},P_2^{\mathrm{R}},P_3^{\mathrm{R}}) \end{aligned} \tag{3.9}$$

With α_{11111} and α_{11122} set to zero and α_1 solved by applying the Curie-Weiss law, the remaining 12 unknown coefficients were divided into three groups according to the symmetry. For tetragonal phase, by taking the P_3 as the polar direction of the single domain state and setting P_1 and P_2 to zero, the energy function only contained three unknown coefficients α_{11}, α_{111} and α_{1111}. These were determined by Eq. (3.10).

$$\begin{aligned}
\frac{\partial f_{\mathrm{LD}}^{\mathrm{T}}}{\partial P_3^{\mathrm{T}}}\left(0,0,P_S^{\mathrm{T}}\left(T_1\right)\right)&=0\\
\frac{1}{e_{33}^{\mathrm{T}}\left(T_1\right)e_0}&=\frac{\partial^2 f_{\mathrm{LD}}^{\mathrm{T}}}{\partial\left(P_3^{\mathrm{T}}\right)^2}\left(0,0,P_S^{\mathrm{T}}\left(T_1\right)\right)\\
f_{\mathrm{LD}}^{\mathrm{T}}\left(0,0,P_S^{\mathrm{T}}\left(T_C\right)\right)&=0\\
\frac{\partial f_{\mathrm{LD}}^{\mathrm{T}}}{\partial P_3^{\mathrm{T}}}\left(0,0,P_S^{\mathrm{T}}\left(T_C\right)\right)&=0
\end{aligned} \tag{3.10}$$

The first two equations in Eq. (3.10) were for the spontaneous polarization and longitudinal dielectric constant of tetragonal phase. The remaining two equations were used to describe the energy equivalence between tetragonal phase and cubic phase at the Curie temperature. The cubic phase was assumed to possess zero energy. Note the spontaneous polarization of tetragonal phase at the Curie temperature $P_{\mathrm{S}}^{\mathrm{T}}(T_{\mathrm{C}})$ was unknown. It was determined together with α_{11}, α_{111} and α_{1111}. Solving Eq. (3.10) and all the following equations required a numerical method as high order polynomials were involved. The Newton-Raphson method was used. With α_{11}, α_{111} and α_{1111} determined, the spontaneous polarization of tetragonal phase at the temperature of phase transition between tetragonal phase and orthorhombic phase $P_{\mathrm{S}}^{\mathrm{T}}(T_{\mathrm{OT}})$ was calculated using Eq. (3.11).

$$\frac{\partial f_{\mathrm{LD}}^{\mathrm{T}}}{\partial P_3^{\mathrm{T}}}\left(0,0,P_S^{\mathrm{T}}\left(T_{\mathrm{OT}}\right)\right)=0 \tag{3.11}$$

Next, orthorhombic symmetry was considered. In the local coordinate system associated with 1O configuration, by setting the two polarization components along the nonpolar directions to zero, the energy function only contained unknown coefficients α_{12}, α_{112}, α_{1112}, α_{1122} and α_{11112}. They were determined by solving Eq. (3.12).

$$
\begin{aligned}
\frac{1}{e_{11}^{\mathrm{T}}(T_1)e_0} &= \frac{\partial^2 f_{\mathrm{LD}}^{\mathrm{T}}}{\partial\left(P_1^{\mathrm{T}}\right)^2}\left(0,0,P_S^{\mathrm{T}}(T_1)\right)\\
\frac{\partial f_{\mathrm{LD}}^{\mathrm{O}}}{\partial P_3^{\mathrm{O}}}\left(0,0,P_S^{\mathrm{O}}(T_2)\right) &= 0\\
\frac{1}{e_{33}^{\mathrm{O}}(T_2)e_0} &= \frac{\partial^2 f_{\mathrm{LD}}^{\mathrm{O}}}{\partial\left(P_3^{\mathrm{O}}\right)^2}\left(0,0,P_S^{\mathrm{O}}(T_2)\right)\\
\frac{1}{e_{11}^{\mathrm{O}}(T_2)e_0} &= \frac{\partial^2 f_{\mathrm{LD}}^{\mathrm{O}}}{\partial\left(P_1^{\mathrm{O}}\right)^2}\left(0,0,P_S^{\mathrm{O}}(T_2)\right)\\
f_{\mathrm{LD}}^{\mathrm{O}}\left(0,0,P_S^{\mathrm{O}}(T_{\mathrm{OT}})\right) &= f_{\mathrm{LD}}^{\mathrm{T}}\left(0,0,P_S^{\mathrm{T}}(T_{\mathrm{OT}})\right)\\
\frac{\partial f_{\mathrm{LD}}^{\mathrm{O}}}{\partial P_3^{\mathrm{O}}}\left(0,0,P_S^{\mathrm{O}}(T_{\mathrm{OT}})\right) &= 0
\end{aligned}
\tag{3.12}
$$

The first equation in Eq. (3.12) was for the transverse dielectric constant of tetragonal phase. The second to fourth equations were for the spontaneous polarization and dielectric constants of orthorhombic phase. The remaining two equations were used to describe the energy equivalence between tetragonal phase and orthorhombic phase at the phase transition temperature T_{OT}. Since $P_{\mathrm{S}}^{\mathrm{T}}(T_{\mathrm{OT}})$ was already solved in Eq. (3.11), the RHS of the fifth equation in Eq. (3.12) was known.

With the above-mentioned coefficients determined, the last few coefficients α_{123}, α_{1123}, α_{11223} and α_{11123} were determined by solving Eq. (3.13).

$$
\begin{aligned}
\frac{1}{e_{22}^{\mathrm{O}}(T_2)e_0} &= \frac{\partial^2 f_{\mathrm{LD}}^{\mathrm{O}}}{\partial\left(P_2^{\mathrm{O}}\right)^2}\left(0,0,P_S^{\mathrm{O}}(T_2)\right)\\
\frac{\partial f_{\mathrm{LD}}^{\mathrm{R}}}{\partial P_3^{\mathrm{R}}}\left(0,0,P_S^{\mathrm{R}}(T_3)\right) &= 0\\
\frac{1}{e_{33}^{\mathrm{R}}(T_3)e_0} &= \frac{\partial^2 f_{\mathrm{LD}}^{\mathrm{R}}}{\partial\left(P_3^{\mathrm{R}}\right)^2}\left(0,0,P_S^{\mathrm{R}}(T_3)\right)\\
\frac{1}{e_{11}^{\mathrm{R}}(T_3)e_0} &= \frac{\partial^2 f_{\mathrm{LD}}^{\mathrm{R}}}{\partial\left(P_1^{\mathrm{R}}\right)^2}\left(0,0,P_S^{\mathrm{R}}(T_3)\right)
\end{aligned}
\tag{3.13}
$$

The first equation in Eq. (3.13) was for the other transverse dielectric constant of orthorhombic phase. The remaining equations in Eq. (3.13) were used to fit to the spontaneous polarization and dielectric constants of rhombohedral phase.

4 Phase-field simulation of domain walls in ferroelectric single crystals

4.1 Introduction

Ferroelectric relaxor single crystals PMN-PT exhibit ultrahigh piezoelectric coefficients and electromechanical coupling factors and thus are widely used as a substitute for conventional piezoelectric ceramics to improve the performance of sensors and actuators. The ternary compound PIN-PMN-PT [5] was developed to increase the phase transition temperature and Curie temperature of PMN-32PT without sacrificing the exceptional piezoelectric properties. These ferroelectric relaxor-PT crystals are usually grown in compositional ranges close to a morphotropic phase boundary (MPB) that results in rhombohedral symmetry. Then they are cut and poled along certain orientations to achieve enhanced piezoelectric properties, a process described as domain engineering [2,62,63].

The engineered domain structures are very important in understanding the material behavior and the mechanism of domain evolution under external excitations. The phase-field method is a powerful approach to modeling mesoscale microstructural evolution governed by the time-dependent Ginzburg-Landau (TDGL) equation. Chen et al. developed a semi-implicit Fourier-spectral method [41] to solve the TDGL equation and applied it to the phase-field modeling of ferroelectric domain formation in three-dimensional space [60] and domain structures in ferroelectric thin films [82–85]. Using the same computational method, Wang et al. simulated ferroelectric and ferroelastic polarization switching [86] and studied the effect of mechanical strain [87] and defects (cracks and notches) [88–90]. Zhang and Bhattacharya modeled domain switching subjected to mechanical stress and cyclic electric field using a finite difference

framework and attributed the large strain actuation to 90° domain switching [42]. A finite element implementation of a phase-field model was established by Schrade et al. [43] and Landis et al. [36]. In addition to single crystals, the phase-field method was extended to polycrystals to look into the effect of grains [91–93]. Recently, the phase-field method was used to investigate the flexoelectric effect on the domain structures in nanoscale ferroelectrics [94–96].

Even though the phase-field method has proved to be a powerful approach to understanding the mechanism of microstructural evolution, most of the modeling work was focused on the materials with a tetragonal structure such as $BaTiO_3$, $PbTiO_3$ and certain compositions of PZT with high PT content. This is because the phase-field method requires input of a Landau-Devonshire energy function that describes the dielectric, piezoelectric and ferroelectric properties of a single crystal in the single domain state, but this type of energy function was not available for the new ferroelectric relaxor-PT crystals. Recently Lv and Lynch developed a 10^{th} order Landau-Devonshire energy function for rhombohedral PIN-PMN-PT crystals [10,97]. This was elaborated in Chapter 3. This energy function was implemented in a phase-field model in the work presented here. The results showed the effects of domain formation and evolution on the material properties. Special attention was given to the two types of domain walls that were observed in the rhombohedral crystals, the 71 domain wall and the 109 domain wall. The next section reviews the phase-field formulation and finite element implementation. This is followed by the simulations of 71 domain walls and 109 domain walls resulting in homogeneous and heterogeneous responses, respectively. Then the minimal domain wall motion in the engineered domain structures under the electric field is discussed based on the simulation results.

4.2 Phase-field method

The phase-field method uses a free energy density functional with order parameters that describe dielectric, piezoelectric, ferroelectric and elastic properties. Polarization and strain are usually chosen as the order parameters for ferroelectric materials. The total free energy density of the system includes the Landau-Devonshire energy, gradient energy, elastic energy and electrical energy, Eq. (4.1).

$$f = f_{\text{L-D}} + f_{\text{grad}} + f_{\text{elas}} + f_{\text{elec}} \tag{4.1}$$

Here the Landau-Devonshire energy is expressed as a 10^{th} order polynomial that was developed for PIN-PMN-PT crystals with rhombohedral variants [10,97]. This energy function was originally expressed in terms of three polarization components P_1, P_2 and P_3 along the axes of the pseudo-cubic unit cell as shown in Figure 4.1(a). The associated coordinate system is called the "cubic" coordinate system. Since the polarization component perpendicular to the diagonal plane (-110) remains zero throughout the switching process under the electric field along the [110] direction [10], the whole system can be reduced to two dimensions by using two in-plane components p_y and p_z as defined in Figure 4.1(b). The associated coordinate system is referred to as the "rhombohedral" coordinate system. The plane (-110) contains four spontaneous polarization directions corresponding to the energy minima of the Landau-Devonshire energy. Each of them is called a rhombohedral variant. By poling along the [110] direction with electric field, an engineered domain structure is obtained with only two variants, R1-R2 or R3-R4. This is called a two-rhombohedral-variant (2R) crystal.

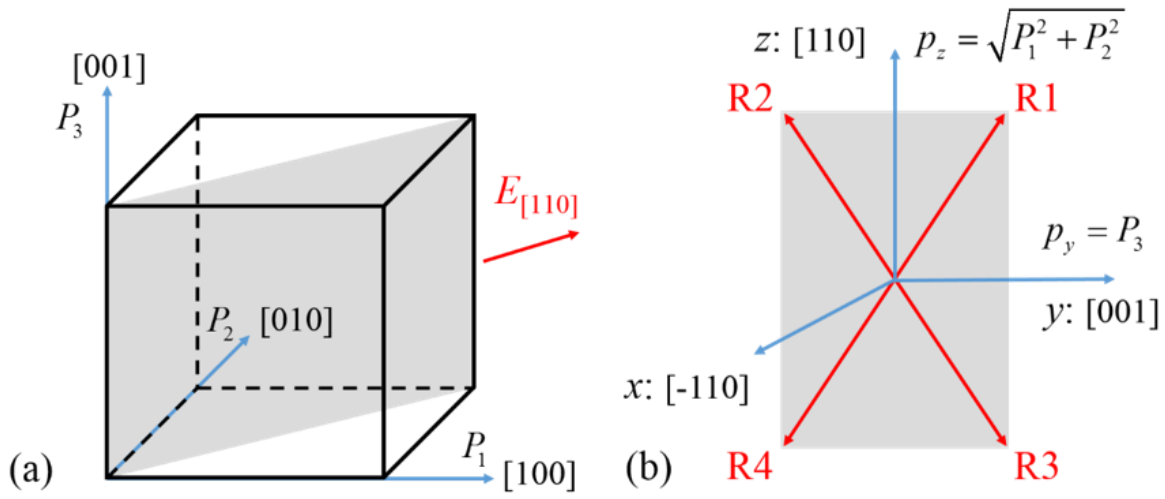

Figure 4.1. (a) The "cubic" coordinate system used in reference [10]. The three axes are in the directions [100]-[010]-[001]. (b) The 2D "rhombohedral" coordinate system used in this work. The three axes are in the directions [-110]-[001]-[110]. The *y*-*z* plane is the diagonal plane (-110) in (a). It contains four rhombohedral variants, R1, R2, R3 and R4.

In this work, the engineered 2R domain structure is modeled in the 2D rhombohedral coordinate system. All of the energy terms are expressed in this 2D system. Detailed derivations of the energies can be found in Chapter 2 and the work of Su and Landis [36]. The 10th order Landau-Devonshire energy function with coefficients expressed in the rhombohedral coordinate system is given by Eq. (4.2).

$$\begin{aligned} f_{\text{L-D}} = {} & \alpha_1\left(p_y^2 + p_z^2\right) + \frac{1}{2}\alpha_{11}\left(2p_y^4 + p_z^4\right) + \frac{1}{4}\alpha_{12}\left(4p_y^2p_z^2 + p_z^4\right) + \frac{1}{4}\alpha_{111}\left(4p_y^6 + p_z^6\right) \\ & + \frac{1}{4}\alpha_{112}\left(4p_y^4p_z^2 + p_z^6 + 2p_y^2p_z^4\right) + \frac{1}{4}\alpha_{123}p_y^2p_z^4 + \frac{1}{8}\alpha_{1111}\left(8p_y^8 + p_z^8\right) \\ & + \frac{1}{8}\alpha_{1112}\left(2p_y^2p_z^6 + p_z^8 + 8p_y^6p_z^2\right) + \frac{1}{16}\alpha_{1122}\left(8p_y^4p_z^4 + p_z^8\right) \\ & + \frac{1}{4}\alpha_{1123}\left(p_y^4p_z^4 + p_y^2p_z^6\right) + \frac{1}{16}\alpha_{11112}\left(2p_y^2p_z^8 + p_z^{10} + 16p_y^8p_z^2\right) \\ & + \frac{1}{16}\alpha_{11223}\left(4p_y^4p_z^6 + p_y^2p_z^8\right) + \frac{1}{8}\alpha_{11123}\left(2p_y^6p_z^4 + p_y^2p_z^8\right) \end{aligned} \tag{4.2}$$

All of the coefficients are taken from reference [10] and temperature is set to 25°C for α_1.

The gradient energy is expressed in terms of polarization gradient, which penalizes large spatial variations of polarization, Eq. (4.3).

$$f_{\text{grad}} = \frac{1}{2} G\left(p_{y,y}^2 + p_{z,z}^2 + p_{y,z}^2 + p_{z,y}^2 \right) \tag{4.3}$$

The comma after the variable represents the derivative with respect to the spatial coordinate. Here the gradient coefficient G is the only parameter, making the gradient energy independent of crystallographic orientation. The gradient energy has a direct effect on the domain wall thickness, which is proportional to the square root of G [36].

The elastic energy is expressed in terms of elastic strain components, Eq. (4.4).

$$f_{\text{elas}} = \frac{1}{2} C_{ijkl} \varepsilon_{ij}^{\text{el}} \varepsilon_{kl}^{\text{el}} \tag{4.4}$$

Repeated indices imply summation (Einstein summation convention). The superscript "el" is used to represent the elastic strain tensor, which is the difference between total strain and spontaneous strain: $\varepsilon_{ij}^{\text{el}} = \varepsilon_{ij} - \varepsilon_{ij}^{0}$. Here the elastic stiffness tensor C_{ijkl} has the same symmetry as the high temperature cubic phase. The three independent components are $C_{11} = 12\times10^{10}\text{N/m}^2$, $C_{12} = 10\times10^{10}\text{N/m}^2$ and $C_{44} = 6\times10^{10}\text{N/m}^2$. These values are estimated based on the measurements [74,98]. Note the elastic stiffness tensor C_{ijkl} is defined in the cubic coordinate system. Tensor transformation is required before it can be used to describe the elastic energy in the rhombohedral coordinate system, Eq. (4.5).

$$f_{\text{elas}} = \frac{1}{2} C'_{22} \left(\varepsilon_{yy}^{\text{el}} \right)^2 + \frac{1}{2} C'_{33} \left(\varepsilon_{zz}^{\text{el}} \right)^2 + C'_{23} \varepsilon_{yy}^{\text{el}} \varepsilon_{zz}^{\text{el}} + 2C'_{44} \left(\varepsilon_{yz}^{\text{el}} \right)^2 \tag{4.5}$$

Here C'_{ijkl} is the elastic stiffness tensor in the rhombohedral coordinate system. The subscripts 1-2-3 represent the orthogonal directions [-110]-[001]-[110], corresponding to *x*-*y*-*z* axes of the rhombohedral coordinate system. The subscripts 4-5-6 represent the shear terms *yz*-*zx*-*xy*. Eq. (4.5) is the elastic energy expansion by assuming generalized plane strain such that all elastic strain components are zero except ε_{yy}^{el}, ε_{zz}^{el} and ε_{yz}^{el}. Note that the total out-of-plane strain ε_{xx} is not zero. It is assumed to be equal to the out-of-plane component of the spontaneous strain ε_{xx}^{0}. The nonzero elastic strain components can be calculated by the displacement components u_y and u_z along *y* and *z* axes in Figure 4.1(b), Eq. (4.6).

$$\begin{aligned}
&\varepsilon_{yy}^{el} = u_{y,y} - \varepsilon_{yy}^{0} && \varepsilon_{yy}^{0} = \left(Q_{13}p_z^2 + Q_{33}p_y^2\right) \\
&\varepsilon_{zz}^{el} = u_{z,z} - \varepsilon_{zz}^{0} && \varepsilon_{zz}^{0} = \frac{1}{2}\left(Q_{13}+Q_{33}+Q_{44}\right)p_z^2 + Q_{13}p_y^2 \\
&\varepsilon_{yz}^{el} = \frac{1}{2}\left(u_{y,z}+u_{z,y}\right) - \varepsilon_{yz}^{0} && \varepsilon_{yz}^{0} = Q_{44}p_y p_z
\end{aligned} \tag{4.6}$$

The spontaneous strain components ε_{yy}^{0}, ε_{zz}^{0} and ε_{yz}^{0} within (-110) plane in the 2D rhombohedral coordinate system are obtained via tensor transformation of the spontaneous strain components defined in the cubic coordinate system, Eq. (4.7).

$$\begin{aligned}
&\varepsilon_{11}^{0} = Q_{33}P_1^2 + Q_{13}P_2^2 + Q_{13}P_3^2 && \varepsilon_{23}^{0} = Q_{44}P_2P_3 \\
&\varepsilon_{22}^{0} = Q_{13}P_1^2 + Q_{33}P_2^2 + Q_{13}P_3^2 && \varepsilon_{13}^{0} = Q_{44}P_1P_3 \\
&\varepsilon_{33}^{0} = Q_{13}P_1^2 + Q_{13}P_2^2 + Q_{33}P_3^2 && \varepsilon_{12}^{0} = Q_{44}P_1P_2
\end{aligned} \tag{4.7}$$

The spontaneous strain components in Eq. (4.7) are defined using the quadratic electrostrictive coefficients in the cubic coordinate system. The electrostrictive coefficients $Q_{33} = 0.066 m^4/C^2$, $Q_{13} = -0.032 m^4/C^2$ and $Q_{44} = 0.023 m^4/C^2$ are from reference [10].

The electrical energy has two contributions, one from the material, and the other from the free space occupied by the material, Eq. (4.8).

$$f_{\text{elec}} = -E_y p_y - E_z p_z - \frac{1}{2}\kappa_0 \left(E_y^2 + E_z^2\right) \tag{4.8}$$

Here κ_0 is the permittivity of free space. The electric field components E_y and E_z are along y and z axes, respectively. They are related to the electric potential (ϕ) by Eq. (4.9).

$$\begin{aligned} E_y &= -\phi_{,y} \\ E_z &= -\phi_{,z} \end{aligned} \tag{4.9}$$

The stress and electric displacement are obtained from the partial derivatives of the total free energy f using Eq. (4.10).

$$\begin{aligned} \sigma_{ij} &= \frac{\partial f}{\partial \varepsilon_{ij}} \\ D_i &= -\frac{\partial f}{\partial E_i} \end{aligned} \tag{4.10}$$

The temporal evolution of the polarization is governed by the TDGL equations. In the 2D system, they are expressed as

$$\begin{aligned} \beta \dot{p}_y &= \left(\frac{\partial f}{\partial p_{y,y}}\right)_{,y} + \left(\frac{\partial f}{\partial p_{y,z}}\right)_{,z} - \frac{\partial f}{\partial p_y} \\ \beta \dot{p}_z &= \left(\frac{\partial f}{\partial p_{z,y}}\right)_{,y} + \left(\frac{\partial f}{\partial p_{z,z}}\right)_{,z} - \frac{\partial f}{\partial p_z} \end{aligned} \tag{4.11}$$

where β is the inverse mobility coefficient. The dot on top of the variable represents the derivative with respect to time. The terms on the RHS of Eq. (4.11) represent the driving force for the evolution of the system.

The governing equations for mechanical equilibrium and Gauss law are in Eq. (4.12).

$$\begin{aligned} \sigma_{ij,j} &= 0 \\ D_{i,i} &= 0 \end{aligned} \tag{4.12}$$

The TDGL equation, mechanical equilibrium and Gauss law are solved simultaneously to make the phase-field model fully coupled. It is assumed that the system reaches mechanical equilibrium instantaneously for a given polarization field but varies slowly with respect to the speed of light (quasi-static electromagnetic approximation). The inertial terms and body forces are neglected. There is no volume charge density within the body. The boundary conditions for mechanical equilibrium and Gauss law are prescribed displacement / traction and prescribed electric potential / charge density, respectively.

The three governing equations (TDGL, mechanical equilibrium and Gauss law) are solved simultaneously using the finite element method. A mapped mesh is used with quadrilateral elements and quadratic Lagrange shape functions. Each node has five degrees of freedom: two polarization components (p_y and p_z), one electric potential (ϕ) and two displacement components (u_y and u_z). In order to improve the convergence, the variables and coefficients are normalized as follows,

$$
\begin{array}{lll}
\mathbf{P}^* = \mathbf{P} / P_0 & l_0 = \sqrt{G_0 / \alpha_0} & \mathbf{r}^* = \mathbf{r} / l_0 \\
\alpha_0 = \left|\alpha_1\right|_{25^\circ \mathrm{C}} & t_0 = \beta / \alpha_0 & t^* = t / t_0 \\
G^* = G / G_0 & \kappa_0^* = \kappa_0 \alpha_0 & \mathbf{C}^* = \mathbf{C} / \left(\alpha_0 P_0^2\right) \\
\mathbf{E}^* = \mathbf{E} / \left(\alpha_0 P_0\right) & \boldsymbol{\sigma}^* = \boldsymbol{\sigma} / \left(\alpha_0 P_0^2\right) & \mathbf{Q}^* = \mathbf{Q} \cdot P_0^2 \\
\alpha_1^* = \alpha_1 / \alpha_0 & \alpha_{11}^* = \alpha_{11} P_0^2 / \alpha_0 & \alpha_{12}^* = \alpha_{12} P_0^2 / \alpha_0 \\
\alpha_{111}^* = \alpha_{111} P_0^4 / \alpha_0 & \alpha_{112}^* = \alpha_{112} P_0^4 / \alpha_0 & \alpha_{123}^* = \alpha_{123} P_0^4 / \alpha_0 \\
\alpha_{1111}^* = \alpha_{1111} P_0^6 / \alpha_0 & \alpha_{1112}^* = \alpha_{1112} P_0^6 / \alpha_0 & \alpha_{1122}^* = \alpha_{1122} P_0^6 / \alpha_0 \\
\alpha_{1123}^* = \alpha_{1123} P_0^6 / \alpha_0 & \alpha_{11112}^* = \alpha_{11112} P_0^8 / \alpha_0 & \alpha_{11223}^* = \alpha_{11223} P_0^8 / \alpha_0 \\
\alpha_{11123}^* = \alpha_{11123} P_0^8 / \alpha_0 & &
\end{array}
\tag{4.13}
$$

where **r** is the spatial coordinate. The constants for normalization are $P_0 = 0.384\mathrm{C/m^2}$ and $G_0 = 5.99\times10^{-12}\mathrm{m^4NC^{-2}}$. The characteristic length scale is $l_0 = 1\mathrm{nm}$. All the variables and coefficients with a star represent the normalized quantities.

4.3 Domain wall formation

The phase-field method was first used to simulate the domain formation process on a representative volume element with the size of $200\times200\text{nm}^2$. The mesh size was $1\times1\text{nm}^2$ to ensure there were multiple mesh elements across a domain wall. The representative volume element works with periodic boundary conditions. It is straight-forward to apply periodic boundary conditions to the polarization and electric potential, i.e. the polarization and electric potential on one boundary are equal to those on the opposite boundary. However, applying periodic boundary conditions in the same manner to the displacements imposes a zero strain condition. A mechanical clamping effect is introduced. Most of the phase-field work in the past used the zero strain condition, but the free standing material behavior under external excitation is also of interest. In this work, a periodic boundary condition that accommodates nonzero strain was used based on a method developed for heterogeneous material systems [99,100]. Figure 4.2 is a schematic of a representative volume element with quadrilateral geometry. The node sets on the four edges except the vertex points are denoted as Top, Bot, Left and Right. LT, RT, LB and RB represent four vertex nodes, respectively. The periodic boundary conditions can be applied to the two displacement components (u and v) in the following manner:

$$\begin{cases} u_{\text{Bot}} - u_{\text{LB}} = u_{\text{Top}} - u_{\text{LT}} \\ v_{\text{Bot}} - v_{\text{LB}} = v_{\text{Top}} - v_{\text{LT}} \end{cases}$$
$$\begin{cases} u_{\text{Left}} - u_{\text{LB}} = u_{\text{Right}} - u_{\text{RB}} \\ v_{\text{Left}} - v_{\text{LB}} = v_{\text{Right}} - v_{\text{RB}} \end{cases} \tag{4.14}$$
$$\begin{cases} u_{\text{RB}} - u_{\text{LB}} = u_{\text{RT}} - u_{\text{LT}} \\ v_{\text{RB}} - v_{\text{LB}} = v_{\text{RT}} - v_{\text{LT}} \end{cases}$$

The first two groups of equations in Eq. (4.14) ensure periodicity in the vertical and horizontal directions, respectively. The last group of equations defines the relations of four vertex points,

which are not included in the first two groups. These periodic boundary conditions not only enforce periodicity in displacements, but also accommodate dilation or contraction with nonzero strain. To suppress rigid body motion, the vertex LB is fixed and the vertical displacement of vertex RB is constrained.

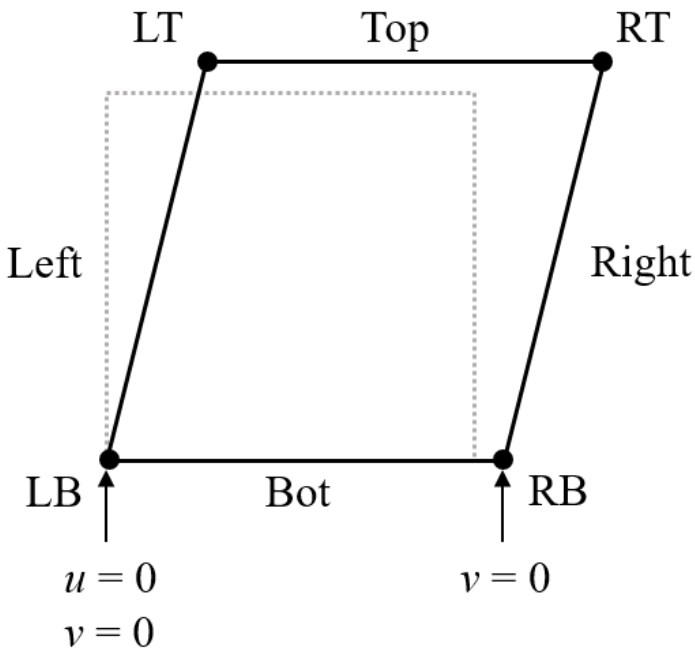

Figure 4.2. A schematic of a representative volume element with boundaries (Top, Bot, Left and Right) and vertex points (LT, RT, LB and RB). *u* and *v* are horizontal and vertical displacement components, respectively.

Driven by energy minimization to reach equilibrium state, the domain formation process in a representative volume element of the rhombohedral ferroelectric single crystal is shown in Figure 4.3. The colors represent the magnitude of polarization with unit C/m^2. The white arrows represent the directions of polarization. To initiate the process, random perturbations were applied to the initial values of polarizations. Triggered by the perturbation (Figure 4.3(a)), some domains began to nucleate and grow (Figure 4.3(b)). As the domains got larger, they began to interact with other domains nearby. Domains with the same polarization merged and formed

larger domains while those with different polarizations were separated by domain walls (Figure 4.3(c)). The 71, 109 and 180 domain walls all appeared, but soon the 180 domain walls became disfavored and began to fade out (Figure 4.3(d)). The intermediate process was mainly dominated by the 71 and 109 domain walls (Figure 4.3(e), (f) and (g)). The domain walls were 3~4nm thick given the normalized gradient coefficient $G^* = 4$. As the domains continued to evolve, 71 domain walls gradually disappeared. Eventually, two 109 domain walls survived in the equilibrium state (Figure 4.3(h)). As shown in Figure 4.3, the average strain was not zero throughout the domain formation process. The periodic boundary conditions in Eq. (4.14) accommodated the volume variation and avoided the clamping issue that could be introduced by equating the displacements on the opposite boundaries.

Note Figure 4.3(h) represents the ideal minimum energy state. In the actual material, defects exist that can pin the domain walls, generating more complex domain patterns similar to the intermediate states such as those in Figure 4.3(e), (f) or (g), where both 71 and 109 domain walls are populated and thus have a major effect on the material behavior. In order to gain deeper insight into the characteristics of the 71 and 109 domain walls and their effects on the properties of domain engineered 2R crystals, the evolution of the two domain walls under the electric field along the [110] direction was simulated and discussed in the next section.

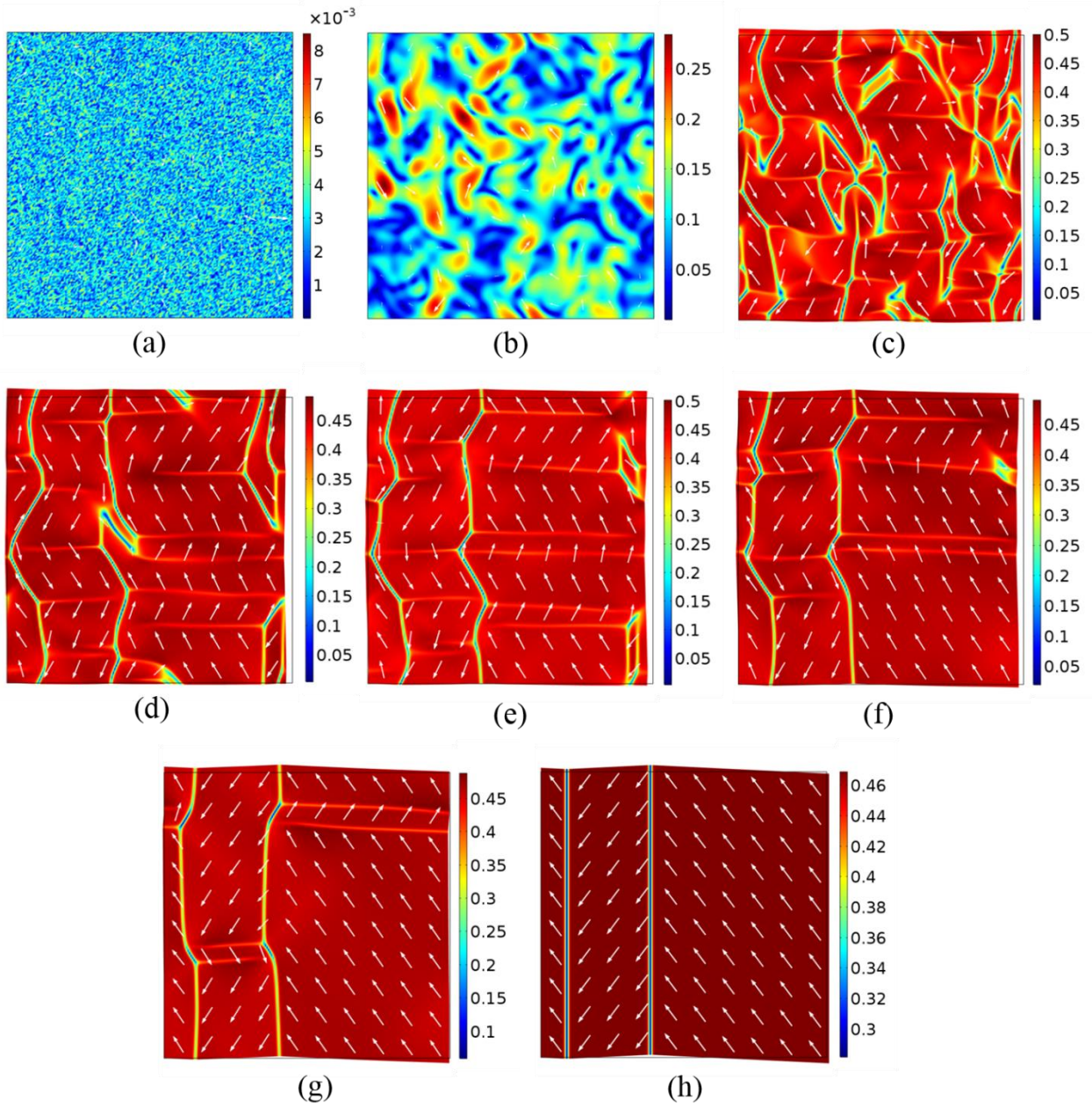

Figure 4.3. Domain formation process in a representative volume element of the rhombohedral ferroelectric single crystals. The colors represent the magnitude of polarization with unit C/m^2. The white arrows represent the directions of polarization. The deformation is magnified by 10 times.

4.4 Electric field driven domain wall evolution

4.4.1 71 domain wall

A square periodic element containing two 71 domain walls was simulated. The size of the square was $40\times40\text{nm}^2$. Periodic boundary conditions were applied. Two 71 domain walls were formed at one-quarter and three-quarter of the height by setting the initial conditions in the proximity of the expected equilibrium solutions of R4 in the middle and R3 in the top and bottom, and then letting the system relax. The resulting equilibrium state at $t = 0$ is shown in Figure 4.4. An electric field along the [110] direction was applied by setting the potential difference on the top and bottom boundaries accordingly. The electric field was in a triangle wave form with the peak field 1MV/m. The period T was long enough so that the system reached equilibrium at each step. The volume average p_y along the [001] direction ($P_{[001]}$) and p_z along the [110] direction ($P_{[110]}$) are also plotted in Figure 4.4. $P_{[001]}$ was zero throughout the process, meaning the 71 domain walls did not move. $P_{[110]}$ varied with the field applied, indicating broadening and narrowing of the 71 domain walls. No domain switching occurred. When the field was in the opposite direction from the polarization, the 71 domain walls became narrower. When the field was in the same direction, the 71 domain walls became wider. The domain walls were thinnest (t = T/4) and thickest (t = 3T/4) when the field reached the positive peak and negative peak, respectively.

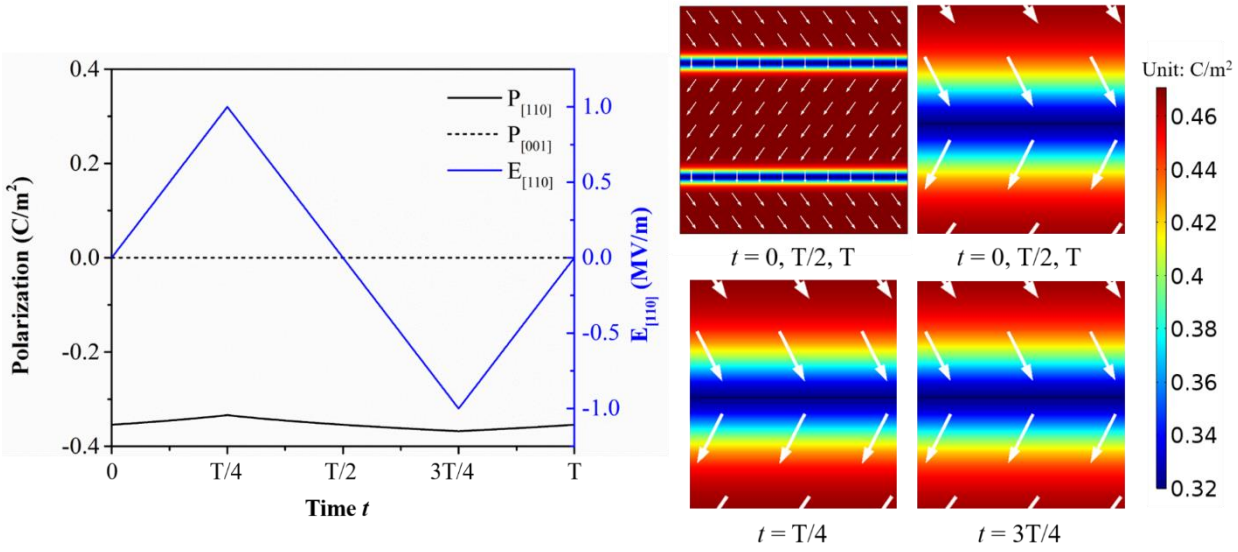

Figure 4.4. The broadening of the 71 domain walls when the electric field is below the coercive field. T is the period of the electric field. The domain wall is zoomed in to show the variation of the domain wall thickness.

When the electric field exceeded the coercive field, polarization switching occurred as shown in Figure 4.5. At t = 0, R3 and R4 were separated by two 71 domain walls. As the positive field increased and exceeded the coercive field, $P_{[110]}$ jumped to a positive value with R3 switching to R1 and R4 switching to R2 simultaneously. The domains stayed with R1 and R2 as the field decreased to zero at t = T/2. When the field became negative and went beyond the coercive field, $P_{[110]}$ jumped back to being negative with R1 and R2 switching back. In the meantime, $P_{[001]}$ remained zero, indicating the 71 domain wall did not move during the switching process. As the electric field cycled, polarization switching occurred homogeneously without domain wall motion. This is the domain engineering effect, where the electric field does not provide a driving force for domain wall motion. This lack of domain wall motion is the reason why the domain engineered crystals have a very low dielectric loss coefficient (tanδ) and high electromechanical coupling factors.

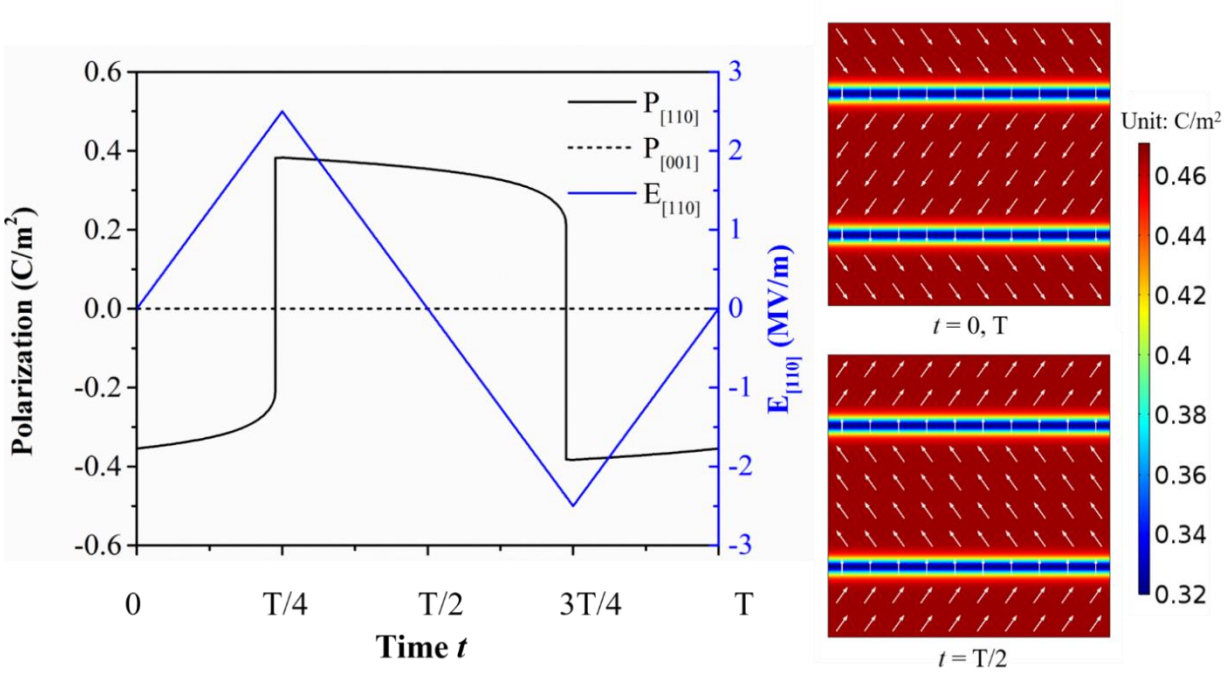

Figure 4.5. The homogeneous polarization switching with no motion of the 71 domain walls when the electric field exceeds the coercive field. The domains before and after the switching are shown on the right.

4.4.2 109 domain wall

A square periodic element containing two 109 domain walls was simulated. The size of the square was $40\times40\text{nm}^2$. Periodic boundary conditions were applied. Two 109 domain walls were formed at one-quarter and three-quarter of the width by setting the initial conditions in the proximity of the expected equilibrium solutions of R3 in the middle and R1 in the left and right, and then letting the system relax. The obtained equilibrium state at $t = 0$ is shown in Figure 4.6. A constant electric field of 0.1MV/m along the [110] direction was applied by setting the potential difference on the top and bottom boundaries accordingly. The electric field was applied at $t = 0$ and the response of $P_{[110]}$ and $P_{[001]}$ is plotted in Figure 4.6. The increase of $P_{[110]}$ corresponded to the motion of two 109 domain walls towards each other as R3 switched to R1. The domain wall motion exhibited an almost linear behavior until an abrupt change to $P_{[110]}$ and

$P_{[001]}$ was observed when the two 109 domain walls began to contact and merge. Eventually the 109 domain walls disappeared. R3 domain completely switched to R1 through the sweeping of the 109 domain walls and a single domain was formed. The response of the single domain is governed by the Landau-Devonshire energy and the hysteresis loops can be reproduced as those in reference [10]. The switching from R3 to R1 is not a strain free process. If the zero strain type of periodic boundary conditions is applied, two 109 domain walls shown in Figure 4.6 will not merge due to the mechanical clamping effect and thus the single domain will not form. The time axis in Figure 4.6 provides an idea of how long it takes to reach equilibrium under the given conditions. The domains reach equilibrium at each time step if the period of the cyclic electric field is longer than nano-seconds by orders of magnitude.

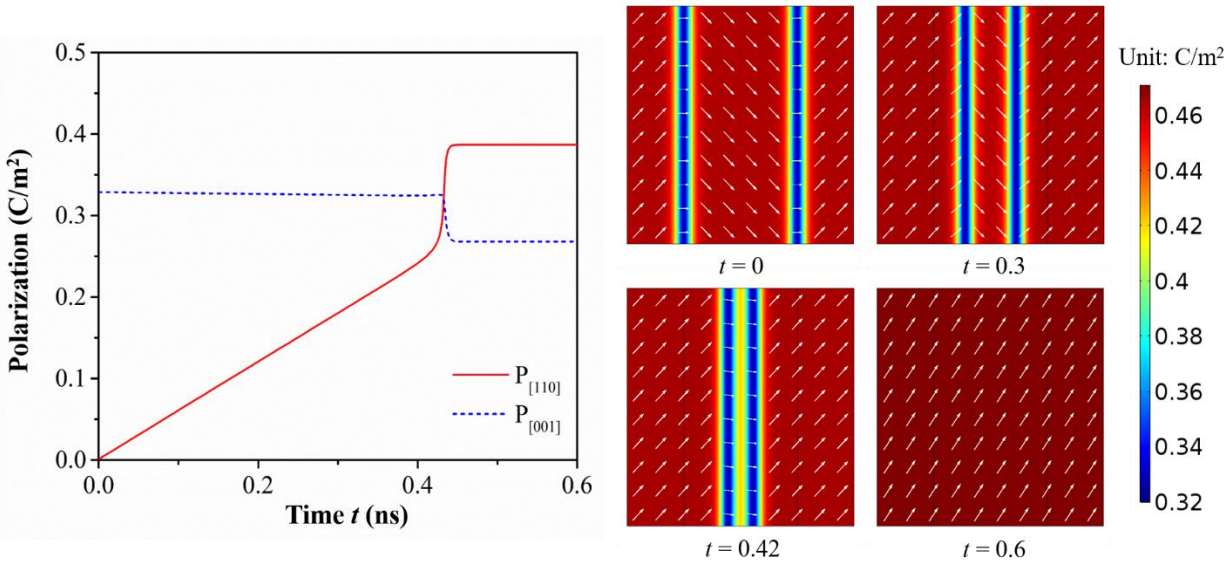

Figure 4.6. The sweeping of the 109 domain walls and heterogeneous polarization switching under the constant electric field 0.1MV/m. A single domain is formed after the two domain walls merge and disappear.

Note the electric field applied in Figure 4.6 is only 0.1MV/m. If an even lower electric field is applied, a smaller driving force will be generated and the 109 domain walls will move slower.

There is no critical electric field to drive the sweeping of 109 domain walls. This is because under the electric field along the [110] direction, the domain on one side of the 109 domain wall is always favored by the field while the other is not. The favored domain expands by pushing the domain wall to the disfavored one. This heterogeneous process does not involve all the material at the same time. It is a local effect where the two regions compete and the wall in between moves towards the region with higher energy to minimize that region. This helps reduce the field or energy required to drive the polarization switching as compared to the case where the whole region is equally favored by the electric field and it has to be switched simultaneously. There are some other factors that may affect the polarization switching such as the domain size, loading rate, gradient coefficients and defects or other pinning sources. The complete study of these factors goes beyond this work. However, the simulation results show the fundamental difference in the mechanism of polarization switching with 71 or 109 domain walls involved. The domain wall sweeping reduces the energy required to reorient the domains in the heterogeneous switching (109 domain wall) compared to the homogeneous switching (71 domain wall).

The simulation results also help understand why the domain wall motion is minimal in the engineered domain structures [65,80,101,102]. Both 71 and 109 domain walls are populated in the unpoled crystals. These crystals are then cut and poled (domain-engineered) to achieve the enhanced piezoelectric properties. During the poling process, domains reorient and align in the directions favored by the field. This reduces 109 domain walls because the domain on one side of 109 domain wall is not favored by the field and these domains are minimized. As a result, the 109 domain walls associated with these disfavored domains disappear. Some may remain due to the domain wall pinning effects but the dominant effect is from the favored domains and the associated 71 domain walls. Since the two domains separated by the 71 domain wall are equally

favored by the external electric field, the domain wall motion is minimal in domain engineered structures. This explains why the intrinsic crystal lattice effects (homogeneous response) account for 80~90% of the overall response while the extrinsic effects related to domain wall motion (heterogeneous response) are only 10~20%.

4.5 Conclusion

In this work, a phase-field model was developed based on a 10^{th} order Landau-Devonshire energy function for rhombohedral PIN-PMN-PT ferroelectric single crystals. In order to gain a better understanding of the engineered domain structures, domain formation and domain wall evolution under the electric field along the [110] direction were simulated. A new way to apply periodic boundary conditions was used to accommodate nonzero strain during domain formation and evolution. Special attention was given to the 71 and 109 domain walls that were populated in the crystal from the domain formation process. The two types of domain walls showed different behavior in response to the electric field. A domain wall broadening effect was observed on the 71 domain walls when the electric field was below the coercive field. Homogeneous polarization switching with no motion of the 71 domain walls occurred when the electric field exceeded the coercive field. While the sweeping of the 109 domain walls facilitated heterogeneous polarization switching and reduced the energy required relative to the homogeneous switching. The two mechanisms of domain evolution explained the minimal domain wall motion in the engineered domain structures under the electric field. With this work, the application of the phase-field method was expanded to the new rhombohedral phase ferroelectric relaxor-PT crystals beyond tetragonal phase ferroelectric materials. This work also provided insight into the engineered domain structures of ferroelectric single crystals that is important in many applications.

5 Summary and conclusions

Domain engineered ferroelectric relaxor-PT crystals have attracted extensive attentions due to their ultrahigh piezoelectric coefficients and electromechanical coupling factors. They show great potential for replacing the conventional piezoelectric ceramics and improving the performance of piezo-based applications such as sensors and actuators. To gain insight into the microstructure and its effects on the material behavior, this dissertation presented a modeling approach from an energetic perspective.

It started with an introduction to the thermodynamics of coupled electromechanical systems in Chapter 2. A kinetic relation governing the evolution of polarization (the TDGL equation) and a finite element formulation to solve the coupled problem were also discussed. These provided the theoretical background of this energetic modeling approach.

A Landau-Devonshire energy function, in the form of a 10^{th} order polynomial, was proposed to describe the dielectric, piezoelectric and ferroelectric properties of rhombohedral phase PIN-PMN-PT crystals with a MPB composition. This was elaborated in Chapter 3. The coefficients of this energy function were determined through extensive fitting to the experimental data. The resulting energy function reproduced the temperature induced phase transformations as well as the polarization and strain hysteresis loops of domain engineered 4R and 2R crystals. With the energy function proposed, the Landau-Devonshire theory was extended from the conventional $BaTiO_3$ crystals with tetragonal symmetry to the novel PIN-PMN-PT crystals with rhombohedral symmetry.

This energy function was then implemented in a phase-field model to investigate the evolution of domain structures under the electric field. The details were presented in Chapter 4.

In order to accommodate nonzero strain during domain formation and evolution, a new way to apply periodic boundary conditions was proposed. The domain formation process was simulated first and 71 and 109 domain walls were found to populate the crystals. Then these two types of domain walls were individually studied under the electric field applied along the [110] direction. They showed different behavior in response to the electric field. A domain wall broadening effect was observed on 71 domain walls when below the coercive field. When the electric field exceeded the coercive field, homogeneous polarization switching occurred with no motion of 71 domain walls. While the sweeping of 109 domain walls facilitated heterogeneous polarization switching and reduced the energy required relative to homogeneous polarization switching. The two mechanisms of domain evolution are consistent with the minimal domain wall motion in the engineered domain structures under the electric field. With this work, the application of the phase-field method was expanded to the new rhombohedral phase relaxor-PT crystals beyond tetragonal phase ferroelectric materials. This work also deepened the understanding of domain structures in ferroelectric single crystals that is important in many applications.

References

[1] S. Zhang, F. Li, High performance ferroelectric relaxor-PbTiO3 single crystals: Status and perspective, J. Appl. Phys. 111 (2012) 031301. doi:10.1063/1.3679521.

[2] S.-E. Park, T.R. Shrout, Ultrahigh strain and piezoelectric behavior in relaxor based ferroelectric single crystals, J. Appl. Phys. 82 (1997) 1804–1811. doi:10.1063/1.365983.

[3] A.J. Bell, Phenomenologically derived electric field-temperature phase diagrams and piezoelectric coefficients for single crystal barium titanate under fields along different axes, J. Appl. Phys. 89 (2001) 3907–3914. doi:10.1063/1.1352682.

[4] E. Sun, W. Cao, Relaxor-based ferroelectric single crystals: Growth, domain engineering, characterization and applications, Prog. Mater. Sci. 65 (2014) 124–210. doi:10.1016/j.pmatsci.2014.03.006.

[5] S. Zhang, F. Li, N.P. Sherlock, J. Luo, H. Jae Lee, R. Xia, R.J. Meyer, W. Hackenberger, T.R. Shrout, Recent developments on high Curie temperature PIN-PMN-PT ferroelectric crystals, J. Cryst. Growth. 318 (2011) 846–850. doi:10.1016/j.jcrysgro.2010.11.043.

[6] X. Huo, S. Zhang, G. Liu, R. Zhang, J. Luo, R. Sahul, W. Cao, T.R. Shrout, Complete set of elastic, dielectric, and piezoelectric constants of [011]C poled rhombohedral Pb(In0.5Nb0.5)O 3-Pb(Mg1/3Nb2/3)O3-PbTiO 3:Mn single crystals, J. Appl. Phys. 113 (2013) 074106. doi:10.1063/1.4792661.

[7] B. Noheda, D.E. Cox, G. Shirane, J. Gao, Z.-G. Ye, Phase diagram of the ferroelectric relaxor (1-x)PbMg1/3Nb2/3O3-xPbTiO3, Phys. Rev. B. 66 (2002) 054104. doi:10.1103/PhysRevB.66.054104.

[8] S. Zhang, T.R. Shrout, Relaxor-PT single crystals: Observations and developments, IEEE Trans. Ultrason. Ferroelectr. Freq. Control. 57 (2010) 2138–2146. doi:10.1109/TUFFC.2010.1670.

[9] L.-Q. Chen, Phase-Field Models for Microstructure Evolution, Annu. Rev. Mater. Res. 32 (2002) 113–140. doi:10.1146/annurev.matsci.32.112001.132041.

[10] P. Lv, L. Wang, C.S. Lynch, A phenomenological thermodynamic energy function for PIN-PMN-PT relaxor ferroelectric single crystals, Acta Mater. 137 (2017) 93–102. doi:10.1016/j.actamat.2017.07.031.

[11] P. Lv, C.S. Lynch, Phase- field simulation of domain walls in rhombohedral ferroelectric single crystals, Acta Mater. 155 (2018) 245–252. doi:10.1016/j.actamat.2018.06.016.

[12] W.G. Cady, Piezoelectricity: an introduction to the theory and applications of electromechanical phenomena in crystals, McGraw-Hill, New York, 1946.

[13] B. Jaffe, W.R. Cook, H. Jaffe, Piezoelectric ceramics, Academic Press, 1971. doi:10.1016/b978-0-12-379550-2.x5001-7.

[14] B. Jaffe, R.S. Roth, S. Marzullo, Piezoelectric properties of Lead zirconate-Lead titanate solid-solution ceramics, J. Appl. Phys. 25 (1954) 809–810. doi:10.1063/1.1721741.

[15] A.J. Moulson, J.M. Herbert, Electroceramics: materials, properties, applications, John Wiley & Sons, 2003. doi:10.5860/choice.28-0314.

[16] G. Yi, Z. Wu, M. Sayer, Preparation of Pb(Zr,Ti)O3 thin films by sol gel processing: Electrical, optical, and electro- optic properties, J. Appl. Phys. 64 (1988) 2717–2724. doi:10.1063/1.341613.

[17] P. Muralt, Ferroelectric thin films for micro-sensors and actuators: a review, J. Micromechanics Microengineering. 10 (2000) 136–146. doi:10.1088/0960-1317/10/2/307.

[18] N. Setter, D. Damjanovic, L. Eng, G. Fox, S. Gevorgian, S. Hong, A. Kingon, H. Kohlstedt, N.Y. Park, G.B. Stephenson, I. Stolitchnov, A.K. Taganstev, D. V. Taylor, T. Yamada, S. Streiffer, Ferroelectric thin films: Review of materials, properties, and applications, J. Appl. Phys. 100 (2006) 051606. doi:10.1063/1.2336999.

[19] E. Cross, Materials science: Lead-free at last, Nature. 432 (2004) 24–25. doi:10.1038/nature03142.

[20] J. Rödel, W. Jo, K.T.P. Seifert, E.M. Anton, T. Granzow, D. Damjanovic, Perspective on the development of lead-free piezoceramics, J. Am. Ceram. Soc. 92 (2009) 1153–1177. doi:10.1111/j.1551-2916.2009.03061.x.

[21] Y. Saito, H. Takao, T. Tani, T. Nonoyama, K. Takatori, T. Homma, T. Nagaya, M. Nakamura, Lead-free piezoceramics, Nature. 432 (2004) 84–87. doi:10.1038/nature03028.

[22] T.R. Shrout, S.J. Zhang, Lead-free piezoelectric ceramics: Alternatives for PZT?, J. Electroceramics. 19 (2007) 111–124. doi:10.1007/s10832-007-9047-0.

[23] M.D. Maeder, D. Damjanovic, N. Setter, Lead free piezoelectric materials, J. Electroceramics. 13 (2004) 385–392. doi:10.1007/s10832-004-5130-y.

[24] D. Damjanovic, N. Klein, J. Li, V. Porokhonskyy, What Can Be Expected From Lead-Free Piezoelectric Materials?, Funct. Mater. Lett. 03 (2010) 5–13. doi:10.1142/S1793604710000919.

[25] A. Vinogradov, F. Holloway, Electro-mechanical properties of the piezoelectric polymer PVDF, Ferroelectrics. 226 (1999) 169–181. doi:10.1080/00150199908230298.

[26] H. Kawai, The Piezoelectricity of Poly (vinylidene Fluoride), Jpn. J. Appl. Phys. 8 (1969) 975–976. doi:10.1143/jjap.8.975.

[27] Acmite Market Intelligence, Global Piezoelectric Device Market, 2017. https://www.acmite.com/market-reports/materials/global-piezoelectric-device-market.html.

[28] M.E. Lines, A.M. Glass, Principles and applications of ferroelectrics and related materials, Oxford university press, 1977. doi:10.1093/acprof:oso/9780198507789.001.0001.

[29] D. Damjanovic, Ferroelectric, dielectric and piezoelectric properties of ferroelectric thin films and ceramics, Reports Prog. Phys. 61 (1998) 1267–1324. doi:10.1088/0034-4885/61/9/002.

[30] F. Li, L. Jin, Z. Xu, S. Zhang, Electrostrictive effect in ferroelectrics : An alternative approach to improve piezoelectricity, Appl. Phys. Rev. 1 (2014) 011103. doi:10.1063/1.4861260.

[31] L.E. Cross, S.J. Jang, R.E. Newnham, S. Nomura, K. Uchino, Large electrostrictive effects in relaxor ferroelectrics, Ferroelectrics. 23 (1980) 187–192. doi:10.1080/00150198008018801.

[32] K. Uchino, S. Nomura, L.E. Cross, R.E. Newnham, S.J. Jang, Electrostrictive effect in perovskites and its transducer applications, J. Mater. Sci. 16 (1981) 569–578. doi:10.1007/BF00552193.

[33] C.B. Sawyer, C.H. Tower, Rochelle Salt as a Dielectric, Phys. Rev. 35 (1930) 269–273. doi:10.1103/physrev.35.269.

[34] S.C. Hwang, C.S. Lynch, R.M. McMeeking, Ferroelectric/ferroelastic interactions and a polarization switching model, Acta Metall. Mater. 43 (1995) 2073–2084. doi:10.1016/0956-7151(94)00379-v.

[35] D. Carka, C.S. Lynch, Ferroelectric and Ferromagnetic Phase Field Modeling, in: J. Schröder, D.C. Lupascu (Eds.), Ferroic Funct. Mater., Springer, 2018: pp. 55–96.

[36] Y. Su, C. Landis, Continuum thermodynamics of ferroelectric domain evolution: Theory, finite element implementation, and application to domain wall pinning, J. Mech. Phys. Solids. 55 (2007) 280–305. doi:10.1016/j.jmps.2006.07.006.

[37] B. Völker, C.M. Landis, M. Kamlah, Multiscale modeling for ferroelectric materials: identification of the phase-field model's free energy for PZT from atomistic simulations, Smart Mater. Struct. 21 (2012) 035025. doi:10.1088/0964-1726/21/3/035025.

[38] E. Fried, M.E. Gurtin, Continuum theory of thermally induced phase transitions based on an order parameter, Phys. D. 68 (1993) 326–343. doi:10.1016/0167-2789(93)90128-N.

[39] E. Fried, M.E. Gurtin, Dynamic solid-solid transitions with phase characterized by an order parameter, Phys. D. 72 (1994) 287–308. doi:10.1016/0167-2789(94)90234-8.

[40] M.E. Gurtin, Generalized Ginzburg-Landau and Cahn-Hilliard equations based on a microforce balance, Phys. D. 92 (1996) 178–192. doi:10.1016/0167-2789(95)00173-5.

[41] L.Q. Chen, J. Shen, Applications of semi-implicit Fourier-spectral method to phase field equations, Comput. Phys. Commun. 108 (1998) 147–158. doi:10.1016/S0010-4655(97)00115-X.

[42] W. Zhang, K. Bhattacharya, A computational model of ferroelectric domains. Part I: model formulation and domain switching, Acta Mater. 53 (2005) 185–198.

doi:10.1016/j.actamat.2004.09.016.

[43] D. Schrade, R. Mueller, B.X. Xu, D. Gross, Domain evolution in ferroelectric materials: A continuum phase field model and finite element implementation, Comput. Methods Appl. Mech. Eng. 196 (2007) 4365–4374. doi:10.1016/j.cma.2007.05.010.

[44] K.-J. Bathe, Finite element procedures, 2nd ed., 2006.

[45] A.F. Devonshire, XCVI. Theory of Barium Titanate Part I, London, Edinburgh, Dublin Philos. Mag. J. Sci. 40 (1949) 1040–1063.

[46] A.F. Devonshire, CIX. Theory of Barium Titanate Part II, London, Edinburgh, Dublin Philos. Mag. J. Sci. 42 (1951) 1065–1079.

[47] A.J. Bell, L.E. Cross, A phenomenological gibbs function for BaTiO3 giving correct E field dependence of all ferroelectric phase changes, Ferroelectrics. 59 (1984) 197–203. doi:10.1080/00150198408240090.

[48] A. Amin, M.J. Haun, B. Badger, H. McKinstry, L.E. Cross, A phenomenological Gibbs function for the single cell region of the PbZrO3:PbTiO3 solid solution system, Ferroelectrics. 65 (1985) 107–130. doi:10.1080/00150198508008964.

[49] M.J. Haun, E. Furman, S.J. Jang, H.A. Mckinstry, L.E. Cross, Thermodynamic theory of PbTiO3, J. Appl. Phys. 62 (1987) 3331–3338. doi:10.1063/1.339293.

[50] M.J. Haun, T.J. Harvin, M.T. Lanagan, Z.Q. Zhuang, S.J. Jang, L.E. Cross, Thermodynamic theory of PbZrO3, J. Appl. Phys. 65 (1989) 3173–3180. doi:10.1063/1.342668.

[51] C. Kittel, Theory of Antiferroelectric Crystals, Phys. Rev. 82 (1951) 729–732. doi:10.1103/physrev.82.729.

[52] B. Noheda, D.E. Cox, G. Shirane, J.A. Gonzalo, L.E. Cross, S.-E. Park, A monoclinic ferroelectric phase in the Pb(Zr1-xTix)O3 solid solution, Appl. Phys. Lett. 74 (1999) 2059–2061. doi:10.1063/1.123756.

[53] D. Vanderbilt, M.H. Cohen, Monoclinic and triclinic phases in higher-order Devonshire

theory, Phys. Rev. B. 63 (2001) 094108. doi:10.1103/PhysRevB.63.094108.

[54] Y.L. Li, L.E. Cross, L.Q. Chen, A phenomenological thermodynamic potential for BaTiO3 single crystals, J. Appl. Phys. 98 (2005) 064101. doi:10.1063/1.2042528.

[55] Y.L. Wang, a. K. Tagantsev, D. Damjanovic, N. Setter, V.K. Yarmarkin, a. I. Sokolov, I. a. Lukyanchuk, Landau thermodynamic potential for BaTiO3, J. Appl. Phys. 101 (2007) 104115. doi:10.1063/1.2733744.

[56] A.A. Heitmann, G.A. Rossetti, Thermodynamics of polar anisotropy in morphotropic ferroelectric solid solutions, Philos. Mag. 90 (2010) 71–87. doi:10.1080/14786430902897750.

[57] A.A. Heitmann, G.A. Rossetti, Thermodynamics of ferroelectric solid solutions with morphotropic phase boundaries, J. Am. Ceram. Soc. 97 (2014) 1661–1685. doi:10.1111/jace.12979.

[58] B. Völker, P. Marton, C. Elsässer, M. Kamlah, Multiscale modeling for ferroelectric materials: A transition from the atomic level to phase-field modeling, Contin. Mech. Thermodyn. 23 (2011) 435–451. doi:10.1007/s00161-011-0188-7.

[59] H.-L. Hu, L.-Q. Chen, Computer simulation of 90 ° ferroelectric domain formation in two-dimensions, Mater. Sci. Eng. A. 238 (1997) 182–191. doi:10.1016/S0921-5093(97)00453-X.

[60] H.-L. Hu, L.-Q. Chen, Three-Dimensional Computer Simulation of Ferroelectric Domain Formation, J. Am. Ceram. Soc. 81 (1998) 492–500. doi:10.1111/j.1151-2916.1998.tb02367.x.

[61] W. Zhang, K. Bhattacharya, A computational model of ferroelectric domains. Part II: grain boundaries and defect pinning, Acta Mater. 53 (2005) 199–209. doi:10.1016/j.actamat.2004.09.015.

[62] S. Wada, S.-E. Park, L.E. Cross, T.R. Shrout, Engineered domain configuration in rhombohedral PZN-PT single crystals and their ferroelectric related properties, Ferroelectrics. 221 (1999) 147–155. doi:10.1080/00150199908016449.

[63] S.-E. Park, S. Wada, L.E. Cross, T.R. Shrout, Crystallographically engineered BaTiO3 single crystals for high-performance piezoelectrics, J. Appl. Phys. 86 (1999) 2746–2750. doi:10.1063/1.371120.

[64] J. Tian, P. Han, X. Huang, H. Pan, J.F. Carroll, D. a. Payne, Improved stability for piezoelectric crystals grown in the lead indium niobate-lead magnesium niobate-lead titanate system, Appl. Phys. Lett. 91 (2007) 222903. doi:10.1063/1.2817743.

[65] F. Li, S. Zhang, Z. Xu, Z. Li, X. Wei, DC Bias Electric Field Dependent Piezoelectricity for [001] Poled Pb(In1/2Nb1/2)O3-Pb(Mg1/3Nb2/3)O3-PbTiO3 Crystals, J. Adv. Dielectr. 01 (2011) 303–308. doi:10.1142/S2010135X11000422.

[66] F. Li, S. Zhang, D. Lin, J. Luo, Z. Xu, X. Wei, T.R. Shrout, Electromechanical properties of Pb(In1/2Nb1/2)O3-Pb(Mg1/3Nb2/3)O3-PbTiO3 single crystals, J. Appl. Phys. 109 (2011) 014108. doi:10.1063/1.3530617.

[67] E. Sun, S. Zhang, J. Luo, T.R. Shrout, W. Cao, Elastic, dielectric, and piezoelectric constants of Pb(In1⁄2Nb1⁄2)O3–Pb(Mg1⁄3Nb2⁄3)O3–PbTiO3 single crystal poled along [011]c, Appl. Phys. Lett. 97 (2010) 032902. doi:10.1063/1.3466906.

[68] F. Li, S. Zhang, Z. Xu, X. Wei, J. Luo, T.R. Shrout, Electromechanical properties of tetragonal Pb(In1/2Nb1/2)O3−Pb(Mg1/3Nb2/3)O3−PbTiO3 ferroelectric crystals, J. Appl. Phys. 107 (2010) 054107. doi:10.1063/1.3331407.

[69] S. Zhang, G. Liu, W. Jiang, J. Luo, W. Cao, T.R. Shrout, Characterization of single domain Pb(In0. 5Nb0. 5)O3-Pb(Mg1/3Nb2/3)O3-PbTiO3 crystals with monoclinic phase, J. Appl. Phys. 110 (2011) 064108. doi:10.1063/1.3639316.

[70] E. Sun, W. Cao, W. Jiang, P. Han, Complete set of material properties of single domain 0.24Pb(In1/2Nb1/2)O3-0.49Pb(Mg1/3Nb2/3)O3-0.27PbTiO3 single crystal and the orientation effects, Appl. Phys. Lett. 99 (2011) 032901. doi:10.1063/1.3615684.

[71] L. Liang, Y.L. Li, L.Q. Chen, S.Y. Hu, G.H. Lu, A thermodynamic free energy function for potassium niobate, Appl. Phys. Lett. 94 (2009) 072904. doi:10.1063/1.3081418.

[72] T. Liu, C.S. Lynch, Crystal Variant Based Modeling of Relaxor Single Crystals, Proc.

SPIE. 5053 (2003) 347–356. doi:10.1117/12.484706.

[73] T. Liu, C.S. Lynch, Ferroelectric properties of [110], [001] and [111] poled relaxor single crystals: Measurements and modeling, Acta Mater. 51 (2003) 407–416. doi:10.1016/S1359-6454(02)00422-6.

[74] X. Liu, S. Zhang, J. Luo, T.R. Shrout, W. Cao, Complete set of material constants of Pb(In1/2Nb1/2)O3–Pb(Mg1/3Nb2/3)O3–PbTiO3 single crystal with morphotropic phase boundary composition, J. Appl. Phys. 106 (2009) 074112. doi:10.1063/1.3243169.

[75] S. Zhang, J. Luo, W. Hackenberger, N.P. Sherlock, R.J. Meyer, T.R. Shrout, Electromechanical characterization of PIN-PMN-PT cystals as a function of crystallographic orientation and temperature, J. Appl. Phys. 105 (2009) 104506. doi:10.1063/1.3131622.

[76] E. Sun, W. Cao, P. Han, Complete set of material properties of [011]c poled 0.24Pb(In1/2Nb1/2)O3–0.46Pb(Mg1/3Nb2/3)O3–0.30PbTiO3 single crystal, Mater. Lett. 65 (2011) 2855–2857. doi:10.1016/j.matlet.2011.06.013.

[77] S. Zhang, F. Li, J. Luo, R. Xia, W. Hackenberger, T.R. Shrout, Investigation of single and multidomain Pb(In0.5Nb 0.5)O3-Pb(Mg1/3Nb2/3)O3-PbTiO3 crystals with mm2 symmetry, Appl. Phys. Lett. 97 (2010) 132903. doi:10.1063/1.3494532.

[78] E. Sun, R. Zhang, F. Wu, W. Cao, Complete matrix properties of [001](c) and [011](c) poled 0.33Pb(In(1/2)Nb(1/2))O(3)-0.38Pb(Mg(1/3)Nb(2/3))O(3)-0.29PbTiO(3) single crystals, J. Alloys Compd. 553 (2013) 267–269. doi:10.1016/j.jallcom.2012.11.111.

[79] E. Sun, R. Zhang, F. Wu, B. Yang, W. Cao, Influence of manganese doping to the full tensor properties of 0.24Pb(In1/2Nb1/2)O3-0.47Pb(Mg1/3Nb2/3)O3-0.29PbTiO3 single crystals, J. Appl. Phys. 113 (2013) 074108. doi:10.1063/1.4792600.

[80] F.H. Schader, G.A. Rossetti, J. Luo, K.G. Webber, Piezoelectric and ferroelectric properties of <001>C Pb(In1/2Nb1/2)O3-Pb(Mg1/3Nb2/3)O3-PbTiO3 single crystals under combined thermal and mechanical loading, Acta Mater. 126 (2017) 174–181. doi:10.1016/j.actamat.2016.12.051.

[81] Y. Wan, Z. Li, Z. Xu, S. Fan, X. Yao, Phase transition characteristics of the relaxor-based 0.24PIN–0.51PMN–0.25PT single crystals, J. Alloys Compd. 558 (2013) 244–247. doi:10.1016/j.jallcom.2013.01.034.

[82] Y.L. Li, S.Y. Hu, Z.K. Liu, L.Q. Chen, Phase-field model of domain structures in ferroelectric thin films, Appl. Phys. Lett. 78 (2001) 3878–3880. doi:10.1063/1.1377855.

[83] Y. Li, S.Y. Hu, Z.K. Liu, L.Q. Chen, Effect of substrate constraint on the stability and evolution of ferroelectric domain structures in thin films, Acta Mater. 50 (2002) 395–411. doi:10.1016/s1359-6454(01)00360-3.

[84] Y. Li, S.Y. Hu, Z.K. Liu, L.Q. Chen, Effect of electrical boundary conditions on ferroelectric domain structures in thin films, Appl. Phys. Lett. 81 (2002) 427–429. doi:10.1063/1.1492025.

[85] L.Q. Chen, Phase-field method of phase transitions/domain structures in ferroelectric thin films: A review, J. Am. Ceram. Soc. 91 (2008) 1835–1844. doi:10.1111/j.1551-2916.2008.02413.x.

[86] J. Wang, S.Q. Shi, L.Q. Chen, Y. Li, T.Y. Zhang, Phase-field simulations of ferroelectric/ferroelastic polarization switching, Acta Mater. 52 (2004) 749–764. doi:10.1016/j.actamat.2003.10.011.

[87] J. Wang, Y. Li, L. Chen, T. Zhang, The effect of mechanical strains on the ferroelectric and dielectric properties of a model single crystal - Phase field simulation, Acta Mater. 53 (2005) 2495–2507. doi:10.1016/j.actamat.2005.02.011.

[88] J. Wang, T.Y. Zhang, Phase field simulations of polarization switching-induced toughening in ferroelectric ceramics, Acta Mater. 55 (2007) 2465–2477. doi:10.1016/j.actamat.2006.11.041.

[89] J. Wang, M. Kamlah, Three-dimensional finite element modeling of polarization switching in a ferroelectric single domain with an impermeable notch, Smart Mater. Struct. 18 (2009) 104008. doi:10.1088/0964-1726/18/10/104008.

[90] J. Wang, M. Kamlah, Effect of electrical boundary conditions on the polarization

distribution around a crack embedded in a ferroelectric single domain, Eng. Fract. Mech. 77 (2010) 3658–3669. doi:10.1016/j.engfracmech.2010.07.007.

[91] S. Choudhury, Y.L. Li, C.E. Krill, L.Q. Chen, Phase-field simulation of polarization switching and domain evolution in ferroelectric polycrystals, Acta Mater. 53 (2005) 5313–5321. doi:10.1016/j.actamat.2005.07.040.

[92] W. Shu, J. Wang, T. Zhang, Effect of grain boundary on the electromechanical response of ferroelectric polycrystals, J. Appl. Phys. 112 (2012) 064108. doi:10.1063/1.4752269.

[93] J. Wang, W. Shu, T. Shimada, T. Kitamura, T.Y. Zhang, Role of grain orientation distribution in the ferroelectric and ferroelastic domain switching of ferroelectric polycrystals, Acta Mater. 61 (2013) 6037–6049. doi:10.1016/j.actamat.2013.06.044.

[94] Y. Gu, M. Li, A.N. Morozovska, Y. Wang, E.A. Eliseev, V. Gopalan, L.Q. Chen, Flexoelectricity and ferroelectric domain wall structures: Phase-field modeling and DFT calculations, Phys. Rev. B. 89 (2014) 174111. doi:10.1103/PhysRevB.89.174111.

[95] R. Ahluwalia, A.K. Tagantsev, P. Yudin, N. Setter, N. Ng, D.J. Srolovitz, Influence of flexoelectric coupling on domain patterns in ferroelectrics, Phys. Rev. B. 89 (2014) 174105. doi:10.1103/PhysRevB.89.174105.

[96] Y. Gu, Z. Hong, J. Britson, L.Q. Chen, Nanoscale mechanical switching of ferroelectric polarization via flexoelectricity, Appl. Phys. Lett. 106 (2015) 022904. doi:10.1063/1.4905837.

[97] P. Lv, C.S. Lynch, Energetics of domain engineered rhombohedral ferroelectric single crystals, in: SPIE, 2017: p. 101650B. doi:10.1117/12.2263245.

[98] S. Zhang, J. Luo, W. Hackenberger, T.R. Shrout, Characterization of Pb(In1/2Nb1/2)O3–Pb(Mg1/3Nb2/3)O3–PbTiO3 ferroelectric crystal with enhanced phase transition temperatures, J. Appl. Phys. 104 (2008) 064106. doi:10.1063/1.2978333.

[99] R.J.M. Smit, W.A.M. Brekelmans, H.E.H. Meijer, Prediction of the mechanical behavior of nonlinear heterogeneous systems by multi-level finite element modeling, Comput. Methods Appl. Mech. Eng. 155 (1998) 181–192. doi:10.1016/S0045-7825(97)00139-4.

[100] O. Van Der Sluis, P.J.G. Schreurs, W.A.M. Brekelmans, H.E.H. Meijer, Overall behaviour of heterogeneous elastoviscoplastic materials: Effect of microstructural modelling, Mech. Mater. 32 (2000) 449–462. doi:10.1016/S0167-6636(00)00019-3.

[101] D. Damjanovic, M. Budimir, M. Davis, N. Setter, Monodomain versus polydomain piezoelectric response of 0.67Pb(Mg 1/3Nb2/3)O3-0.33PbTiO3 single crystals along nonpolar directions, Appl. Phys. Lett. 83 (2003) 527–529. doi:10.1063/1.1592880.

[102] F. Li, S. Zhang, Z. Xu, X. Wei, J. Luo, T.R. Shrout, Composition and phase dependence of the intrinsic and extrinsic piezoelectric activity of domain engineered (1-x)Pb(Mg1/3Nb 2/3)O3-xPbTiO3 crystals, J. Appl. Phys. 108 (2010) 034106. doi:10.1063/1.3466978.